Sensing Ultraviolet Light Emission From Hydrogen Flames

Flame detection and flame monitoring in CO2 emission free domestic boilers

S.E. Bielefeld

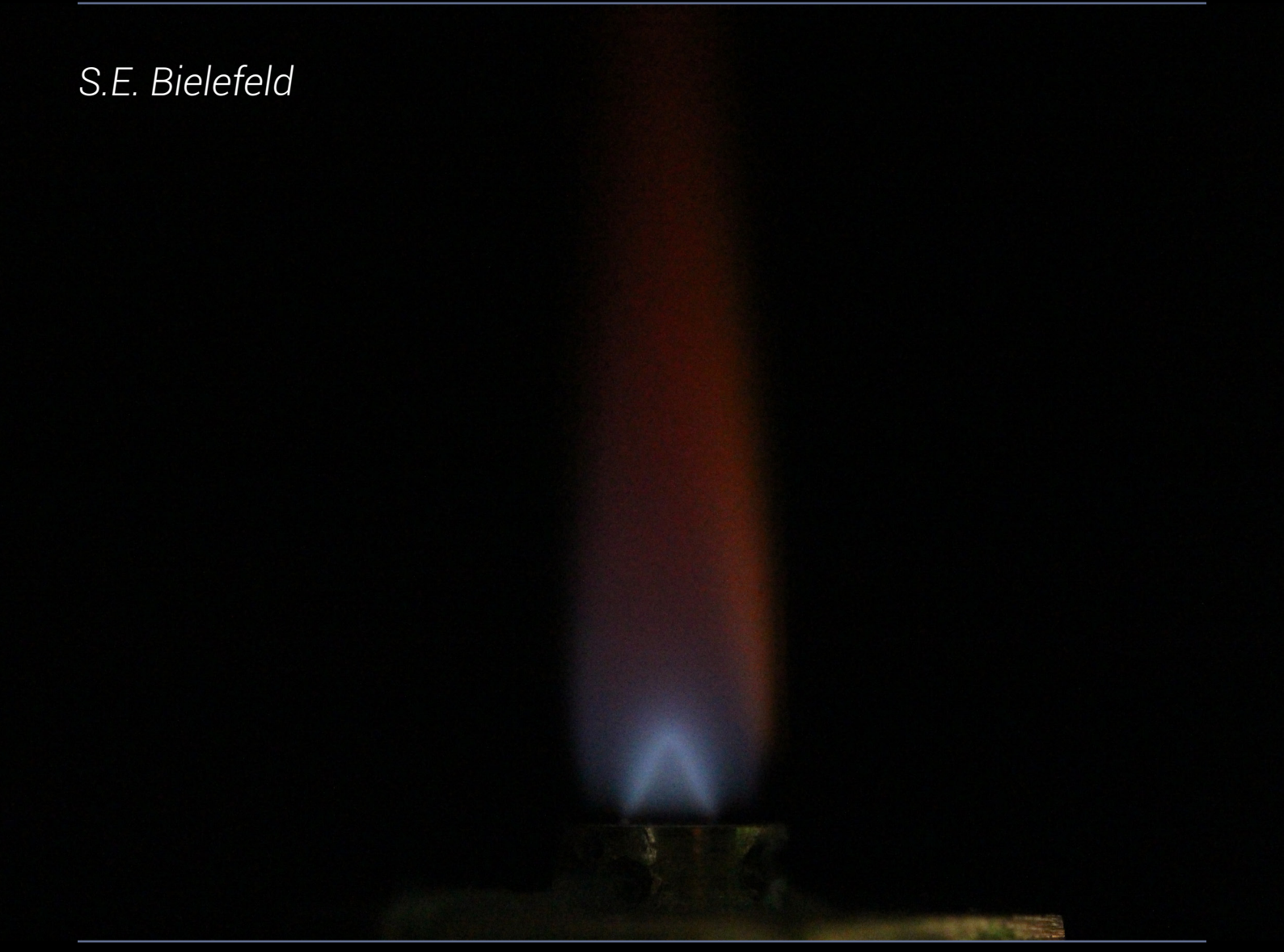

TU Delft

Sensing Ultraviolet Light Emission From Hydrogen Flames

Flame detection and flame monitoring in CO_2 emission free domestic boilers

by

S.E. Bielefeld

to obtain the degree of Master of Science
at the Delft University of Technology,
to be defended publicly on Thursday July 16, 2020 at 08:30 AM.

Student number:	4912535	
Project duration:	November 15, 2019 – July 16, 2020	
Thesis committee:	Prof. dr. D. J. E. M. Roekaerts,	TU Delft, supervisor
	Dr. G. A. Bohlin,	TU Delft
	Dr. ir. M. J. Tummers,	TU Delft
	Dr. N. Beishuizen,	Robert Bosch GmbH

This thesis is confidential and cannot be made public until January 16, 2021.

An electronic version of this thesis is available at `http://repository.tudelft.nl/`.

TU Delft

Preface

This graduation project was a collaboration between the TU Delft and Bosch Thermotechniek. I would like to thank my colleagues Hans, Henny and Jaap for helping me with the manufacturing of the components of the setup, and Lean and Hubert for their help with LabVIEW.
I would also like to thank Yuriy Shoshin for letting me test my burner at the laboratory at the TU Eindhoven, and for constantly being approachable for advice.
Lastly, I thank my supervisors Dirk Roekaerts, Nijso Beishuizen and Gert-Jan Feberwee for guiding me through this work. I am grateful for the time you spent on supervising my project, and for everything I learned while working on this study.

S.E. Bielefeld
Delft, July 2020

Summary

The motivation for this graduation project is the assessment of the novel approach to applying ultraviolet sensor technology for flame detection and monitoring in hydrogen-powered domestic gas boilers. Four questions are addressed:

1. Is the sensor sensitive enough to detect lean flames of $\phi = 0.5$ and $\dot{V} = 2\text{L/min}$ with resulting low radiation levels?
2. Is the sensor sensitive to changes in the equivalence ratio of $\Delta\phi = 0.05$?
3. How does the sensor signal depend on the position of the sensor with respect to the flame?
4. Can the dependence of sensor signal on sensor position be described analytically?

To investigate these points, the study reports the response of an ultraviolet sensor to a Bunsen-like premixed laminar hydrogen-air flame as a function of the sensor position and for different values of the equivalence ratio ϕ.
The first three points are investigated with an empirical parameter study, for which a setup was developed and used. The parameters examined are the equivalence ratio of the gas mixture and three parameters that determine the sensor position. These parameters are the horizontal distance between sensor and flame, the vertical distance between sensor and flame, and the inclination of the sensor.
To compare the experimental data of sensor signal strength for different values of the equivalence ratio to reference values, ultraviolet chemiluminescence images of the flames were recorded during the measurements. The empirical investigation of the influence of the sensor position on the sensor signal was compared to values obtained from a View Factor equation. The View Factor is an analytical approach to describing the fraction of radiation emitted by a surface striking another, dependent on their geometry and relative position. A View Factor was derived for the context of this work and values were calculated for the same sensor positions that have been tested experimentally.
The following conclusions are drawn:

1. The sensor is sensitive enough to detect flames at low radiation levels ($\phi = 0.5$ and $\dot{V} = 2\text{L/min}$). This evidence is supported by the results of the parameter study of ϕ and by those of the parameter study of different sensor positions.
2. The sensor is sensitive to changes in the equivalence ratio of ratio of $\Delta\phi = 0.05$. The predicted operational range of the appliance is given as $0.5 \leq \phi \leq 0.75$. For this range of equivalence ratios, the curve reveals a clear relation between ϕ and sensor signal strength. However, said relation is not as unambiguous for rich flames. Further research should determine the minimal detectable change in equivalence ratio $\Delta\phi$, and is necessary in order to find a strategy for relating the sensor signal to a distinct equivalence ratio for rich flames.
3. Each parameter has a visible influence on the sensor signal. The dependence of the sensor position on the signal strength is reported for those parameters that define the position individually. Only for a few examined sensor positions the flame can not be detected. Installing the sensor at heights lower than $20mm$ is recommended. Regarding the tilt angle of the sensor, installing the sensor in a position where it is directed to the flame base is recommended.
4. The derived View Factor equation cannot be used without further improvements. Qualitatively, the calculated values match the empirical observations. However, accuracy is low because peaks and abrupt decays are not reflected in the View Factor curves. Three aspects are not included in the VF equation. Firstly, the VF does not take into account that the flame does not emit UV light homogeneously over the surface. Secondly, the View Factor does not reflect a possible tip opening, which happens for lean flames, hence those within the operational range of the boiler. Lastly, the VF does not include the influence of the view field of the sensor. If all three can be included, the View Factor is a promising approach for an analytical description of the influence of the sensor position.

Contents

List of Abbreviations

CCD charge-coupled device

COP Conference of Parties

CU Control Unit

FCCC Framework Convention on Climate Change

FoV Field of View

FWHM Full width at half maximum

MFC mass flow controller

LHV Lower Heating Value

UV ultraviolet

VF View Factor

VFB View Factor backside

VFF View Factor frontside

1 Introduction

The world we live in relies heavily on fossil carbon fuels.
We use fossil fuels as feedstock, and to generate electricity and heat in both industrial factories and our homes. In 2018, fossil fuels accounted for more than 70% of Europe's energy mix [14]. Countries strive for economic growth, which can lead to a further increase in the demand for energy, especially in emerging economies. In addition, population growth has a similar effect on the demand for energy.
Burning fossil fuels to generate energy or for other purposes leads to the emission of carbon dioxide, which increases the greenhouse effect of the earth's atmosphere and causes global warming. As climate change advances, it affects and endangers how we live. According to [39], just 50 years from today between 1 and 3 billion people will be living in climatic conditions that are unsuitable for humans. Figure 1.1 illustrates the consequential shift of areas that fit human living. The figures were calculated without accounting for extreme weather events or the expected rise in sea levels. It is clear we need to focus our efforts on keeping global warming as low as possible.
One globally accepted way of doing this was developed during the Conference of Parties (COP) of the United Nations' Framework Convention on Climate Change (FCCC) held in Paris in 2015. Participants agreed to keep "a global temperature rise this century well below 2 degrees Celsius above pre-industrial levels and to pursue efforts to limit the temperature increase even further to 1.5 degrees Celsius" [37]. Greenhouse gas emissions, among which CO_2 emissions, must be decreased if this agreement is to be respected. Therefore, the consumption of fossil carbon energy sources has to be stopped and alternative energy carriers found and implemented.

One promising alternative energy carrier is hydrogen. It has a Lower Heating Value (LHV) of $120 MJ/kg$, the highest number among all the known substances [26]. Methane has an LHV of only 50 MJ/kg. However, the low density of hydrogen leads to a lower value for volumetric energy density, which is relevant when discussing fuels. At $10.8 kJ/L$, the volumetric LHV of hydrogen is the lowest of all fuels [1]. That of methane is $35.8 kJ/L$, more than three times higher.
Hydrogen is abundantly available. Approximately 15% of the earth's surface consists of hydrogen in the form of water, fossil fuel or biomass [26]. Several procedures exist for obtaining molecular hydrogen, among which electrolysis, where electrical energy is used to split water into oxygen and hydrogen. Electrolysis does not produce CO_2 emissions if the required electrical energy is generated from renewable energy sources such as solar or wind energy, to name only two.
Hydrogen can be transported through existing gas networks, if they are adapted to the diffusivity of hydrogen through the pipeline material. This enables decentralized use of hydrogen. However, hydrogen can also be stored as chemical energy for later use, either in its gaseous state, or as a liquid.
Hydrogen has a wide field of application. It can be used as feedstock, generate electricity and heat in fuel cells or be burned, like hydrocarbon gas. Unlike hydrocarbon gas, however, no carbon dioxide is produced.
Reference [31] provides a good overview of the various production methods, storage options and possibilities for transporting hydrogen. It also discusses the safety of hydrogen and compares it to the most frequently used hydrocarbon fuels.

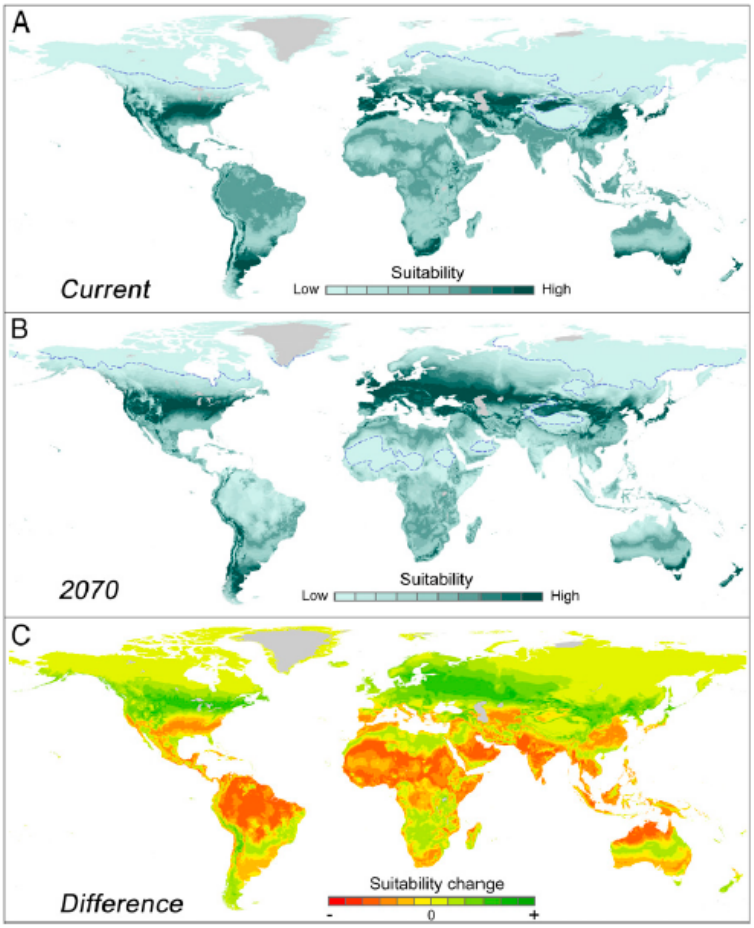

Fig. 4. Projected geographical shift of the human temperature niche. (*Top*) Geographical position of the human temperature niche projected on the current situation (*A*) and the RCP8.5 projected 2070 climate (*B*). Those maps represent relative human distributions (summed to unity) for the imaginary situation that humans would be distributed over temperatures following the stylized double Gaussian model fitted to the modern data (the blue dashed curve in Fig. 2*A*). (*C*) Difference between the maps, visualizing potential source (orange) and sink (green) areas for the coming decades if humans were to be relocated in a way that would maintain this historically stable distribution with respect to temperature. The dashed line in *A* and *B* indicates the 5% percentile of the probability distribution. For an analysis induding precipitation effects, see *SI Appendix*, Fig. S10.

Figure 1.1: Areas suitable for human living today and 50 years from now. Figure taken from reference [39].

In 2018, the residential sector was responsible for 26% of Europe's total final energy consumption. 32% of the corresponding energy was generated from natural gas. 64% of the energy consumed in European households is used for heating spaces and 15% for heating water (figures obtained from [15]). Natural gas is burned in domestic gas boilers for heating both water and spaces and figures are similar for the Netherlands. In 2018, 28% of the final energy demand was consumed by households. The domestic sector emitted 24.6 Mton CO_2 - eq per year. With 69%, heat was the most significant component of residential energy consumption. To meet the goal of the Paris Agreement, the Netherlands agreed to decrease the annual emissions of all greenhouse gases to 5% of the 1990 emissions (figures obtained from [12]). The Dutch government proposes the use of hydrogen as a key strategy to accomplish their target [18].

For using hydrogen to heat water in domestic gas boilers, technological systems need to be adapted to the properties of hydrogen. To ensure safety at all times, the flame in the heat cell of the boiler, where combustion takes place, needs to be monitored continuously. If gas is injected but no flame is burning, hydrogen may leak into the appliance where it will likely cause an explosion, since concentrations of only 4 vol% in the air are explosive already [26]. Explosions can also occur after unburned gas has already accumulated, if the ignition of the gas mixture is delayed. Due to the high burning velocity of hydrogen, the risk of flame flashback is increased compared to conventional hydrocarbon gas mixtures. The inlet velocity has to be adjusted to the equivalence ratio of the fuel-air composition at all times, which makes continuous monitoring crucial. Current monitoring strategies such as the ionization current method are not applicable to hydrogen flames,

since no ions are present in hydrogen flames [33]. Hence, new monitoring strategies need to be developed.

The use of chemiluminescence as an indicator for flame properties such as heat release or equivalence ratio is a mature concept in combustion technology [4, 10, 11]. Chemiluminescence describes the emission of light due to relaxation of the excited radicals produced during the combustion process. This process consists of two steps. At first, an excited radical is formed from two species in eq. (1.1). The second step is the spontaneous loss of the excess energy, during which the radical relaxes back to its ground state energy by releasing a photon ($h\nu$) in eq. (1.2)[4].

$$A + B \rightarrow R^* + \text{others} \tag{1.1}$$

$$R^* \rightarrow R + h\nu \tag{1.2}$$

In the case of hydrogen flames, the decay of the excited hydroxyl radical OH^* emits ultraviolet (UV) light measuring $309nm$ in wavelength [4]. Formation and depletion of OH^* is described through three mechanisms,

$$H + O + M = OH^* + M \tag{1.3}$$

$$OH^* = OH + h\nu \tag{1.4}$$

$$OH^* + M = OH + M \tag{1.5}$$

Kathrotia et al. published a study on the kinetics of OH^* chemiluminescence that provides a detailed overview of the hydrogen combustion system [23]. More studies have investigated OH^* radical concentrations and reaction rates in hydrogen flames [8, 19, 22]. Other studies, such as [19, 32, 41] report spatial distribution of emission intensities. However, no reports on integrated light emission from hydrogen-air flames with different equivalence ratios have been found in literature. No study on the use of UV chemiluminescence as an indicator for monitoring hydrogen flames in domestic hot water boilers has been found, either.

Hydrogen flames emit light at different wavelengths, as shown in Figure 1.2 (for further information on the emission spectrum of hydrogen refer to [3, 29] or [34]).

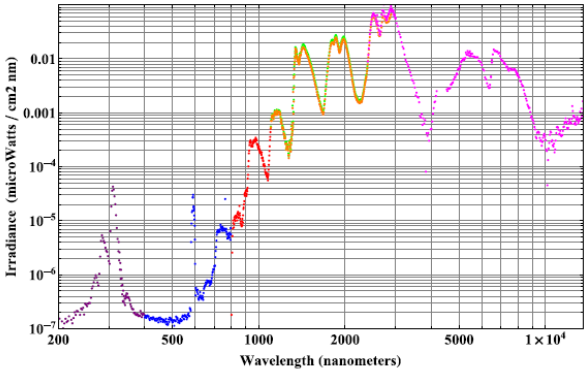

Figure 1.2: Compilation of the intensity calibrated hydrogen flame spectral data from 200 nm through 13,500 nm placed on a logelog plot allowing comparison of the magnitudes of the spectral peaks. Figure taken from reference [3]

The figure clearly shows that the intensity for longer wavelengths is much higher than the intensity for the UV range. This is why commercially available detection devices for hydrogen flames work with the infrared part of the spectrum, from $750nm$ to over $5000nm$ either alone or in combination with the UV light emission [40]. A sensor measuring infrared radiation is not suitable for flame detection because of the infrared radiation (thermal radiation) of the burner in the appliance. Strategies relying on the UV bands alone are reported to have drawbacks, including problems distinguishing between sunlight and flame emission [40]. This issue may be neglected for the given application, since the flame in a boiler burns in a closed chamber where no natural light is present. Another argument for using UV emission is that at a wavelength of $309nm$, the hydrogen flame spectrum shows the highest signal to noise ratio (see figure 4 in [3]).
Legal regulations require a certain response time of the flame monitoring system. The short response time of an optical sensor such as a UV sensor is the preferred solution for fulfilling those standards.

As mentioned above, no prior study has been found that reports experiences of using this sensor type in the given environment. The graduation project herein contributes to this novel field of research by reporting the sensor's response to hydrogen flames. The purpose of this work is to assess the feasibility of UV sensing technology for application in hydrogen-powered gas boilers. The focus is the influence of both the equivalence ratio and the sensor position on the sensor's output signal.
The following four questions are addressed:

1. Is the sensor sensitive enough to detect lean flames of $\phi = 0.5$ and $\dot{V} = 2\text{L/min}$ with resulting low radiation levels?
2. Is the sensor sensitive to changes in the equivalence ratio of $\Delta\phi = 0.05$?
3. How does the sensor signal depend on the position of the sensor with respect to the flame?
4. Can the dependence of sensor signal on sensor position be described analytically?

Questions 1 to 3 are the topics of an empirical study.
An experimental setup is designed, installed and used. It allows to measure the sensor's response to the flame as a function of three parameters that determine the position of the sensor compared to the flame. Said parameters are the horizontal and vertical distances between sensor and flame, and the inclination of the sensor. As the inlet gas mixture can be varied, the setup allows evaluation of the influence of the equivalence ratio of the flame on the sensor signal, too. Further, additional parameters such as the outlet velocity v_{outlet} of the unburned gas and the Reynolds number of the gas flow Re can be altered. Implemented thermocouples monitor the nozzle and burner head temperatures during the experiments. The burner is built in such a way that the nozzle can be changed. This makes it possible to work with flames of different sizes and shapes. For this research, studies are conducted that examine the sensor signal for different sensor positions and flames of different equivalence ratios.
Measurement results are compared to data obtained from chemiluminescence images of the flames that are taken during the respective measurements. This is done in order to validate empirical observations for the influence of the equivalence ratio on the sensor signal strength. The images display the intensity of UV light emission qualitatively or, if calibrated with a light source of known emission intensity, as absolute values. Due to time constraints, the calibration of the camera is outside the scope of this study and results are compared qualitatively.
To interpret the empirically observed influence of the sensor position on the signal strength, an analytical concept from *radiative heat transfer* theory is extended to the present work. This concept, the *View Factor (VF)* describes the transmission of radiation between two objects as a function of their geometry and their relative position. The View Factor between sensor and flame is developed as a function of the parameters that describe the position of the sensor with regard to the flame. The equation is evaluated for the same sensor positions for which experimental data is obtained.

This report is structured as follows. The next chapter presents the experimental setup that was designed for this research. The studies conducted are described in Chapter 3. Chapter 4 presents and discusses the empirical results of the work, and chapter 5 introduces the View Factor as a concept to describe the experimental observations. Chapter 6 concludes the findings of the research and proposes further investigations related to the research questions.

2

Experimental setup

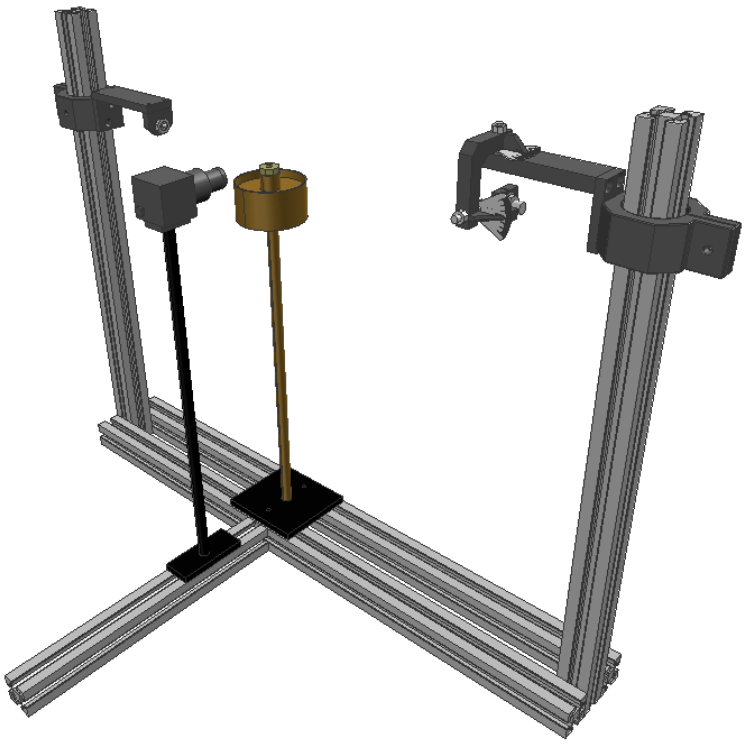

Figure 2.1: 3D model of experimental setup to study Bunsen like hydrogen-air flames. UV light radiation is measured with a UV sensor, and chemiluminescence images are taken with a camera that is equipped with an optical bandpass filter. A second UV sensor is used to control a shut-off valve that interrupts the hydrogen supply path if no flame is sensed.

Introduction

This chapter introduces and describes the experimental setup that was designed to study the influence of the flame's equivalence ratio and the position of the UV sensor on the sensor signal strength empirically. Figure 2.1 shows the 3D model of the setup, without gas supply path and data acquisition equipment. Figure 2.2 shows the connection scheme of the setup in a simplified sketch. Figure 2.3 is a photo of the complete setup. The setup includes the following components.

— A burner, which is equipped with a nozzle to produce a flame of desired shape and size.

— A UV light sensor, that measures the UV chemiluminescence emitted by the flame.

— A second UV sensor, which monitors whether a flame is present and that controls a magnetic shut-off valve in the hydrogen gas supply, for safety reasons.

— A charge-coupled device (CCD) camera, that is equipped with an optical bandpass filter to take images of UV radiation.

The listed components are assembled in a frame, that ensures an accurate positioning of the components relative to each other. Additionally, the frame stabilized the components against movements induced from the outside, to increase the safety of the setup.
In the following, the different components and their function are described in more detail.

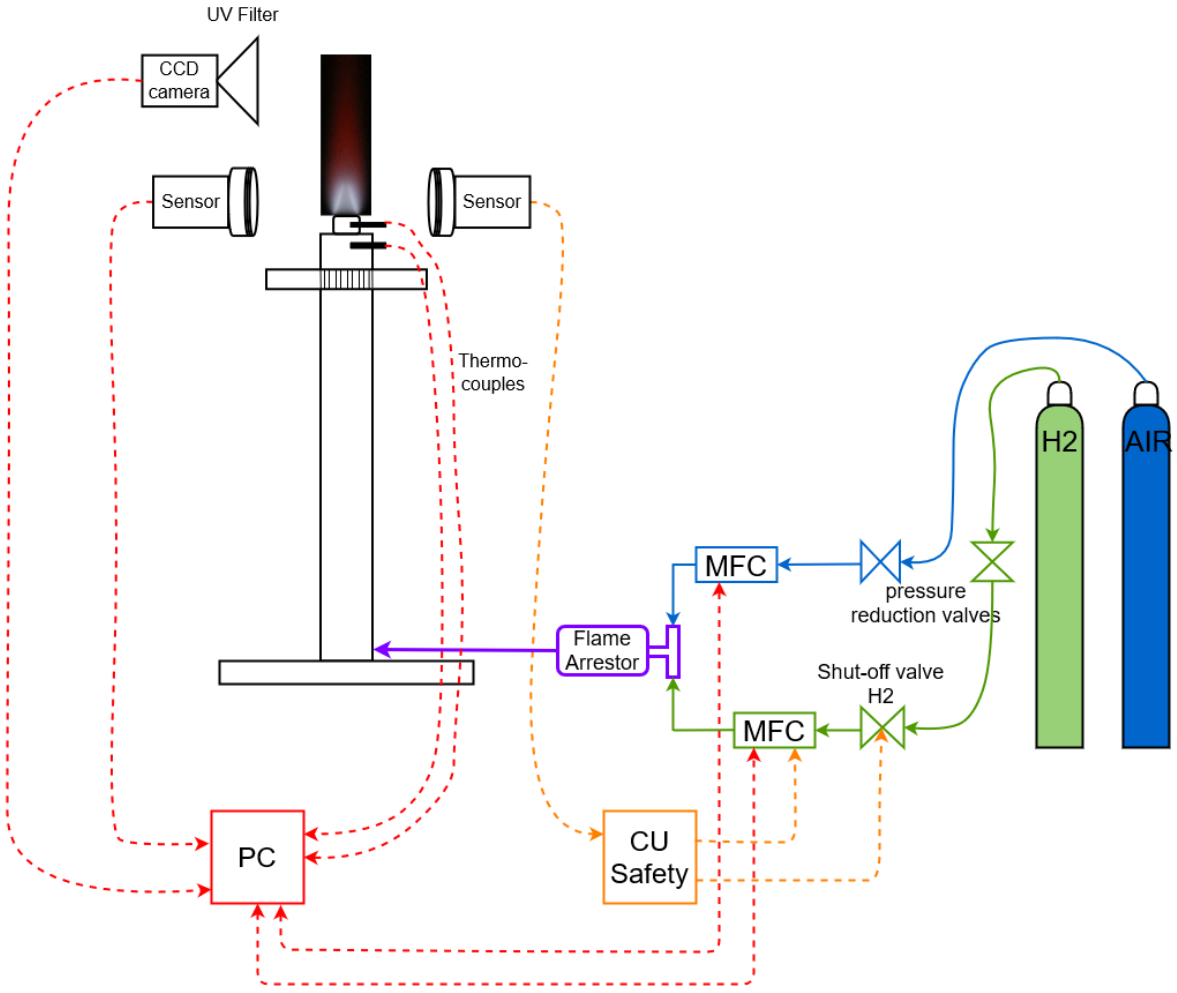

Figure 2.2: Schematic of the developed experimental setup to study premixed, laminar Bunsen-like hydrogen-air flames. Hydrogen and air are supplied from separate bottles. Gas flows are controlled by mass flow controllers and are mixed upstream of a flame arrestor. The gas mixture enters the burner pipe and flows through a ceramic honey comb before entering the nozzle. Two thermocouples are applied to the burner, one upstream of the nozzle and a second one in the nozzle rim. The measured temperatures are stored on a computer. UV light emission from the flame is measured by two UV sensors and with a CCD camera equipped with a bandpass filter. The signal of the first sensor and of the camera are stored on a computer, for further analysis of the data. The second UV sensor monitors whether the gas mixture is ignited. If a flame is present, a control unit opens two shut-off valves in the hydrogen supply path.

2.1. Burner

The following section describes the burner developed for experimenting with hydrogen flames. The requirements for the burner design are introduced and it is shown how the design of the burner components con-

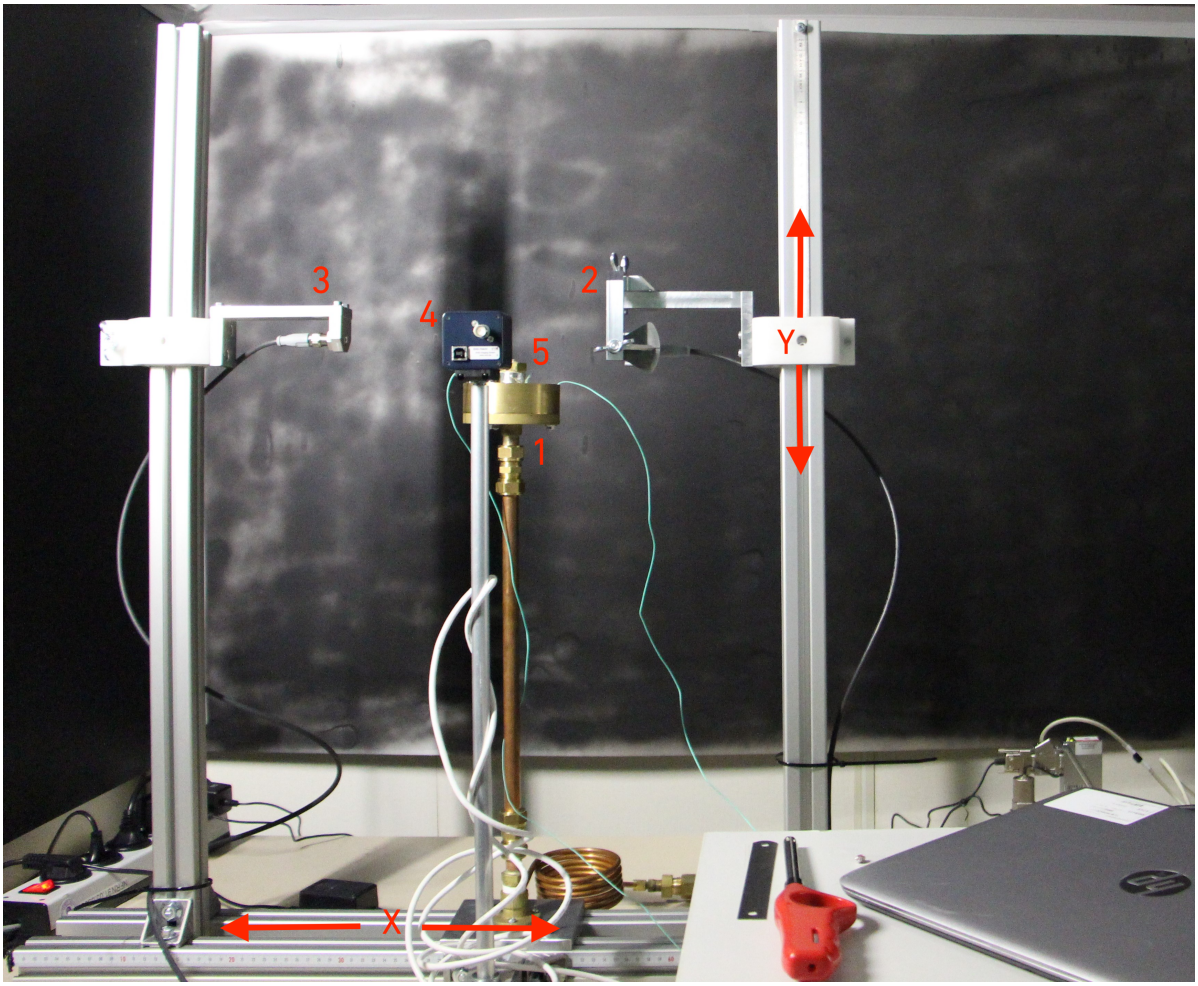

Figure 2.3: Developed experimental setup to study hydrogen-air flames. The burner (indicated with 1) and the nozzle (number 5) are designed for Bunsen like flames. UV light radiation is measured with a UV sensor (indicated with number 2), and chemiluminescence images are taken with a camera that is equipped with an optical bandpass filter (number 4). A second UV sensor (number 3) is used to control a shut-off valve that interrupts the hydrogen supply path if necessary.

tributes to fulfill these requirements. A technical drawing of the burner can be found in appendix A. The burner pipe is made of copper, the burner head and the nozzle are made of brass.

Burner pipe and gas supply

This work investigates premixed, laminar Bunsen-like hydrogen-air flames. In order to ensure that the flow is indeed laminar, and that both components of the gas mixture are fully mixed when being ignited, the mixing pipe and the burner pipe require a certain length. Figure 2.5 shows the mixing components of the gas supply path. Air and hydrogen are supplied from separate bottles. After both gases enter the push-in T-connector (indicated with number 8 in figure 2.12), they flow through a copper pipe with a diameter of $d_{pipe} = 4mm$. The pipe is $l_{pipe} = 1.5m$ long, to guarantee a homogeneous gas mix at the burner pipe inlet.
The gas flow requires a certain length to develop a laminar flow velocity profile. According to eq. (6.5) in [38], the ratio of pipe length to pipe diameter should be

$$\frac{l_{pipe}}{d_{pipe}} \approx 0.06 \cdot Re \tag{2.1}$$

to ensure a fully developed laminar flow. Since $Re \approx 800$ (see below), $0.06 \cdot Re = 48$. The burner pipe is $l_{pipe} = 486mm$ long, with $d_{pipe} = 13mm$. Hence, the ratio is

$$\frac{l_{pipe}}{d_{pipe}} = 37$$

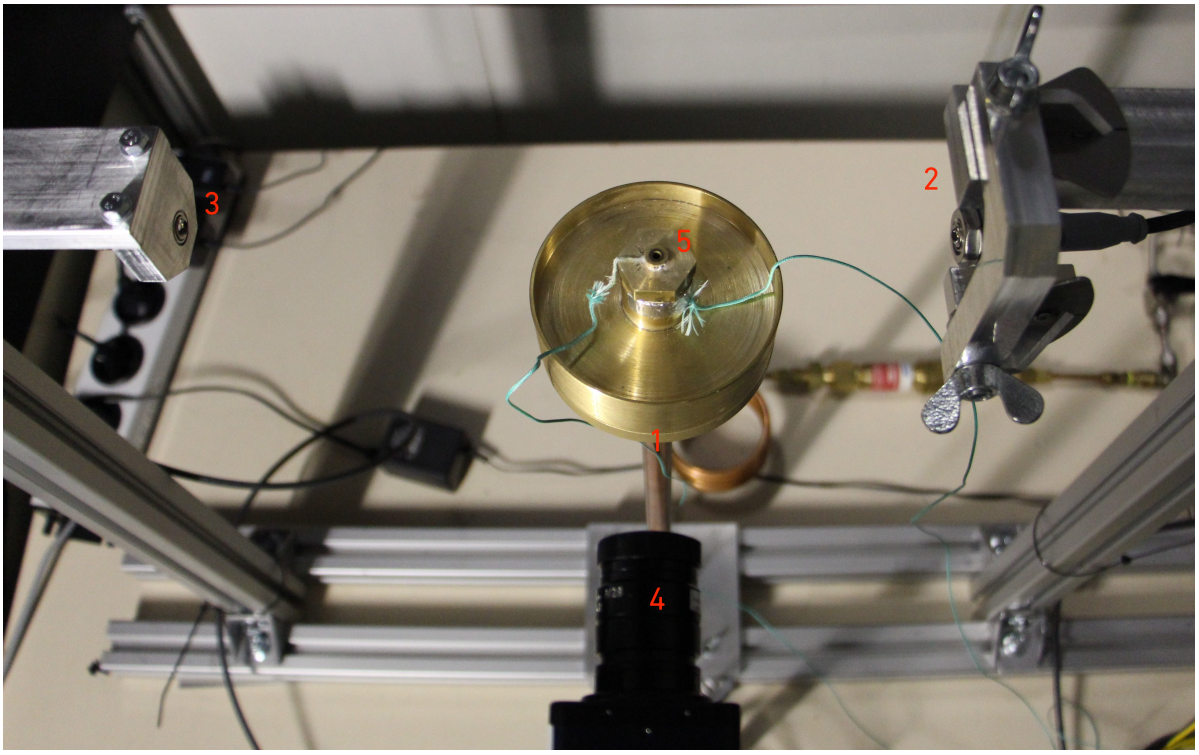

Figure 2.4: Setup from above, indicating how the measurement equipment sees the flame. 1: Burner with thermocouple, 2: UV Sensor for measurements, 3: Security UV sensor to control hydrogen supply, 4: UV camera, 5: Nozzle with thermocouple

which is below the calculated factor of 48. Thus, additional measures are taken to enhance laminar flow development.
A ceramic honey comb is placed at the end of the burner pipe, upstream of the nozzle. The honey comb has square channels, with channel diameter $d_{channel} = 1mm$ and length $l_{channel} = 10mm$. The second measure is the design of the nozzle, which is described in the following section. Judging from the resulting Bunsen flames, the flow profile can be described as fully developed.
For all measurements presented hereafter, the gas outlet velocity is $v_{\text{outlet}} = 475 \pm 5 \frac{cm}{s}$. This results in Reynolds numbers around $Re = 800$. According to [35] and [29], jet flames with this Reynolds number are laminar.

Nozzle

The decision to work with Bunsen-like flames stems from the following two reasons. Firstly, because a conical flame emits radially. This allows to place several measurement instruments around the burner without concerns about the influence of different points of view on the measured data. The second reason is the combustion monitoring method for the industrial reference device. To monitor the combustion in state-of-the-art gas boilers, only a special region of the burner plate is considered. The flames above this region of the burner plate show a shape similar to a Bunsen-like flame, because of the holes through which the gas enters the heat cell (see figure 2.6).
In order for the flame to have a Bunsen-like shape, the nozzle outlet has to be circular. Concerning the outlet diameter of the nozzle, the anchoring of the flame above the nozzle rim imposes limits on the possible range of sizes. The flame stabilizes at the position, where the outlet velocity of the unburned gas and the burning velocity of the gas mixture balance. For equivalence ratios from $0.5 \leq \phi \leq 1.2$, burning velocities for hydrogen flames are between 5 and 10 times higher than for methane flames (see figure 3.6 in [2] and [28]). Therefore, the risk of flame flashback is increased compared to the risk for hydrocarbon fuels such as methane. To avoid flashback, the outlet velocity of the unburned gas has to be sufficiently high. Hence, bigger nozzle outlet diameters require high volume flows and lead to increased gas consumption. Therefore, smaller diameters are favourable, to keep the gas consumption low.
However, small outlet diameters result in flames of smaller dimensions, which emit less light than bigger

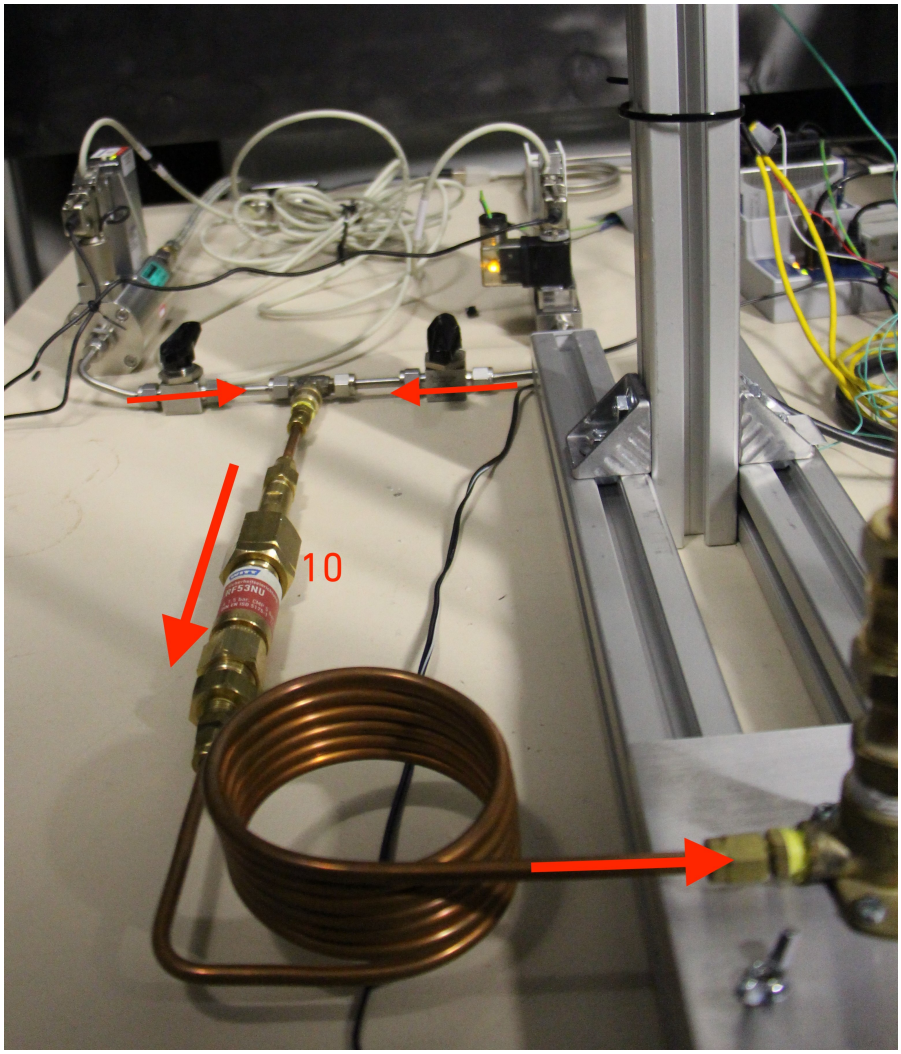

Figure 2.5: Hydrogen and Air are mixed with a push-in T-connector, subsequently the gas mix flows through a 1.5m long copper pipe before it enters the burner pipe.

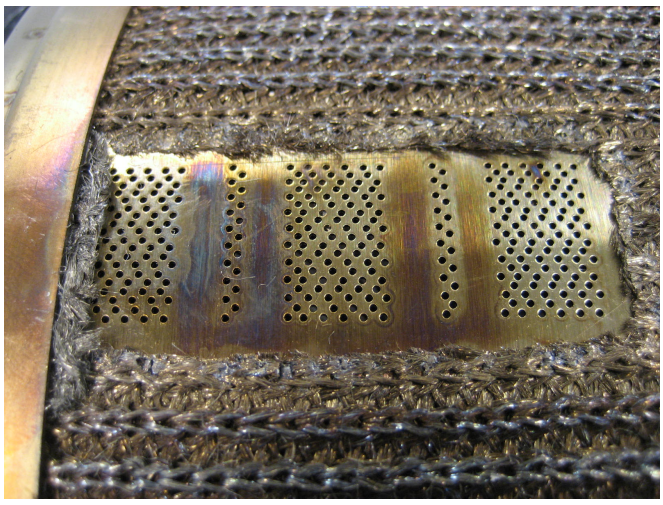

Figure 2.6: Modified burner plate of a gas boiler. Area above which the ionization current is measured to monitor the fuel - air ratio of the flame.

flames. Concerning the functionality of the setup, it has to be ensured that light emission intensities are high enough for the light detecting devices such as the UV sensor and the UV camera.
In addition to that, a smaller diameter leads to increased events of flame blow off for lean equivalence ratios. A compromise of the stated limitations is a diameter of $d_N = 3mm$, leading to an outlet area of $A_N = 0.07cm^2$. With the chosen nozzle size and volume flow, flames with equivalence ratios $\phi \geq 0.45$ can be ignited. An upper limit of the equivalence ratio was not encountered while working with the presented nozzle.

Figure 2.7 shows a cross section of the nozzle.
The burner pipe leading the gas flow to the nozzle has a diameter that is a factor four bigger than the nozzle outlet. Therefore, the gas is led through a piece with the geometry of a truncated cone before entering a 26 mm long channel with the same diameter as the nozzle outlet (visible in figure 2.7). The intention is to enhance a laminar flow.
To ensure that the flame stabilizes above the nozzle outlet, the outlet is not realized as a thin, sharp edge, instead the nozzle rim is thick, as figure 2.4 shows. The rim is $3mm$ high, with a wall thickness of $1.5mm$. The additional material mass increases the heat release that is required to anchor the flame at the desired position.
It is of great importance that the flame is axisymmetric. Considering the outlet velocity of the unburned gas mixture, even small inaccuracies in the circular opening cause fluctuations of the flame. Therefore, the nozzle has to be manufactured carefully.

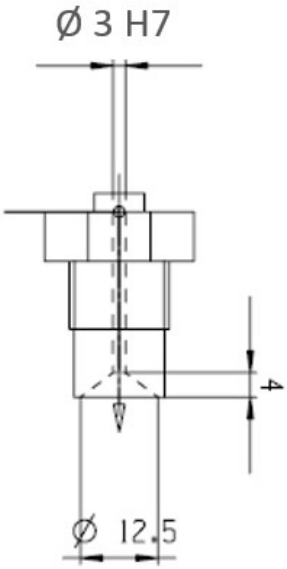

Figure 2.7: Technical drawing of the nozzle cross section.

Two thermocouples are attached to the nozzle to measure the temperature of the material at the respective positions. One thermocouple is placed directly in the burner rim, the second is attached further upstream, where the nozzle is screwed into the burner head (see figures 2.2 and 2.4).

2.2. UV sensor

The sensor which has been used in the presented work is the broadband UV photodetector *TOCON ABC1* from the company *sglux*. Figure 2.8 shows the two components of the *TOCON ABC1*. The sensor is made from the ceramic silicon carbide, a semiconductor material. The photodetector is sold with an integrated amplifier that converts the incident UV light to a voltage signal in the range of 0 V and 5 V. The lower detection limit is given as $1.8pW/cm^2$. The saturation limit is $18nW/cm^2$.

(a) Steel housing with M12x1 thread.

(b) UV photodiode with concentrator lens cap.

Figure 2.8: Steel housing and UV photodiode with concentrator lens cap. Images taken from [30].

To enhance light absorption, a concentrator lens is placed in front of the sensor (see figure 2.8b). Incident light beams contribute differently to the sensor signal, according to the angle with which they enter the lens. This characteristic is described as *Field of View (FoV)*. Figure 2.10 shows the FoV of the sensor. Since the effect of the FoV will play a role for the discussion of the measurement results in chapter 4, it will be described in more detail in that part of the report.
The sensor is most sensitive at wavelengths of $\lambda = 280nm$. The responsitivity at this wavelength is typically $S_{max} = 280mV/nW/cm^2$. The spectral response is shown in figure 2.9. At $\lambda = 309nm$, where hydrogen flames emit UV light, the spectral response is approximately 83% of the maximum responsivity, which leads to a responsivity of $S_{309nm} \approx 232mV/nW/cm^2$.
The offset voltage that is measurable in the absence of illumination is $V_{\text{offset}} = 700\mu V$. All given technical information is taken from the data sheet provided by *sglux* [30].

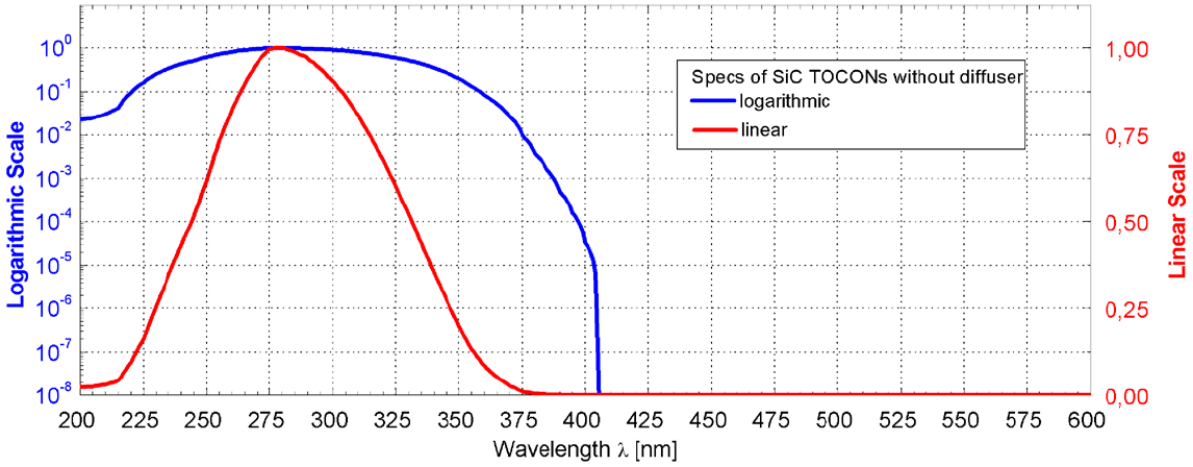

Figure 2.9: Spectral response function of UV sensor *TOCON ABC1*, provided from the data sheet of the sensor [30]. At $309nm$, the spectral response is ~83%.

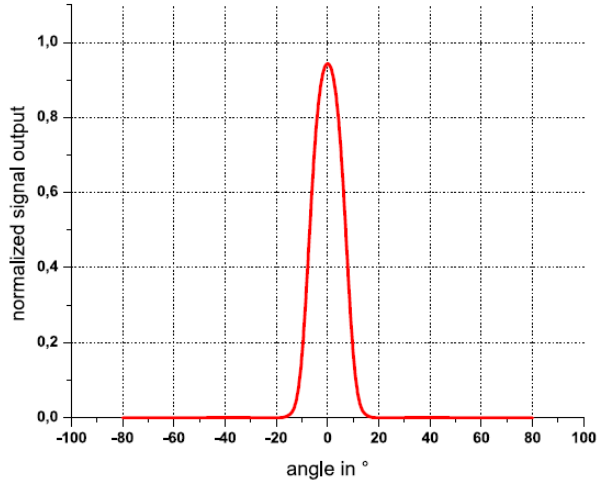

Figure 2.10: FoV of UV sensor *TOCON ABC1*, retrieved from the data sheet of the sensor [30].

Figure 2.11 shows the sensor holder. The position of the sensor is variable in height, indicated as Y direction. In addition, the holder is built in such a way that the sensor can be tilted upwards and downwards, indicated with angle α and to the left or right, indicated as angle β. The sign of α indicates the direction of inclination. $\alpha < 0°$ indicates a tilt towards the base of the flame, $\alpha > 0°$ indicates tilting the sensor towards the flame tip.

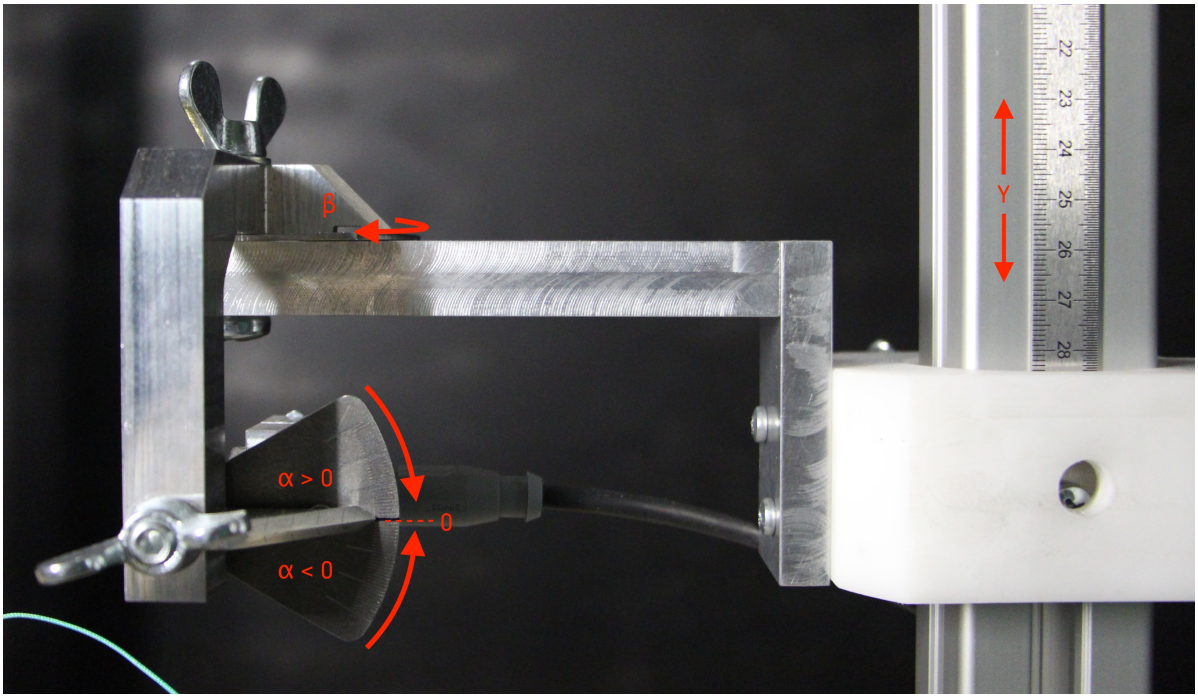

Figure 2.11: Sensor holder. The position of the sensor can be altered in height (Y coordinate), and the sensor can be tilted up and down (angle α), as to the left and to the right (β).

2.3. UV camera

To reference UV light emission measured with the UV sensor, chemiluminescence images are taken with a CCD camera. Deducting emission intensities from chemiluminescence images is a common method in combustion research (see for example references [4, 5, 17, 32, 36, 41, 42]).
The purchased camera is the *EHD-704UV* model from *EHD imaging*. It is equipped with a $25mm$ F/2.8 UV lens (*EHD-UV2528B*) and an optical bandpass filter with centre wavelength of $310 \pm 2nm$ and FWHM of $10nm$ (see [13]). The *ArtViewer* software is used to work with the camera. Picture size is 1360 x 1024 pixels, pictures are taken as 8-bit grey scale images. Further descriptions of the processing of the images is given in section 3.3.
The camera is placed perpendicular to the axis of both UV sensors, see figure 2.4. The distance from which the camera looks at the flame is variable, since the camera hold is placed on a table that can be moved. The exact position is indicated with a scale, comparable to that shown in figure 2.13a.

Calibration

The images taken with the camera are matrices of 8-bit grey scale values for each pixel of the image. They do not give absolute values for the UV radiation of the flame. To translate the grey scale values to values for UV irradiance, the camera has to be calibrated. Only a few studies published OH^* radiation values of hydrogen-air flames, such as [8, 32, 41]. In the last of the studies mentioned, Zhao et al. calibrate their optical system against a light source of known radiance, an integrating sphere radiance source. Zhao et al. used a black body in an earlier study to calibrate their optical system [42], as well. Since no integrating sphere radiance source is available, an alternative idea is to use a tungsten ribbon lamp, that behaves like a black body. The lamp has been calibrated, and the black body temperature is known as a function of the supplied current.
The transmission efficiency of the optical bandpass filter is known from the datasheet of the filter. For an accurate calibration, the camera has to be positioned at the exact same distance to the ribbon lamp as to the hydrogen-air flame, respectively. Therefore it is necessary to find a method how to measure both distances, before calibrating the camera. Due to time constraints, the calibration of the camera is not part of this work and left for further research.

2.4. Mass flow controller

The mass flow controller (MFC) is a crucial part of the gas supply path. To work with flames of known equivalence ratio and outlet velocity, the volume flows of both mixture components, hydrogen and air, are controlled by a MFC. Both controllers are connected to the *LabVIEW* software described in section 3.2. The MFC for hydrogen is equipped with a shut-off valve that is closed when the UV sensor signal indicates the absence of a flame, to increase safety.

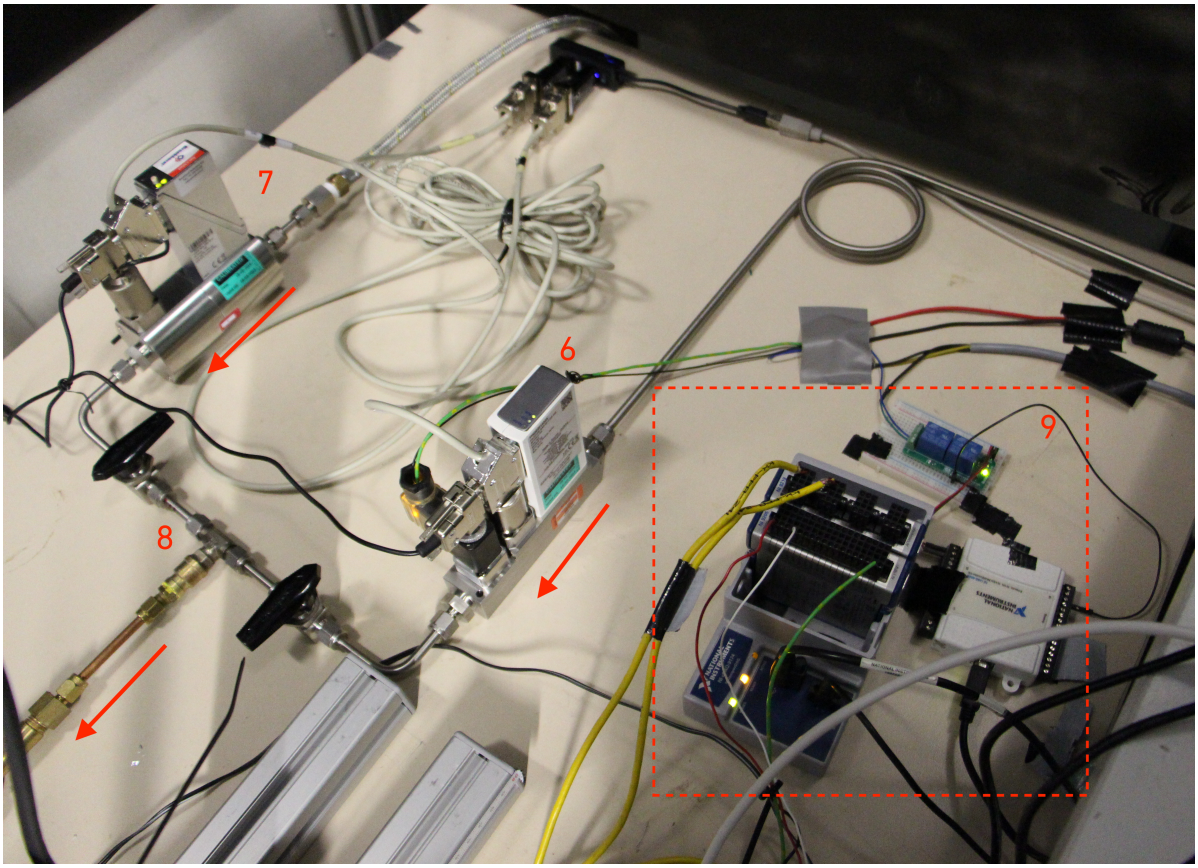

Figure 2.12: Hydrogen and air enter the setup separately, their volume flow is controlled by mass flow controllers (6 for hydrogen and 7 for air). The gasses are mixed at the T-connector (8) ~1.5m upstream of the burner. Measurement data is acquired with the components visible in 9. Also the security shut-off valve (not visible) in the hydrogen path is controlled via 9.

For both gas flows, a MFC from *Bronkhorst* was purchased. For the air flow, the selected model is the *EL-FLOW Base F-202BB* with a flow range of $2-100$ ln/min and a given accuracy of $\pm 1\%$ of the full scale, hence ± 1 ln/min. For the hydrogen gas flow, a different model was chosen. The *EL-FLOW Prestige FG-201CS* has a flow range of $0.4-20$ ln/min with an indicated accuracy of ± 0.02ln/min and additional $\pm 0.5\%$ of the read gas flow. The flow ranges were determined according to the desired total volume flow, which, together with the outlet diameter of the nozzle, determines the outlet velocity of the unburned gas mixture v_{outlet}. If values for v_{outlet} are too high, the mixture can not be ignited. If they are too small, the risk for flashback is increased.
Both flow controllers have been calibrated before delivery. The flow controllers are indicated by numbers 6 and 7 in figure 2.12.

2.5. Safety measures

Burning hydrogen implies risks of explosion, since hydrogen is explosive for a wide range of concentrations from 4–75 vol% [26] and requires little energy to react with the oxygen in the air ($0.02 mJ$ for a stoichiometric mixture, one thousand times less than methane [31]). Therefore, accumulation of unburned hydrogen has to be prevented. To avoid damages to components and staff, several measures are taken.
As figures 2.1, 2.3 and 2.4 show, a second UV sensor is observing the flame. Its output signal is connected to the Control Unit (CU) and compared to a fixed threshold signal strength. Only when the signal strength is above the threshold value, the CU powers a normally closed magnetic shut-off valve that is placed in the hydrogen supply path. A second shut-off valve that is controlled in the same way is implemented in the hydrogen MFC.
The entire experimental setup is placed under an exhaust duct, that covers a large area above the setup and that is closed at three sides. In addition to the safety aspect, the duct hinders the presence of natural light in the surroundings of the experiment, to prevent a falsification of the flame measurements. The side walls are painted with carbon black, to minimize the influence of reflections. The duct is build such, that unburned hydrogen is led directly to the exhaust gas subtraction network. An additional measure to avoid accumulation of unburned hydrogen in the surroundings of the setup is a gas detector, that gives an alarm if hydrogen leaves the area of the duct.
To avoid explosions due to flame flashback, a flame arrestor (*RF53NU* from *Witt Gas*) is placed in the gas supply downstream of the T-connector where both hydrogen and air are mixed (visible in figure 2.5, indicated with number 10).

2.6. Uncertainties

Several components of the setup induce inaccuracies that have to be taken into account when the empirical data is interpreted later. These sources are identified and discussed.

Mass flow controllers

The gas flow is controlled by the flow controllers described in section 2.4. These instruments are accurate only to a certain degree. This has two consequences.

Firstly, the real gas flow deviates from the set point of operation. This affects the equivalence ratio and has to be taken into account when comparing data from measurements that were intentionally carried out with the same equivalence ratio. The same accounts for emission intensity values from the chemiluminescence images. To avoid errors, data is analysed with regard to the mean measured equivalence ratio, instead of the equivalence ratio calculated from the set gas flow values.
The actual equivalence ratio is always lower than the set value. In general, the deviation is higher for higher values of ϕ. For the studies that have been carried out, the minimum deviation was approximately -0.85% and the maximum deviation was about -4.9% of the set equivalence ratio.

Secondly, the gas flow is subject to fluctuations that are reflected in the signal measured by the sensor and in unstable flame heights. Consequently, mean values are calculated and presented with error bars indicating the standard deviation of experimentally obtained data. The observed standard deviation of the sensor signal lies between $1.8 mV$ and $4.2 mV$. Related to the respective mean signal strength, this results in higher deviations for lower equivalence ratios, since the signal strength increases with the equivalence ratio. The highest relative deviation is 3.2%, the lowest is 0.32%.
The implementation of chambers in the supply path could even out these fluctuation and is thus recommended to further improving the setup.

UV sensor

Another source of uncertainty is the sensor described in section 2.2. It is observed that the measured signal is subject to fluctuations that are independent of the flame, since they are present even when measuring the dark background. Another observation is a non-zero signal strength in the case of an absent flame. This is referred to as offset voltage, mentioned earlier (see section 2.2). To exclude the background signal from the signal strength attributed to the flame, the dark signal is recorded before each set of experiments. The obtained average background signal is subtracted from the experimental data subsequently. At only $0.41 mV$, the average background signal is almost negligible compared to the signal strength measured during the ex-

periments.
Final values for signal strength are mean values with the signal fluctuation expressed as the standard deviation presented in error bars.

Positioning of UV sensor

The sensors position is adjusted manually. The scales used to modulate the location are visible in figure 2.13 and in figure 2.11 for the Y direction and tilt angles. The scales allow the following levels of precision.

- X direction: $1 \pm 0.5mm$
- Y direction: $0.5 \pm 0.5mm$
- Tilt angle α: $1 \pm 1°$

Accordingly, data is presented with error bars indicating the uncertainties in the sensor position.

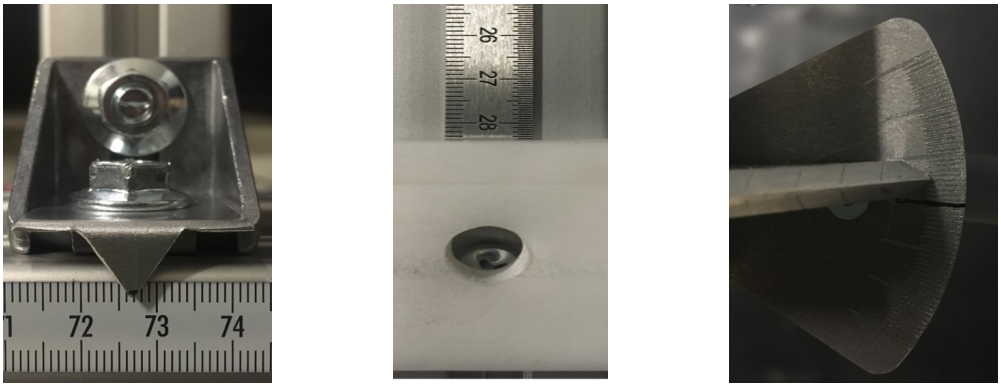

(a) Indicator on the X axis scale. (b) Indicator on the Y axis scale. (c) Indicator on the α scale.

Figure 2.13: To position the sensor at the desired location, scales are applied to the X and Y axis and for the tilt angle axis. Indicators mark the position.

3

Experimental method and conducted studies

Introduction

The following chapter describes how experiments are done, what data is obtained, how it is processed and how the chemiluminescence images are taken and processed. Then, the conducted parameter studies are described.

3.1. Testing procedure

Measurements were started only after a warming up period of the mass flow controllers. For every experimental series, the sensor signal induced by the dark background of the setup is subtracted from the measured signal. Therefore, the sensor signal is recorded without a present flame. Before starting an experimental series, the signal is logged for one minute, this is repeated five times. The mean signal strength is obtained and subtracted from the experimental data.
Each measurement is repeated five times, and the sensor signal is measured for four minutes. After analyzing the influence of the duration of the measurement on signal fluctuations, time was decreased to three minutes. The described procedure was determined on the basis of advice from the first author of references [9] and [10].
For lean flames with $\phi = 0.5 - 1.0$, is was observed that differences in the starting temperature of the burner have a non-negligible influence on the measured sensor signal. Hence, measurements are started at set burner temperatures after a cooling down period in case of serial experiments, in order to have equal starting conditions.

3.2. Data acquisition and data analysis

To analyze the experimentally obtained information on the UV light emissions, a *LabVIEW* program has been written. It does not only acquire and store data, it also controls the gas flows of hydrogen and air. It stores the data described in table 3.1. The frequency of the data acquisition is variable within the frequency limits of each connected component and was set to $4\,Hz$. The following *National Instruments* products are used to execute the $LabVIEW$ commands: *NI 9219* to store the temperature measurements obtained with the thermocouples and *NI 9205* for the incoming signal from both UV sensors and the outgoing signal to the magnetic valve.
The data acquisition equipment is shown in figure 2.12, indicated with a dashed line and number 9. The LabVIEW program can be found in Appendix C.

The recorded data has been used as raw data or to calculate other parameters. Very important for further analysis of the experimental data is the flame equivalence ratio ϕ, which is calculated from the measured gas flows according to 3.1 and 3.2. ϕ is defined as

$$\phi = \frac{Y_{H_2} / Y_{Air}}{(Y_{H_2} / Y_{Air})_{st}} \tag{3.1}$$

Table 3.1: Parameters acquired during measurements

Parameter	Details	Unit
Time	Time since start of measurement	[sec]
Sensors signal	Safety Sensor	[V]
	Measurement Sensor	[V]
	Signal Threshold	[V]
Gas Flow	Air, set point	[L/min]
	Air, actual flow	[L/min]
	H_2, set point	[L/min]
	H_2, actual flow	[L/min]
Temperature	Nozzle Rim	[°C]
	Burner Head	[°C]

where Y_i is the mass fraction and the index *st* stands for stoichiometric conditions. The mass fraction is obtained from the respective mass flows $\dot{m}$ by

$$Y_{H_2} = \frac{\dot{m}_{H_2}}{\dot{m}_{gasmix}} \tag{3.2}$$

The mass flow for each component is calculated with the volume flow $\dot{V}_i$ data obtained from the MFC and the density ρ_i of the gas, assuming ambient temperature as $T = 20°C$ and pressure $p = 1$atm.
The mass flow controllers require approximately 60 seconds to reach a constant flow. Hence, this initial period of the measurements is not taken into account for the data analysis. For the remaining period, mean values and standard deviations are calculated. Since each measurement is repeated five times, the method results in five mean values for the desired parameter. The final value is the average of these five values. A more detailed description of the experimental procedure is given in section 3.1 of chapter 3.

3.3. Image processing and conversion of line-of-sight data

As stated before, light emission intensities from the hydrogen flames are obtained from chemiluminescence images to have reference data for the ϕ - signal curve of the sensor. The images are taken with the CCD camera described above and further processed the following way.

1. Background irradiation is subtracted with an image taken in absence of a flame.
2. The image is cropped to the relevant area, chosen as 425x700 pixel.
3. The average of 10 images is calculated to even out fluctuations of the flame.
4. A filter is used to reduce high-frequency noise induced by the gain of the camera software.
5. Because of camera misalignment, images are rotated to ensure a vertical flame axis which is essential for Abel inversion of the intensity values.

Steps 1 to 3 are realized with the software *ImageJ*. In step 3, the average of 10 images is taken. The appropriate number of images was determine in the following way. For an increasing number of images of the same flame, two flame locations have been chosen, and their average pixel value was computed. For each image that has been added, the standard deviation from the mean was calculated and plotted as a percentage of the mean pixel value. For both locations, the deviation decreased when 10 images have been averaged. The chosen locations are one pixel at the flame base and one pixel at the flame tip.
The filter used in step 4 replaces each pixel value by the mean value of the neighbouring pixels, hence it smooths the image. As a last step, images taken with different exposure times are normalized to a common time of $1ms$. The gain is constant for every image.
The CCD camera takes line-of-sight images. To get spatially resolved intensity images, the line-of-sight values have to be deconvoluted mathematically. An inverse Abel transform is used to reconstruct the emission values. The code was retrieved from the *PyAbel* package for *Python*. The *3-point method* is used, because it is recommended by several studies (see for example [7, 21, 41]).
Pictures are taken for equivalence ratios from $\phi_{\min} = 0.5$ to $\phi_{\max} \approx 1.7$. They can be found in Appendix B.

3.4. Conducted studies

To evaluate the feasibility of the application of a UV sensor for flame detection and monitoring in a gas boiler, the response of the UV sensor to changes in its position and to changes in equivalence ratio ϕ of the flame is investigated. Therefore, the respective measurements are conducted.
The position of the UV sensor is altered, while the flame parameters, and thus the emission intensity, remain constant. The position of the sensor is a function of the horizontal and vertical distance to the burner, and of the tilt angle of the sensor. The horizontal and vertical distance is expressed in the X and the Y coordinate of the sensor position, respectively, the tilt angle is given as angle α. The mentioned parameters are shown in figures 2.3 and 2.11 in chapter 2.
To determine the influence of each parameter on the signal strength, the position of the sensor is varied by changing only one parameter while the other two are left unchanged. The experiments are conducted with a laminar premixed Bunsen-like hydrogen-air flame with equivalence ratio $\phi = 0.5$. The velocity of the unburned gas is $v_{outlet} = 470 cm/s$, therefore the Reynolds number is calculated as $Re \approx 800$. The equivalence ratio is chosen because it is expected to be the lower limit of the operating area of the appliance. Since for this range of ϕ leaner flames emit less UV radiation, it is important to test at these conditions to evaluate the sensor signal for low intensity flames. During the measurements of flames with different equivalent ratios, the sensor position and the velocity of the unburned gas are kept constant.

3.4.1. Equivalence ratio

The sensor's response to different equivalence ratios is tested. While ϕ was increased, the sensor's position is kept constant at $X = 100 mm$, $Y = 10 mm$ and $\alpha = 0°$. This position is chosen because it is the position of the sensor in the reference boiler. Although the expected operational equivalence ratios range from $\phi = 0.5 - 0.75$ only, the sensor curve is obtained for $\phi_{min} = 0.5$ to $\phi_{max} = 1.7$, to see for which equivalence ratio the signal peak occurs. The chosen step size was 0.5, which is considered small enough to study the behaviour of the sensor for changes in equivalence ratio. The measured curve is displayed and discussed in chapter 4, figure 4.1.

3.4.2. Distance to burner rim

The relation between sensor signal strength and horizontal distance from the burner rim is tested. While the X coordinate of the sensor is altered, flames are observed from a constant height of $Y = 10\ mm$, and with 0° inclination. This configuration reflects the position of the sensor in a reference gas boiler.
The measurements are performed for a range from $X_{min} = 30 mm$ to $X_{max} = 150 mm$ with a step size of $30 mm$. The range is chosen considering possible positions for the sensor in the developed appliance. Figure 4.9 in chapter 4 displays the obtained data for the UV sensor signal strength, plotted versus the distance between sensor and burner rim.

3.4.3. Height above burner rim

Next, the relation between signal strength and the height at which the sensor is observing the flame is examined. For the whole set of experiments, the horizontal distance from sensor to burner rim is kept as $X = 100\ mm$, the tilt angle is constantly $\alpha = 0°$.
Measurements are done from $Y_{min} = 0 mm$ to $Y_{max} = 50 mm$, with initial step size of $10 mm$ and additional measurements for $Y = 5 mm$, $8 mm$, $12 mm$, $15 mm$ and $25 mm$. This range is chosen according to possible design options for the developed appliance. Figure 4.11 in chapter 4 displays the obtained data for the UV sensor signal strength plotted versus the height of the sensor above the burner rim.

3.4.4. Tilt angle

The third parameter that influences the incident emission on the sensor is the tilt angle α. While α is varied, the sensor is positioned at a horizontal distance of $X = 100\ mm$ and at a height $Y = 10 mm$ above the burner rim. Like for the experiments described above, this parameter choice is motivated by possible appliance design concepts.
Since the sensor view field is 10° wide, the tilt angle is varied between $\alpha_{min} = -5°$ and $\alpha_{max} = 5°$, in steps of 1°. Negative angles describe tilting the sensor downwards, positive angles tilting it upwards (refer to figure 2.11 in chapter 2). Figures 4.13 and 4.15 in chapter 4 display the obtained data for the UV sensor signal strength plotted versus α.

4

Results and discussion of experimental studies

Introduction

The following chapter presents and discusses the findings of the empirical research. First, the influence of the equivalence ratio on the sensor signal is discussed. The obtained ϕ-signal sensor curve is presented and compared to the integrated line-of-sight intensity values acquired from the chemiluminescence images. Subsequently, the influence of the sensor position is evaluated. The experimentally obtained curves are presented and discussed. In chapter 5, the same curves are built using the View Factor equation and both curves are compared.
The results discussed below are considered in chapter 6, where the feasibility of using UV sensor technology for detection and monitoring of hydrogen-air flames in gas boilers is assessed.
For a description of the experimental procedure refer back to section 3.1 in chapter 3. For details about each study, refer to the same chapter.

4.1. Equivalence ratio and signal strength

Figures 4.1 and 4.3 show the ϕ-signal curve of experimental sensor data and chemiluminescence images data for equivalence ratios from $\phi = 0.5$ until $\phi \approx 1.7$. Due to inaccuracies of the mass flow controllers, the actual value for ϕ deviates from the set value. Data points such as $\phi = 0.977$ and $\phi = 1.26$ are results of this deviation. Both measurements have been done for the same set value as for their adjacent data points, but appear as additional measurements, since results in plots refer to actual values, not to set values.
The images are taken from the same distance at which the sensor is placed ($X = 100mm$, $Y = 10mm$) to avoid differences due to the influence of the transmission distance the light has to travel.

The dashed red line in figure 4.1 shows the polynomial fitted to the sensor output data S_{out} given in mV. The sensor signal increases with increasing equivalence ratio up until $\phi = 1.26$. After this peak, a small decay is visible and the signal reaches a plateau where $S_{out} \approx 667mV$.
The curve is almost linear until $\phi \approx 1.12$. Data points that deviate most are at $\phi = 0.977$ and $\phi = 1.02$. It is visible that $S_{out,0.977} > S_{out,1.02}$, which is against the trend of increasing sensor signal for higher values of ϕ.
Examination of the conditions during the respective measurements show, that the nozzle temperature for both measurements deviates from each other. $T_{nozzle,0.977} = 60.1°C$, whereas $T_{nozzle,1.02} = 40.5°C$. Thus, the nozzle was almost $20°C$ warmer for $\phi = 0.977$. The observed dependence of sensor signal strength and nozzle temperature might be related to an increase in $[OH^*]$, which is the concentration of the radical responsible for the chemiluminescence in the UV light spectrum. The nozzle temperature has an influence on the outlet temperature of the unburned gas, which in turn has an influence on the concentration of the radical (see reference [23]). The temperature dependence of the sensor signal strength was observed earlier, consequently a cooling down period was implemented in the experimental procedure. At the beginning of each new measurement T_{nozzle} was screened, however it appears that it was not sufficiently low for the $\phi = 0.977$ measurement.

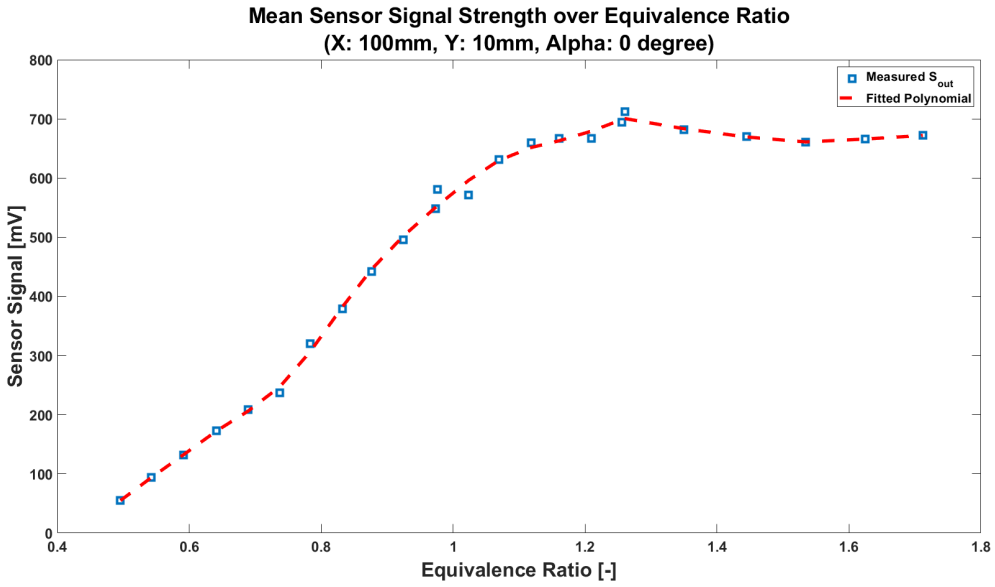

Figure 4.1: ϕ-signal curve fitted to experimental sensor data S_{out} in mV for equivalence ratios from $\phi = 0.5$ to $\phi \approx 1.7$. The sensor is placed at X = 100 mm horizontal distance and Y = 10 mm vertical distance from the flame. The curve reveals a constant increase for equivalent ratios up to $\phi = 1.26$ and flattens subsequently.

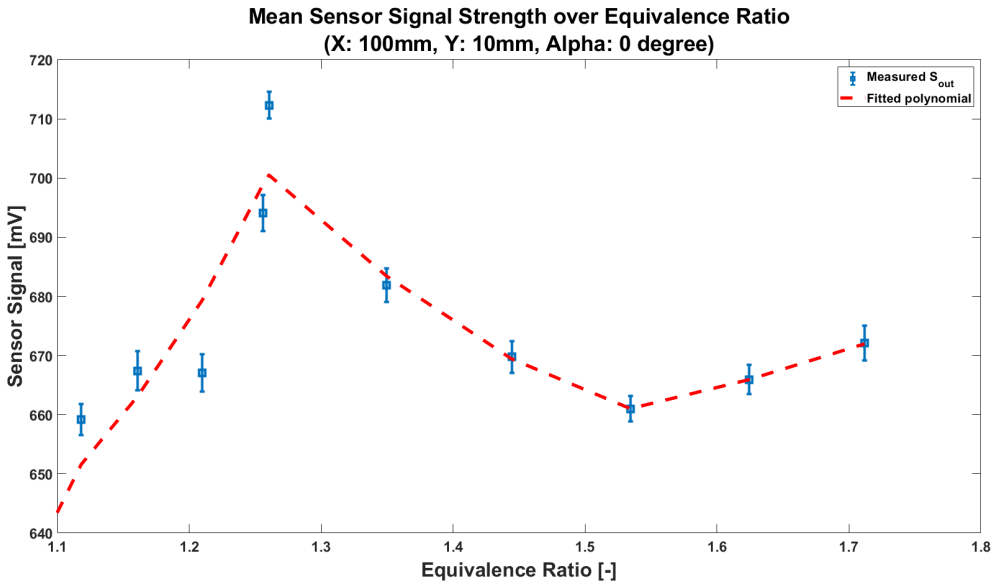

Figure 4.2: ϕ-signal curve of experimental sensor data S_{out} in mV for equivalence ratios from $\phi = 1.1$ until $\phi \approx 1.7$. Horizontal error bars indicate standard deviations for the equivalence ratio, vertical bars show the standard fluctuation of the measured sensor signal. Curve peaks at $\phi \approx 1.25$, subsequently decreases and finally increases again.

Figure 4.2 shows a close up of the curve for rich flames. Horizontal error bars indicate standard deviations for the equivalence ratio, vertical bars show the standard fluctuation of the measured sensor signal. The curve is fitted to the mean signal strength.
The peak for $\phi = 1.26$ seems unreasonably high when compared to S_{out} for $\phi = 1.256$. Here, the temperature difference is not as significant as for the observation above. $T_{nozzle,1.256} = 46.8°C$ and $T_{nozzle,1.26} = 48.7°C$. Hence, the explanation for this observation remains unclear. A generally increased S_{out} value is measured for equivalence ratios around $\phi = 1.3$ with respect to the adjacent equivalence ratios. The signal deviation for the

remaining regions $1.1 < \phi < 1.25$ and $1.4 < \phi < 1.75$ is only $S_{out,1.7} - S_{out,1.12} \approx 13mV$, which is why it appears as a plateau in figure 4.1. The last to mention observation is the slight increase for $1.5 < \phi < 1.7$.
To understand whether the discussed observations stem from irregularities of the experiment or from the chemiluminescence intensity itself, it would be interesting to compare the measurement results to other experimental data, or to simulated values. Unfortunately, no such data has been found in literature. Previous studies examined OH^* concentrations and reaction and excitation rates (refer to [8, 20, 22] and [23]) and spatial distribution of emission intensities (see [19, 23, 32], and [41]), but no report on integrated emission for different equivalence ratios is found.

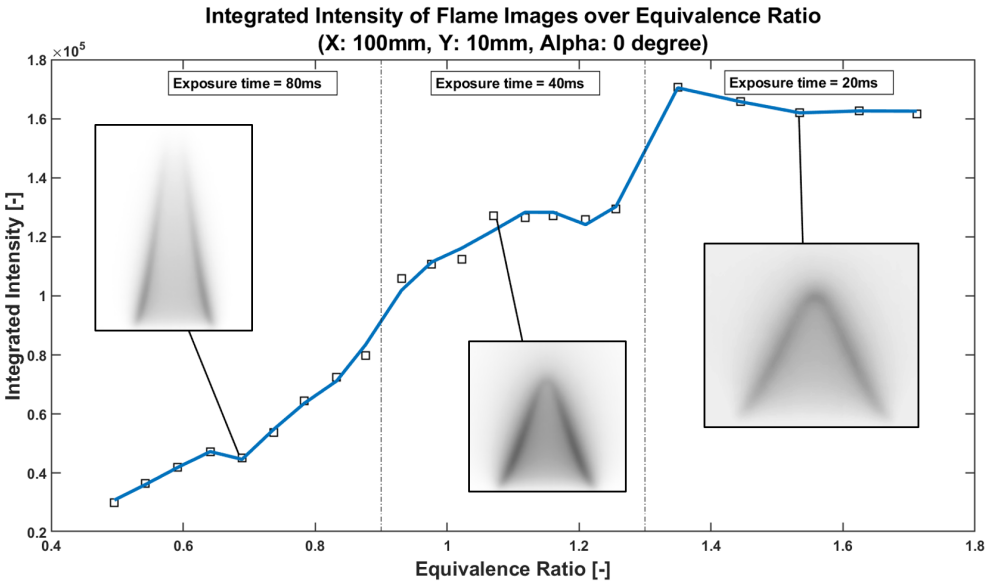

Figure 4.3: ϕ-signal curve of chemiluminescence image data (intensity integrated over whole image) for equivalence ratios from $\phi = 0.5$ to $\phi \approx 1.7$. The images are taken from the same distance to the flame at which the sensor is placed, while the signal strength is measured ($X = 100mm$, $Y = 10mm$). Curve reveals a general increase in measured intensity for $\phi \leq 1.07$ then values stagnate until a sudden peak at $\phi = 1.35$. Subsequently, intensity increases and curve flattens. Vertical lines divide images according to the set exposure time. Example chemiluminescence images (inverted) for $\phi = 0.69$, $\phi = 1.07$ and $\phi = 1.53$.

The solid blue line in figure 4.3 corresponds to the integrated line-of-sight intensity values from the UV chemiluminescence images. An example image is shown in figure 4.4. Pixel intensity values range from 0 to 255, corresponding to an 8-bit format. For each equivalence ratio, the pixel intensity values are integrated over the whole image size, which is 425x700 = 297,500 pixels. For further information on the image processing refer back to chapter 2.

In general, the sum of intensity per picture increases with increasing equivalence ratio. This is true until $\phi = 1.07$, with an exceptional data point for $\phi = 0.69$. For equivalence ratios $1.07 < \phi < 1.21$, the value is almost constant. After peaking at $\phi = 1.35$, the integrated intensity decreases and reaches a plateau ($1.53 < \phi < 1.71$). It is visible that the data can be grouped in three blocks. The first group are images where $0.5 \leq \phi \leq 0.88$. The second one ranges from $\phi = 0.93$ to $\phi = 1.26$. The third group are the remaining data points indicating images with $1.35 \leq \phi \leq 1.71$.
The groups correspond to the images that were taken with the same exposure time setting. Exposure time had to be changed for different equivalence ratios, since images would be saturated otherwise. During the data evaluation, values were normalized to an exposure of $1ms$. The discussed observation leads to the hypothesis, that the *ArtViewer* software does not set the exposure time accurately. [1]

[1] It was intended to verify this assumption by using a stabilized light source to test the exposure time behaviour of the software. Before working with the *ArtViewer* software, a different software has been used. It has been tested with a stabilized light source. The exposure time was increased linearly, and the integrated pixel value was measured. This test revealed a non-linear increase in the integrated pixel value, therefore the software has been exchanged for a the *ArtViewer* software. Due to the outbreak of the Coronavirus, the stabilized light source was not available for further testing and the cause for the stepwise increase in intensity remains unclear.

(a) Original image. (b) Inverted image.

Figure 4.4: Image of flame recorded with a CCD camera equipped with a UV filter. Equivalence ratio $\phi = 1.16$, outlet velocity of unburned gas mixture $v_{outlet} = 470$ cm/s and exposure time $t = 40ms$.

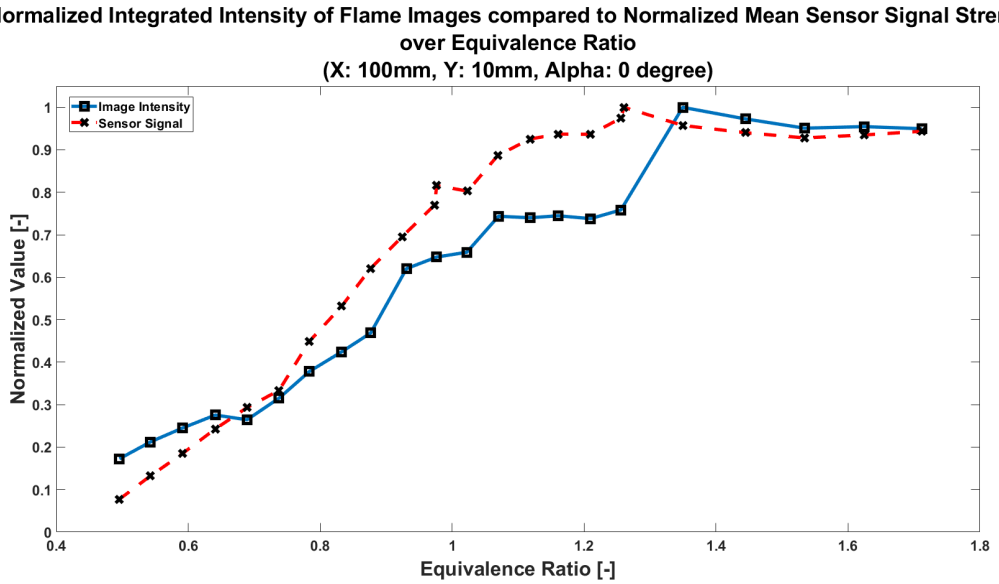

Figure 4.5: Normalized ϕ-signal curves of both experimental sensor data (S_{out} in mV, red dashed line) and chemiluminescence images data (intensity integrated over whole image, blue solid line) for equivalence ratios from $\phi = 0.5$ until $\phi \approx 1.7$. The images are taken from the same distance to the flame at which the sensor is placed, while the signal strength is measured (X = 100 mm, Y = 10 mm).

The flame images have been taken to provide a reference for the measured sensor signal strength. It is clear to see, that the curve fitted to these values does not follow a smooth line like for the sensor signal data. Nevertheless, both curves are compared after the data is normalized with respect to their maximum value, see figure 4.5. Note that the sensor signal was measured for two pairs of almost identical values for ϕ. The difference in signal strength between those values demonstrates measurement uncertainties.
The following observations are made. In general, both curves show an almost linear increase with equivalence ratio until $\phi \approx 1.07$. Subsequently, the curves flatten, but reveal a peak, before values decrease again and a plateau is reached. Interestingly, the peak for the measured sensor signal occurs for an equivalence ratio slightly lower than for the image intensity curve. However, the doubt remains that the peak for $\phi = 1.35$ might not be the global peak of the image curve, but enhanced by effects of a non-linear decrease of exposure time.

Further it can be noticed, that the image intensity reveals higher relative values for equivalence ratios $\phi < 0.67$, but increases less steep than the sensor signal curve and flattens more for equivalence ratios $1.07 \leq \phi \leq 1.26$. In contrast, the tail of the image curve decreases more than the tail of the sensor curve. This could stem from a non-linear decrease in exposure time. If the peak of the image curve was less high, the normalized curve would change.

To conclude this section, it can be said that the sensor detects the flame for all tested equivalence ratios. For $0.5 \leq \phi \leq 1.0$, the linear increase of the curve indicates, that the sensor can be used to identify the equivalence ratio of the flame for lean and stoichiometric flames. However, for rich flames with $\phi > 1.25$, it is difficult to identify a distinct signal strength for ϕ. The emission intensity values obtained from the chemiluminescence images support this analysis.

4.2. Sensor position and signal strength

To evaluate the influence of the sensor position on the signal strength, the three parameters that determine the positioning are varied. The horizontal distance at which the sensor is placed to the flame (referred to as variable X), the vertical distance above the nozzle rim (variable Y) and the angle α, from which the sensor points at the flame with reference to the horizontal plane. Flame parameters are $\phi = 0.5$, $v_{outlet} = 740 cm/s$ and therefore $Re \approx 800$ (for more details refer back to section 3.1). The following section presents and discusses the signal curves.

To interpret the signal curves, the influence of the sensor's FoV is taken into account. The FoV defines the area that is seen by the sensor. As figure 2.10 in chapter 2 shows, the light from different parts of the FoV contributes differently to the sensor signal. It is visible that the FoV is $\pm 15°$ wide. Figure 4.6 illustrates the Field of View of the *TOCON ABC1* projected on the flame. To interpret the signal curves, the projection of the sensor's FoV is plotted for each measurement. The projection displays the whole FoV, the centre is marked with a red rectangle. Looking at figure 2.10, the area around the centre contributes significantly more than the outer edges of the FoV.
The flame height is determined based on a picture of the flame that was taken during the measurement with a ruler placed next to it, like in figure 4.7a. It has to be pointed out that only visible emissions are displayed on the image, not UV light. Therefore, the deducted flame height might deviate from the flame height that is relevant for the sensor. The visible blue irradiation is emitted either from the $H_2O_2^*$ radical, or from the H_2O^* radical (see reference [16]). As stated in [16], the blue emission originates from the same region as the OH^* emission. Hence it is claimed that the photo in figure 4.7a can be an approximation of the flame area where the UV light stems from.

To explain the data with respect to the non-uniform transmission characteristic of the sensor's FoV shown in figure 2.10, it is necessary to take a look at the relative emission intensities over the flame height. Figure 4.8 shows the Abel inverted data of the chemiluminescence image for a flame with $\phi = 0.5$, which itself is shown in figure 4.7b (with inverted colours). It is visible that higher emission values come from the region close to the flame base, whereas they decrease towards the flame tip. The open tip, a phenomenon typical for lean hydrogen-air flames, is nicely visible in all flame images (figures 4.7 and 4.8). Due to the high mobility of hydrogen, it diffuses radially outwards, hence the concentration of hydrogen at the flame tip is lower than the oxygen concentration. This results in a locally reduced equivalence ratio towards the tip. If the fuel-air ratio (equivalence ratio) at the tip is not enough to sustain reactions, flame extinction occurs and the tip appears as open. Reference [25] provides a good explanation of the theoretical background of this phenomenon. Reference [5] maps for which conditions tip opening occurs. The observations of blow out and tip opening made in this work are in good agreement with their findings. Tip opening occurred for flames with equivalent ratios up until $\phi \leq 1.02$, after which the flame tip is closed, as visible in the example image in figure 4.4. Chemiluminescence images for $0.5 \leq \phi \leq 1.71$ are shown in appendix B.
Since the spatial distribution of chemiluminescence intensity at $\phi = 0.5$ shows that the main contribution to the overall emission stems from the flame base, the tip opening is not considered to be influential on the results discussed hereunder.

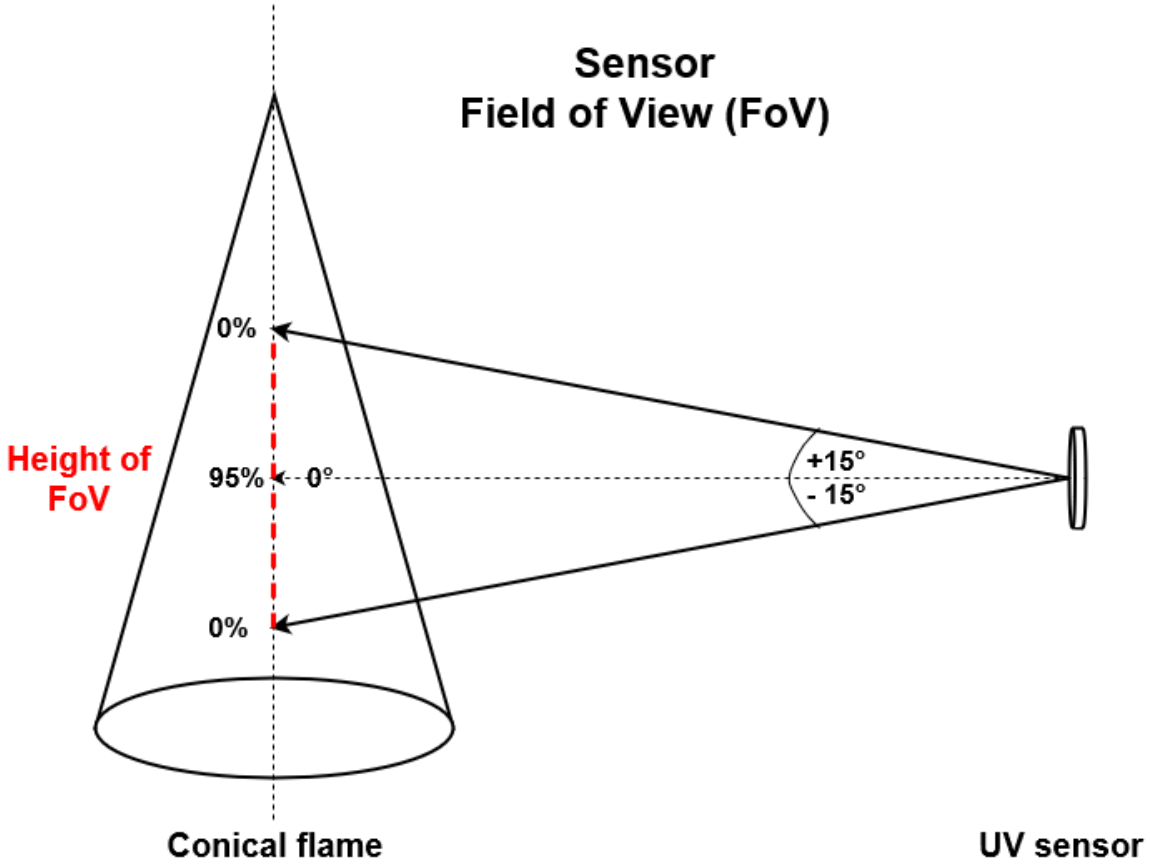

Figure 4.6: Illustration of the FoV of the *TOCON ABC1*. Light beams from different parts of the flame contribute differently to the sensor signal. The FoV is $\pm 15^{\circ}$ wide.

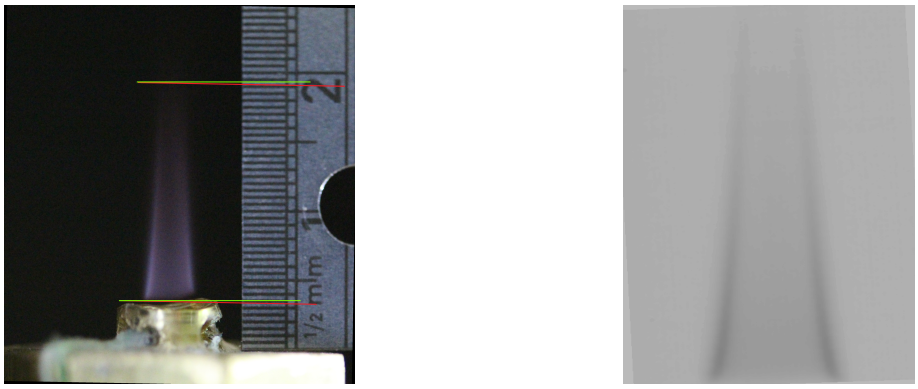

(a) Photo of flame with ruler next to it for approximation of dimensions.

(b) Inverted chemiluminescence image from CCD camera equipped with UV filter. Exposure time $t = 80ms$.

Figure 4.7: Image of visible emission (a) and of UV emission (b) for flame with equivalence ratio $\phi = 0.5$ and outlet velocity of unburned gas mixture $v_{\text{outlet}} = 470$ cm/s.

Horizontal distance X

Figure 4.9 shows the measured sensor signal for increasing horizontal distance between sensor and flame, compared to a curve that displays the *inverse square law*. Figure 4.10 illustrates how the FoV projection on the flame changes with increasing horizontal distance between sensor and flame.

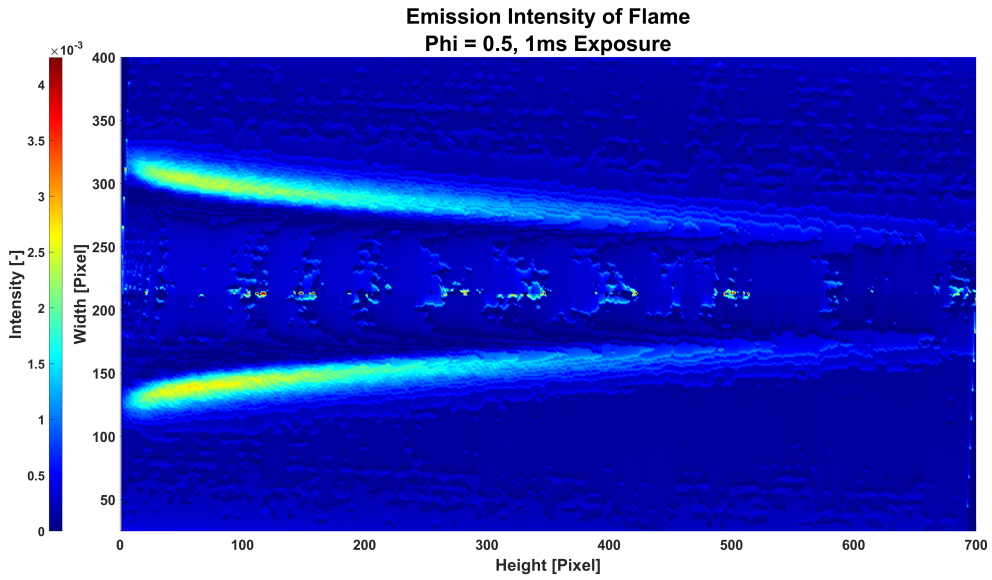

Figure 4.8: Intensity values for Abel inverted image of a flame recorded with a CCD camera equipped with a UV filter. Equivalence ratio $\phi = 0.5$, outlet velocity of unburned gas mixture $v_{\text{outlet}} = 470$ cm/s.

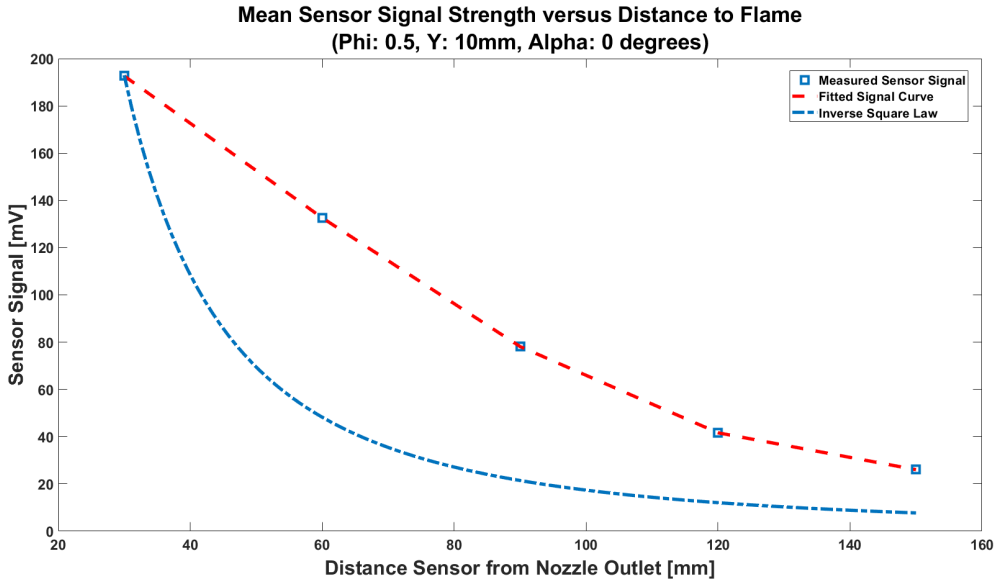

Figure 4.9: Measured sensor signal S_{out} for increasing horizontal distance between sensor and flame and inverse square law. Steady decrease of signal strength with increasing distance X.

The curve in figure 4.9 decreases steadily for increasing values of X. However, figure 4.10 shows that for $X = 30mm$, the flame base, where emission intensities are highest (see figure 4.8), is not yet covered by the view field. For $X = 60mm$, the flame base does contribute.
This is not visible in the signal curve. The dependence of light intensity to distance has to be taken into account. According to the *inverse square law* in eq. (4.1), the decay of intensity of light is inversely proportional to the distance squared to the source of light emission.

$$\text{intensity} \propto \frac{1}{X^2} \tag{4.1}$$

Although the decay of the curve does not reveal this proportionality, the increasing distance seems to have more influence on the signal strength than the sensor's FoV.

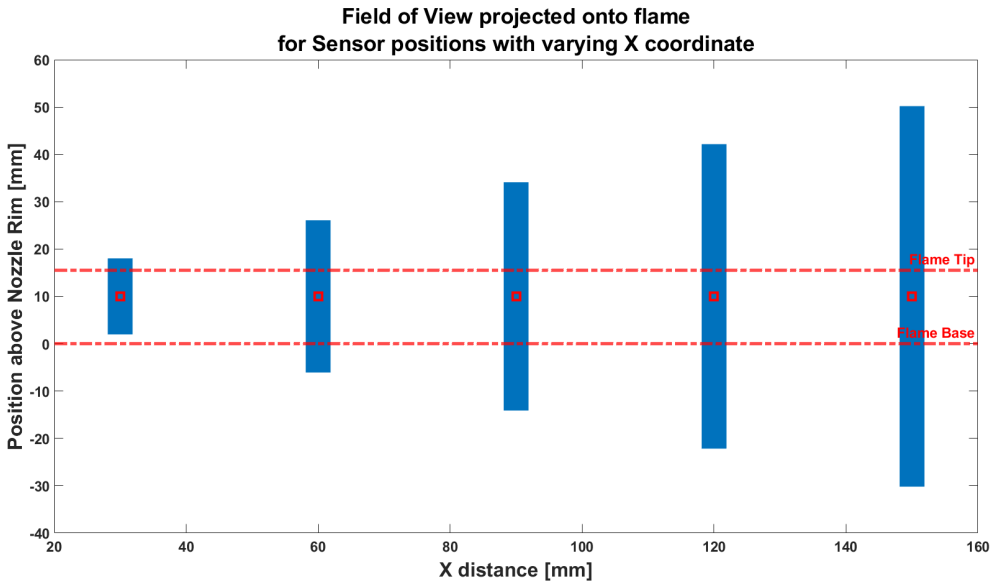

Figure 4.10: FoV projection onto the flame for increasing horizontal distance between sensor and flame while $Y = 10mm$.

Even at a horizontal distance of $X = 150mm$, the signal strength is above the offset voltage of $S_{\text{out,dark}} = 0.7mV$. Hence, a flame is detectable for the whole range of distances. The curve reveals a clear correlation of horizontal distance and signal strength.

Vertical distance Y

Figure 4.11 shows the measured sensor signal mean for increasing vertical distance between sensor and flame, hence sensor height above the nozzle rim. Figure 4.12 illustrates how the FoV projection on the flame changes with increasing sensor height.

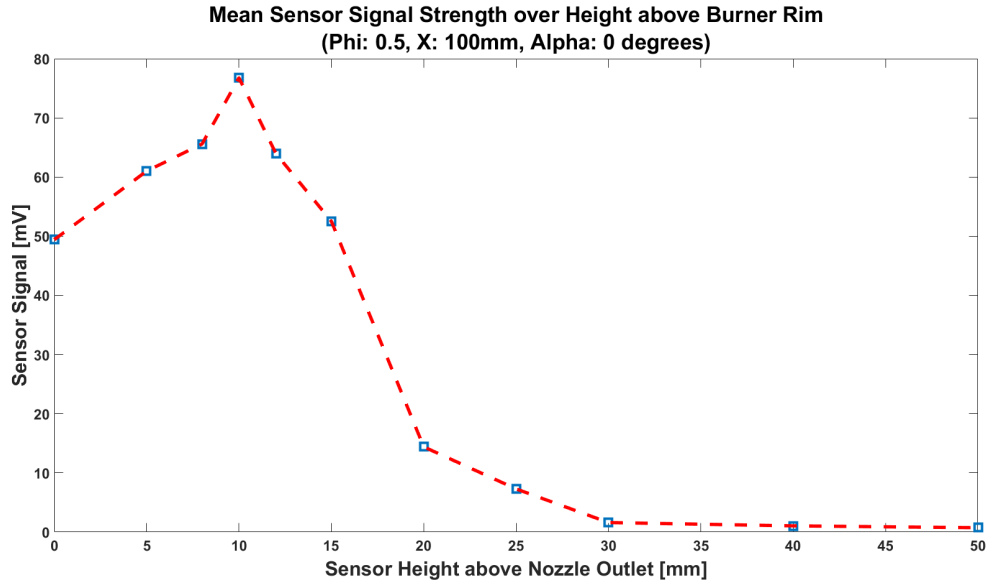

Figure 4.11: Measured sensor signal S_{out} for increasing vertical distance between sensor and flame. Horizontal error bars indicate uncertainty of the sensor position, vertical bars show the standard fluctuation of the measured sensor signal. Increase of signal strength for $0mm \leq Y \leq 10mm$, subsequent decrease of S_{out} for $Y > 10mm$.

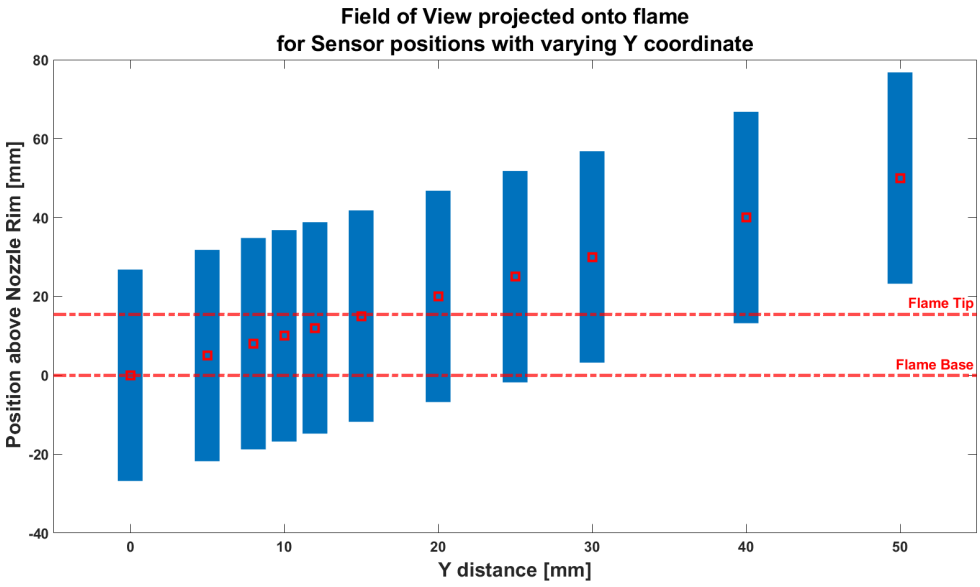

Figure 4.12: FoV projection onto the flame for increasing vertical distance between sensor and flame while $X = 100mm$.

The curve in figure 4.11 increases for $0mm \leq Y \leq 10mm$. Signal strength for $Y = 8mm$ and $Y = 12mm$ is comparable, the same is true for $Y = 0mm$ and $Y = 15mm$. For $15mm \leq Y \leq 20mm$ the curve decays fast, steeper than for $20mm \leq Y \leq 30mm$. For $Y \geq 30mm$ almost no signal strength measurable.

From figure 4.12 it can be seen that the visible flame area moves towards the tip with increasing value Y. For $Y = 5mm$, the centre of the FoV falls on the flame base. Half of the area around the centre does not include the flame. For distances $Y = 5mm$ to $Y = 15mm$, the centre of the FoV lies within the flame. For $Y > 30mm$, only the weekly contributing edge of the FoV covers the flame. For $Y > 40mm$ the flame is completely out of sight.
When comparing both figures, two remarks have to be discussed. First, that the peak for $Y = 10mm$ seems unreasonably high when compared to the trend of the curve. Secondly, that looking at figure 4.12, the peak is expected to occur for a lower sensor height, i.e. at $Y \approx 8mm$. The centre of the FoV moves towards the flame tip for increasing values of Y. From $Y = 0mm$ to $Y = 8mm$, the central area of the FoV covers an increasing part of the flame base, where emissions are higher than at the rest of the flame. For $Y > 8mm$, the central area of the FoV moves up, towards the flame tip. Hence, it is expected that $S_{out,Y10} < S_{out,Y8}$.
Looking at the conditions of the measurements, it is found that the nozzle temperature for $Y = 10mm$ was higher than for the rest of the experiment, with $T_{10} = 29.27°C$, while $T_5 = 27.35°C$, $T_8 = 26.48°C$ and $T_{12} = 26.86° C$. This increase in temperature is comparably small. Nevertheless, $S_{out,10mm}$ is higher than other measurements for the same sensor configuration. The configuration $X = 100mm$, $Y = 10mm$ and $\alpha = 0°$ occurs three times. The two other data points are part of the measurements for tilt angle α (presented below). If those three data points are compared, it is

$$S_{out,10mm} = 76.8mV \text{ and } T_{10} = 29.27°C$$
$$S_{out,0°,neg} = 55.6mV \text{ and } T_{0°,neg} = 25.25°C$$
$$S_{out,0°,pos} = 68.5mV \text{ and } T_{0°,pos} = 28.44°C$$

Hence, $S_{out,10mm} > S_{out,0°,pos} > S_{out,0°,neg}$ and $T_{10} > T_{0°,pos} > T_{0°,neg}$ are coherent.

Only at vertical distances $Y > 50mm$, the sensor signal is lower than the offset voltage $S_{\text{out,dark}} = 0.7mV$ ($S_{out,50} = 0.74mV$). However, it is recommended to install the sensor at $Y < 20mm$, since the signal looses strength and becomes weak for increased heights. Compared to the horizontal distance, an increase in vertical distance leads to higher signal losses.

Tilt angle α

When comparing figures 4.13 and 4.15, it is visible that $S_{out,0°,pos} \neq S_{out,0°,neg}$ (observation is discussed above). Due to this deviation, the measurements for $\alpha < 0$ and $\alpha > 0$ are presented separately.

Inclination towards flame base

Figure 4.13 shows the measured sensor signal mean for different negative tilt angle values. As indicated in figure 2.11 in chapter 2, a negative tilt angle describes a tilt towards the flame base. Figure 4.14 illustrates how the FoV projection on the flame changes for an inclined sensor.

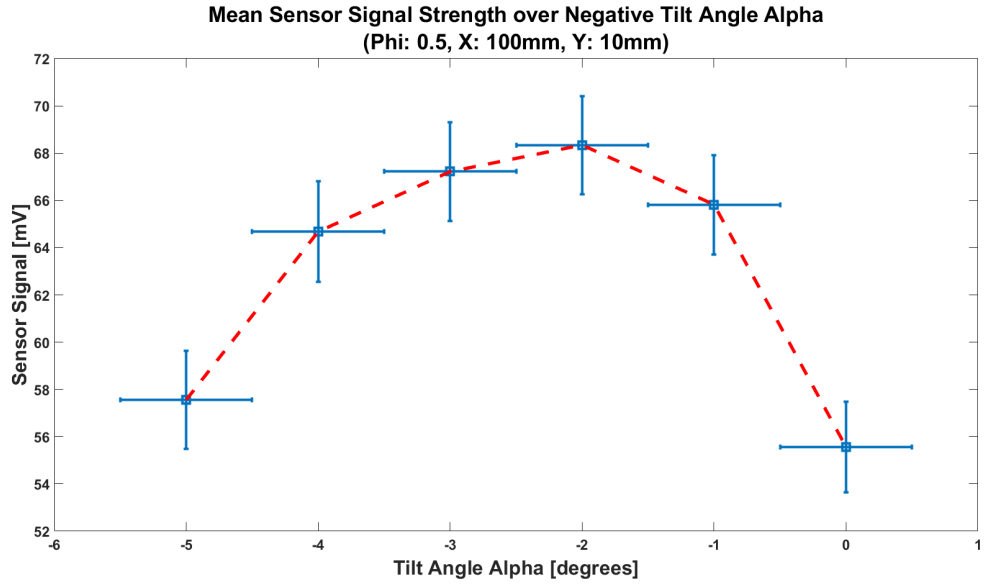

Figure 4.13: Measured sensor signal S_{out} for increasing inclination of the sensor towards the flame base. Horizontal error bars indicate uncertainty of the sensor position, vertical bars show the standard fluctuation of the measured sensor signal. Increase of signal strength for $0° \leq \alpha \leq -2°$, subsequent decrease of S_{out} for $\alpha < -2°$.

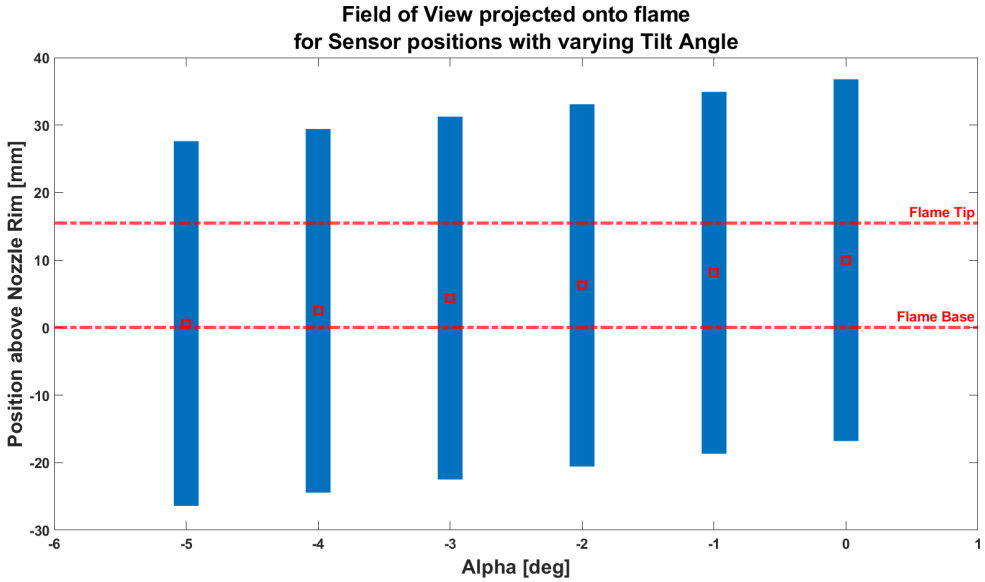

Figure 4.14: FoV projection onto the flame for increasing inclination of the sensor towards the flame base while $X = 100mm$ and $Y = 10mm$.

The sensor signal curve in figure 4.13 shows an increase in signal strength for $-2° \leq \alpha \leq 0°$. If the sensor is tilted further, the signal strength decreases again, with $S_{out,-5°} > S_{out,0°}$. The differences in signal strength for $-1° \leq \alpha \leq -4°$ is only $64.7mV \leq S_{out} \leq 68.3mV$. If standard deviations are taken into account, this difference can be even smaller.
The discussed observations are compared to what is described in figure 4.14.
For $\alpha = 0°$, the centre of the FoV lies in the upper half of the flame. When the sensor is tilted towards the flame base, the centre of the FoV moves towards the flame base, where emissions are higher. This results in an increased signal strength. However, for $\alpha < -2°$, the FoV centre covers always less of the flame. For $\alpha = -5°$, the centre of the FoV lies almost outside of the flame area. This leads to a decrease in sensor signal.

For all values of α, the flame is detected. However, it is recommended to maintain the tilt angle within $\alpha \geq -4°$, since signal losses are lower than for $\alpha = 0°$ or $\alpha = -5°$ for this sensor position.

Inclination towards flame tip

Figure 4.15 shows the mean measured sensor signal for different positive tilt angle values. As indicated in figure 2.11 in chapter 2, a positive tilt angle describes a tilt towards the flame tip. Figure 4.14 illustrates how the FoV projection on the flame changes for an inclined sensor.

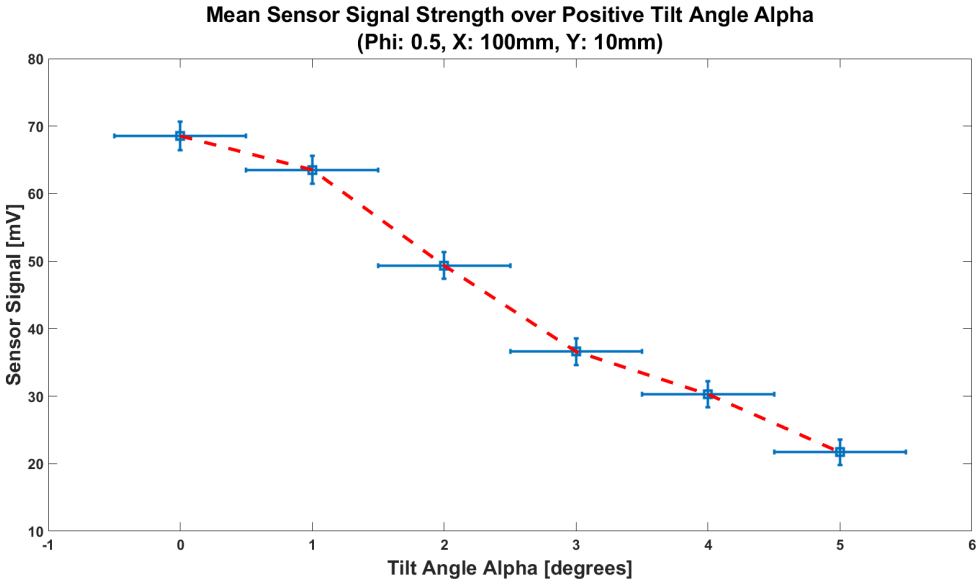

Figure 4.15: Measured sensor signal S_{out} for increasing inclination of the sensor towards the flame tip. Horizontal error bars indicate uncertainty of the sensor position, vertical bars show the standard fluctuation of the measured sensor signal. Steady decrease of signal strength for increasing tilt angles.

Figure 4.15 shows, that sensor signal strength decreases steadily with increasing inclination towards the flame tip. The loss of signal strength is faster for angles $1° < \alpha \leq 3°$ than for $3° < \alpha \leq 5°$.
Looking at figure 4.16 it is visible that the centre of the FoV moves further away from the flame base, for increasing values of α. For $\alpha > +3°$, the centre of the FoV lies above the flame tip.

For all values of α, the flame is detected. However, tilting the sensor towards the tip is not recommended, since it results in signal losses.
Comparing negative and positive values for the tilt angle, it is recommended to install the sensor in a position where it is directed to the flame base, such as $\alpha = -2°$ for $X = 100mm$ and $Y = 10mm$.

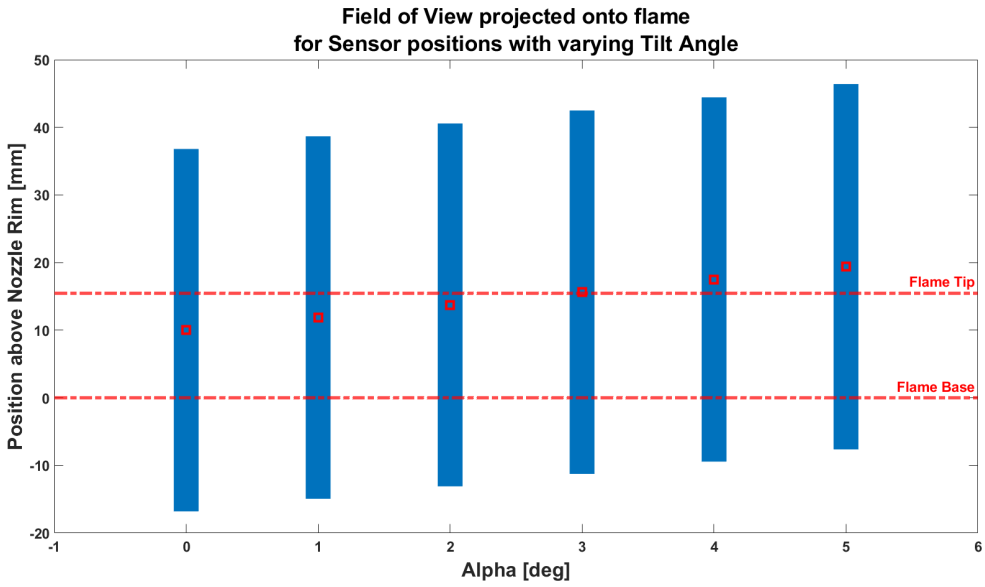

Figure 4.16: FoV projection onto the flame for increasing inclination of the sensor towards the flame tip while $X = 100mm$ and $Y = 10mm$.

Conclusion

To conclude this chapter, the following findings are summarized.

1. The sensor detects the flame for all tested equivalence ratios. For $0.5 \leq \phi \leq 1.0$, the linear increase of the curve indicates, that the sensor can be used to identify the equivalence ratio of the flame for lean and stoichiometric flames for a stepwise increase of $\Delta\phi = 0.05$. However, for rich flames with $\phi > 1.25$, it is difficult to identify a distinct signal strength for a distinct value of ϕ. The emission intensity values obtained from the chemiluminescence images support this analysis.

2. The sensor position has a clear influence on the measured sensor signal strength. Only in a few cases the examined sensor position reveals that the flame can not be detected. This concerns the positioning of the sensor at heights greater than $Y > 50mm$, for a horizontal distance of $X = 100mm$ and a neutral sensor position where $\alpha = 0°$.

3. Although the sensor detects the flame for almost all tested positions, some recommendations are made to avoid strong signal losses. The horizontal distance affects the sensor signal strength less, than the vertical distance. It is recommended to install the sensor at heights $Y < 20mm$. Regarding the tilt angle of the sensor, it is recommended to install the sensor in a position where it is directed to the flame base, such as $\alpha = -2°$ for $X = 100mm$ and $Y = 10mm$.

4. It has been observed that the temperature of the nozzle rim affects the sensor signal strength. This does not hinder the sensor from detecting the flame. However, for a reliable interpretation of the sensor signal, it is recommended to investigate the quantitative influence of the nozzle temperature, or to implement a cooling of the burner head to ensure stable conditions during the measurements.

5

The View Factor - Analytical description of the sensor position

Introduction

The following chapter describes how the influence of the sensor position on the sensor signal is intended to be described analytically. The sensor position is determined by three parameters: The horizontal distance between the sensor and the flame, expressed as the X coordinate, the vertical distance, defined as Y coordinate and the angle under which the sensor is directed to the flame, tilt angle α. The sensor position relative to the flame determines how much emission is incident on the sensor surface, therefore the sensor signal is directly influenced by the positioning of the sensor. If an equation is developed that describes the influence accurately, it can support in the design process of the appliance that is using UV sensor technology. If the possible sensor position is known, it can give a first evaluation of the feasibility of the position. Once a position is chosen, the equation can be used to quantify the influence of the position on the measured signal, to ensure a correct translation from measured sensor signal to flame emission and equivalence ratio.

In *Radiative Heat Transfer* theory, the View Factor (VF) (also referred to as *configuration factor* or *shape factor*) describes how much radiation emitted by one surface or object is transmitted to a second surface or object as a function of their position relative to each other. The present study evaluates whether this concept can be extended to the fraction of UV light emitted by the flame and sensed by the sensor.
The authors of reference [24] derived and successfully applied a View Factor for the radiation emitted from UV light source. Unlike a light source, the emission intensity distribution of a flame is not homogeneous, as shown in figure 4.8 in chapter 4. Since the VF assumes assumes homogeneous properties of the emitting and receiving surface, it is expected that the VF does not predict the emission of the flame accurately. Since the flame consists of adjacent point sources that emit isotropically in all directions, and the flame is assumed to be optically thin, the flame emission that reaches the sensor stems not only from the frontside of the flame, but also from the inside of the backside of the flame. A novel idea how to account for this is to derive two View Factors, one for the frontside and one for the inside of the backside of the flame, and to use the sum of both. Figure 5.1 illustrates the case for which the View Factors are derived. The frontside (and backside) is defined by the portion of the flame that is visible to the sensor. It is a function of the position of the sensor and described by the angle ω.
For the correct implementation of the formulas it is important to mention that the View Factor theory assumes a free way from flame to sensor, without objects that would block the light.

5.1. Theory of concept

The following section describes the View Factor concept according to chapter 4 of Michael F. Modest's book *Radiative Heat Transfer* (reference [27]). Equations (5.1) to (5.9) are taken from this source.
The radiation transport rate is defined as the energy leaving the first surface incident on the second surface divided by the energy leaving the first surface. For two infinitesimal surface elements dA_i and dA_j this means

$$dF_{dA_i-dA_j} = \frac{\text{energy leaving } dA_i \text{ directed towards } dA_j \text{ and incident on } dA_j}{\text{total energy leaving } dA_i} \tag{5.1}$$

The heat transfer rate from dA_i to dA_j is

$$\frac{I(r_i)\cdot\cos\Theta_i\cdot\cos\Theta_j}{S^2}dA_i dA_j \tag{5.2}$$

with $I(r)$ defined as radial radiation, Θ describing the angle between the surface normal $\vec{n}$ and the line connecting both surfaces s_{ij}, with length S. The total energy leaving dA_i is

$$I(r_i)\cdot\pi dA_i \tag{5.3}$$

Hence,

$$dF_{dA_i-dA_j} = \frac{\cos\Theta_i\cdot\cos\Theta_j}{S^2\cdot\pi}dA_j \tag{5.4}$$

If vectors r_i and r_j point from the origin of the chosen coordinate system to A_i and A_j respectively, then their connecting vector is described as $s_{ij} = r_j - r_i$. Since $\cos\Theta_i = \hat{n}_i \cdot s_{ij}/|s_{ij}|$, the VF can be formulated in vector form as

$$dF_{dA_i-dA_j} = \frac{(\hat{n}_i\cdot s_{ij})(\hat{n}_j\cdot s_{ji})}{\pi\cdot S^4}dA_j \tag{5.5}$$

The vector form of the VF allows to express the integrant of equation (5.4) in terms of the local coordinate system in which both surfaces are described.

For the present situation, the flame emission is considered as the surface radiation from a cone, and the sensor is represented by the surface of an area. The VF from a differential element dA_i to a finite area A_j is derived as

$$dF_{dA_i-A_j} = \int_{A_j}\frac{\cos\Theta_i\cdot\cos\Theta_j}{\pi\cdot S^2}dA_j \tag{5.6}$$

One method to solve a surface integral like in equation (5.6) is to transform it into a contour integral. Stokes' theorem describes that a surface integral can be converted into a contour integral by

$$\oint_b f\cdot ds = \int_A(\nabla\times f)\cdot\hat{n}dA \tag{5.7}$$

where b is the boundary of the contour, f a vector function defined for the whole surface A, ds the vector describing the contour of the surface and $\hat{n}$ the vector normal to the surface.
For the present application, the VF in equation (5.6) can be transformed into

$$F_{d1-2} = \frac{1}{2\cdot\pi}\oint_{b_2}\frac{(s_{12}\times\hat{n}_1)ds_2}{S^2} \tag{5.8}$$

with s_{12} as vector pointing from dA_1 to a point on the contour of A_2 and ds_2 pointing along the contour of A_2. For the derivation of eq. 5.8 see page 139f in [27].
Finally, the VF expressed in a Cartesian coordinate system becomes

$$\begin{aligned} F_{d1-2} = &\frac{l_1}{2\cdot\pi}\cdot\oint_{b_2}\frac{(z_2-z_1)dy_2-(y_2-y_1)dz_2}{S^2} \\ &+\frac{m_1}{2\cdot\pi}\cdot\oint_{b_2}\frac{(x_2-x_1)dz_2-(z_2-z_1)dx_2}{S^2} \\ &+\frac{n_1}{2\cdot\pi}\cdot\oint_{b_2}\frac{(y_2-y_1)dx_2-(x_2-x_1)dy_2}{S^2} \end{aligned} \tag{5.9}$$

with l_1, m_1 and n_1 indicating the direction cosines for normal vector $\hat{n}$, S^2 as the length of s_{ij} and

$$s_{12} = (x_2 - x_1)\,\hat{i} + (y_2 - y_1)\,\hat{j} + (z_2 - z_1)\,\hat{k}$$

5.2. Application to present work

Figure 5.1 illustrates the geometry for which the View Factor is obtained.

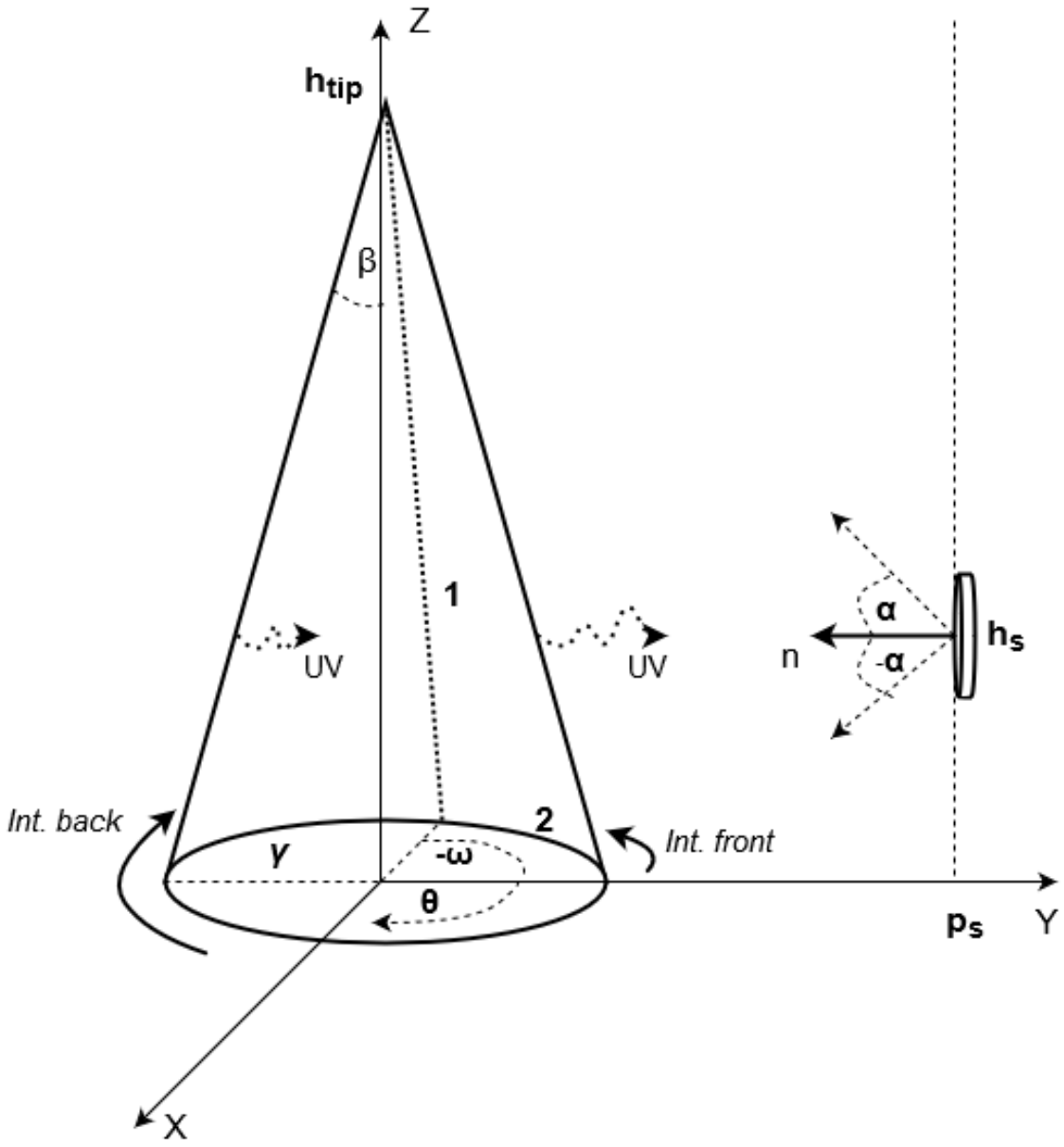

Figure 5.1: Illustration of case for which VF equation is derived, where the flame is approximated by a cone that points in the positive direction of the Z axis of the chosen coordinate system. The flame height is indicated by h_{tip}. In the same coordinate system, the sensor is positioned at the side of the cone, at a position given by $X = 0$, $Y = p_s$ and $Z = h_s$. The inclination of the sensor is described with angle α, that is defined as $\alpha < 0$ for tilting towards the flame base and $\alpha > 0$ for tilting towards the flame tip. The portion of the flame visible by the sensor is defined through angle ω. ω is a property of the relative position of flame and sensor. The angle θ defines the position along the circular base of the cone. Line 1 and arc 2 are the boundaries that describe half of the visible cone. The dotted arrows indicate UV radiation from the backside and the frontside of the flame towards the sensor.

The centre of the cone base is the origin of the coordinate system. The tip of the cone is pointing into the positive direction of the Z axis. The sensor is positioned at the side of the cone. The sensor normal $\vec{n}$ is perpendicular to the Z axis. The two boundaries for which the contour integral is solved are the dotted line 1 and the partial circumference of the cone base, labelled with 2.

A View Factor is a property of two surfaces, one that emits radiation and one that receives radiation. Equation (5.6) describes the VF from a sending surface that is small and a receiving surface that is large. Working with eq. (5.6) and resulting eq. (5.9), therefore gives the view factor from sensor to cone. However, for the case of this study, the View Factor from cone to sensor is needed. The *law of reciprocity* states that

$$A_i \cdot F_{A_i - A_j} = A_j \cdot F_{A_j - A_i} \tag{5.10}$$

If the area of the flame and the sensor area are known, the desired View Factor functions can be obtained. This calculation is carried out after the VF equation is derived.
For the given application not only the emission originating from the visible area of the cone reaches the sensor, but also the light that stems from the backside of the back half of the cone, as indicated by the dotted arrows in figure 5.1. As described in the introduction, two View Factor equations are derived, one for the cone frontside, called View Factor frontside (VFF) and one for the cone backside, called View Factor backside (VFB). Because of the geometry of a cone, the contours, or boundaries for which the integral in equation (5.9) are solved are the same for both cone halves. The integration limits change, and so does the direction of the integration (see figure 5.1). After the contour integrals for both boundaries are presented, this issue will be explained in more detail.

For the context illustrated in figure 5.1, the direction cosines for the sensor element are

$$\begin{aligned} l_1 &= 0 \\ m_1 &= -\cos(\alpha) \\ n_1 &= \sin(\alpha) \end{aligned} \tag{5.11}$$

The radius γ is the radius of the circular horizontal cross section of the cone at height h_z

$$\gamma = (h_{\text{tip}} - h_z) \cdot \tan(\beta) \tag{5.12}$$

where $h_z \in [0, h_{\text{tip}}]$. The coordinates of the sensor element are

$$\begin{aligned} x_1 &= 0 \\ y_1 &= p_s \\ z_1 &= h_s \end{aligned} \tag{5.13}$$

The portion of the cone that is visible for the sensor is defined by the angle ω. It changes according to

$$\omega = \arccos\left[\frac{h_{\text{tip}} - h_s}{p_s} \cdot \tan(\beta)\right] \tag{5.14}$$

If the sensor is positioned at the side of the cone, ω is slightly lower than $\pi/2$. If the sensor is positioned above the flame tip, ω is slightly higher than $\pi/2$. In the following, the coordinates of boundary 1 and distance S^2 between the boundary and the sensor are derived. The coordinates are

$$\begin{aligned} x_2 &= \gamma \cdot \sin(\omega) \\ y_2 &= \gamma \cdot \cos(\omega) \\ z_2 &= h_{\text{tip}} - \gamma \cdot \cot(\beta) \end{aligned} \tag{5.15}$$

Since the integration of boundary 1 is done over the radius of the cone base γ, dx, dy and dz are converted into

$$\begin{aligned} dx_2 &= \sin(\omega) d\gamma \\ dy_2 &= \cos(\omega) d\gamma \\ dz_2 &= -\cot(\beta) d\gamma \end{aligned} \tag{5.16}$$

The distance S^2 is calculated to be

$$S^2 = \gamma^2 - 2\gamma \cdot p_s \cdot \cos(\omega) + {p_s}^2 + (h_{\text{tip}} - \gamma \cdot \cot(\beta) - h_s)^2 \tag{5.17}$$

Equations (5.11) to (5.17) are substituted in equation (5.9). The integral that is solved for boundary 1 is then

$$f_{B1} = \int_0^r -\frac{\left(\cos(\alpha)\left(h_s - h_{\text{tip}}\right) + \sin(\alpha)\, p_s\right)\sqrt{1 - \frac{\tan^2(\beta)\left(h_{\text{tip}} - h_s\right)^2}{{p_s}^2}}}{2\pi\left(\cot^2(\beta)\gamma^2 + \gamma^2 - 2\tan(\beta)\left(h_{\text{tip}} - h_s\right)\gamma + 2\cot(\beta)\left(h_s - h_{\text{tip}}\right)\gamma + t^2 - 2h_s h_{\text{tip}} + {h_s}^2 + {p_s}^2\right)} d\gamma \tag{5.18}$$

The integration is carried out with Wolfram's *Wolfram Mathematica* software. Integration limits are $\gamma_{lower} = 0$ and $\gamma_{upper} = r$ both for VFF and VFB, with r being the radius of the cone base.

For boundary 2, the partial arc of the cone base, the coordinates are the following.

$$\begin{aligned} x_2 &= r \cdot \sin(\theta) \\ y_2 &= r \cdot \cos(\theta) \\ z_2 &= 0 \end{aligned} \tag{5.19}$$

Since boundary 2 is integrated over the angle θ in the plane of the cone base, dx, dy and dz are expressed as

$$\begin{aligned} dx_2 &= r \cdot \cos(\alpha)\, d\theta \\ dy_2 &= -r \cdot \sin(\alpha)\, d\theta \\ dz_2 &= 0 \end{aligned} \tag{5.20}$$

Distance S^2 is now

$$S^2 = r^2 - 2 \cdot r \cdot p_s \cdot \cos(\theta) + {p_s}^2 + {h_s}^2 \tag{5.21}$$

Again, equations (5.11), (5.13) and (5.15) to (5.21) are substituted in equation (5.9) and the integral to solve for boundary 2 is

$$f_{B2} = \int_{\theta_{lower}}^{\theta_{upper}} \frac{r\left(\sin(\alpha)\left(r - p_s\cos(\theta)\right) - \cos(\alpha)\, h_s \cos(\theta)\right)}{2\pi\left(-2p_s r\cos(\theta) + {h_s}^2 + r^2 + {p_s}^2\right)} d\theta \tag{5.22}$$

Unlike for boundary 1, the integration limits for the frontside VF are not the same as for the backside VF. For the frontside, integration limits are $\theta_{lower} = 0$ and $\theta_{upper} = -\omega$. As this describes only half of the geometry, the term is multiplied by two for the calculation of the View Factor equation.
For the backside, the integration limits are $\theta_{lower} = \omega$ and $\theta_{upper} = -\omega$. Here, the integration is done in the clockwise direction, unlike before. This is done because the light emission towards the inside of the cone surface is needed, therefore the surface normal has to be pointing inwards (as indicated in figure 5.1). Changing the direction of integration leads to the desired result.
If integrated f_{B1} is defined as F_{B1} and integrated f_{B2} as $F_{\text{B2,front}}$ and $F_{\text{B2,back}}$, the View Factor for frontside and backside are calculated as

$$\begin{aligned} \text{VFF} &= 2 \cdot (F_{B1} + F_{\text{B2,front}}) \\ \text{VFB} &= 2 \cdot (F_{B1} + F_{\text{B2,back}}) \end{aligned} \tag{5.23}$$

It results that $\text{VFF} = \text{VFB} = 0.5 \cdot \text{VF}_{\text{complete}}$. The equation obtained from *Mathematica* is

$$\begin{aligned} \text{VF} = &-\pi\Bigg(\frac{4\sin^2(\beta)(\cos(\alpha)(h_s - h_{\text{tip}}) + p_s\sin(\alpha))\sin(\omega)}{A} \\ &\cdot \frac{\left(\arctan\left(\frac{2\sin(\beta)\left(p_s\sin(\beta)\cos(\omega) + \cos(\beta)(h_{\text{tip}} - h_s)\right)}{A}\right) + \arctan\left(\frac{p_s\cos(2\beta - \omega) - 2p_s\cos(\omega) + p_s\cos(\omega + 2\beta) + 2h_s\sin(2\beta) - 2h_{\text{tip}}\sin(2\beta) + 4r}{2A}\right)\right)}{A}\Bigg) \\ &+ \pi\frac{2\left(p_s\sin(\alpha)\left({h_s}^2 + {p_s}^2 - r^2\right) + h_s\cos(\alpha)\left({h_s}^2 + {p_s}^2 + r^2\right)\right){p_s}^2\left(\frac{\left({h_s}^2 + (p_s + r)^2\right)\tan\left(\frac{1}{2}\omega\right)}{\sqrt{2{h_s}^2\left({p_s}^2 + r^2\right) + h_s^4 + \left({p_s}^2 - r^2\right)^2}}\right)}{p_s\sqrt{2{h_s}^2\left({p_s}^2 + r^2\right) + h_s^4 + \left({p_s}^2 - r^2\right)^2}} \\ &- \pi\frac{(h_s\cos(\alpha) + p_s\sin(\alpha))\omega}{p_s} \end{aligned} \tag{5.24}$$

where

$$A := |\sin(\beta)| \sqrt{\cos(2\beta)\left({p_s}^2 \cos\left(2\arccos\left(\frac{\tan(\beta)(h_{\text{tip}}-h_s)}{p_s}\right)\right) - 2{h_s}^2 + 4h_s h_{\text{tip}} - 2h_{\text{tip}}^2 + {p_s}^2\right)}$$

$$+ |\sin(\beta)| \sqrt{-{p_s}^2 \cos\left(2\arccos\left(\frac{\tan(\beta)(h_{\text{tip}}-h_s)}{p_s}\right)\right) + 4h_s p_s \sin(2\beta)\cos\left(\arccos\left(\frac{\tan\beta(h_{\text{tip}}-h_s)}{p_s}\right)\right)} \tag{5.25}$$

$$+ |\sin(\beta)| \sqrt{-4h_{\text{tip}} p_s \sin(2\beta)\cos\left(\arccos\left(\frac{\tan\beta(h_{\text{tip}}-h_s)}{p_s}\right)\right) + 2{h_s}^2 - 4h_s h_{\text{tip}} + 2h_{\text{tip}}^2 + 3{p_s}^2}$$

It has to be mentioned that this equation is valid only if the plane of the sensor does not intersect the cone. This limitation can be described with the tilt angles $\alpha_{\text{pos,max}}$ and $\alpha_{\text{neg,max}}$.

$$\begin{aligned} \alpha_{\text{pos,max}} &= \arctan(\frac{p_s - s}{h_s}) \\ \alpha_{\text{neg,max}} &= \arctan(\frac{p_s}{h_{\text{tip}} - h_s}) \end{aligned} \tag{5.26}$$

As mentioned above, the formula in eq. (5.24) describes the View Factor from the sensor to the flame, so

$$\text{VF} := \text{VF}_{S-F}$$

To calculate the View Factor from flame to sensor (VF_{F-S}), equation (5.10) is used. The sensor area A_S is constant. Since the sensor receives emission from the frontside of the flame and from the inside of the backside of the flame, the flame area is divided in A_f and A_b, where indices f and b mean frontside and backside, respectively.
After applying eq. (5.10), the following relations are obtained

$$\begin{aligned} \text{VFF}_{F-S} &= \frac{A_S}{A_f} \cdot \text{VFF}_{S-F} \text{ and} \\ \\ \text{VFB}_{F-S} &= \frac{A_S}{A_b} \cdot \text{VFB}_{S-F} \end{aligned} \tag{5.27}$$

The VF from the whole flame to the sensor is

$$\text{VF}_{F-S} = \text{VFF}_{F-S} + \text{VFB}_{F-S} \tag{5.28}$$

Since $\text{VFF}_{S-F} = \text{VFB}_{S-F} = 0.5 \cdot \text{VF}_{S-F}$, and from equation (5.27) the View Factor from the whole flame to the sensor is obtained as

$$\begin{aligned} \text{VF}_{F-S} &= A_S \cdot (\frac{\text{VFF}_{S-F}}{A_F} + \frac{\text{VFB}_{S-F}}{A_B}) \\ \\ &= \frac{1}{2} \cdot \text{VF}_{S-F} \cdot A_S (\frac{1}{A_F} + \frac{1}{A_B}) \end{aligned} \tag{5.29}$$

All given areas are constants. From equation (5.29) it follows that

$$\text{VF}_{F-S} \propto \text{VF}_{S-F}$$

For the following comparison of measured sensor signal and View Factors it is therefore valid to work with the VF equation presented in 5.24.

5.3. Results and discussion

To evaluate the potential of using View Factors to quantify the influence of the sensor position on the sensor signal strength, the derived View Factor equation is solved for each sensor position tested in the experimental parameter study. As in the empirical studies, the three parameters that determine the sensor position are varied individually. The horizontal distance of sensor to flame (X) is increased first, then the vertical distance of sensor and flame (Y) is increased. Lastly, the tilt angle α is altered.
To compare the View Factor to the measured signal curves, parameters in the VF equation have to be substituted in the following way.

$$p_s = X_{\text{Study}}$$
$$h_s = Y_{\text{Study}}$$
$$\alpha = \alpha_{\text{Study}}$$

The constants h_{tip} and r take values

$$h_{\text{tip}} = 15.5mm$$
$$r = 1.5mm$$

Radius r is equal to the radius of the nozzle, h_{tip} is found with figure 4.7a as described in chapter 4. β is then

$$\beta = \arctan(\frac{r}{h_{\text{tip}}}) = \arctan(\frac{1.5}{15.5}) \approx 5.5^\circ \tag{5.30}$$

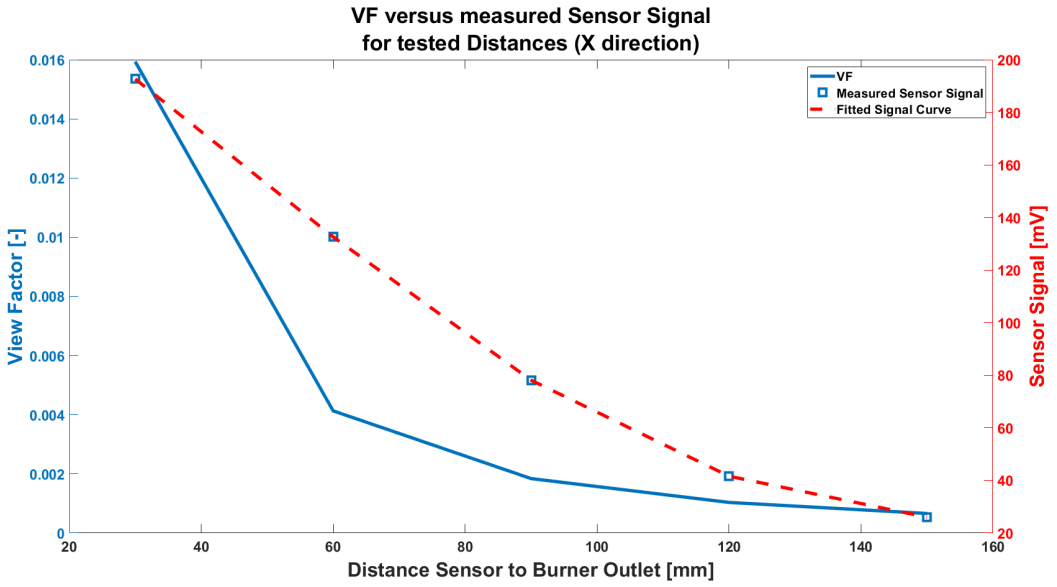

Figure 5.2: VF and measured sensor signal for an increasing horizontal distance between the sensor and the flame. Curves show same behaviour, but signal decays more linearly.

Figure 5.2 shows the VF for an increasing horizontal distance between the sensor and the flame. The curve follows the X-signal curve, but decays faster than the measured sensor signal. The decay follows the *inverse square law* given in equation (4.1) in chapter 4.

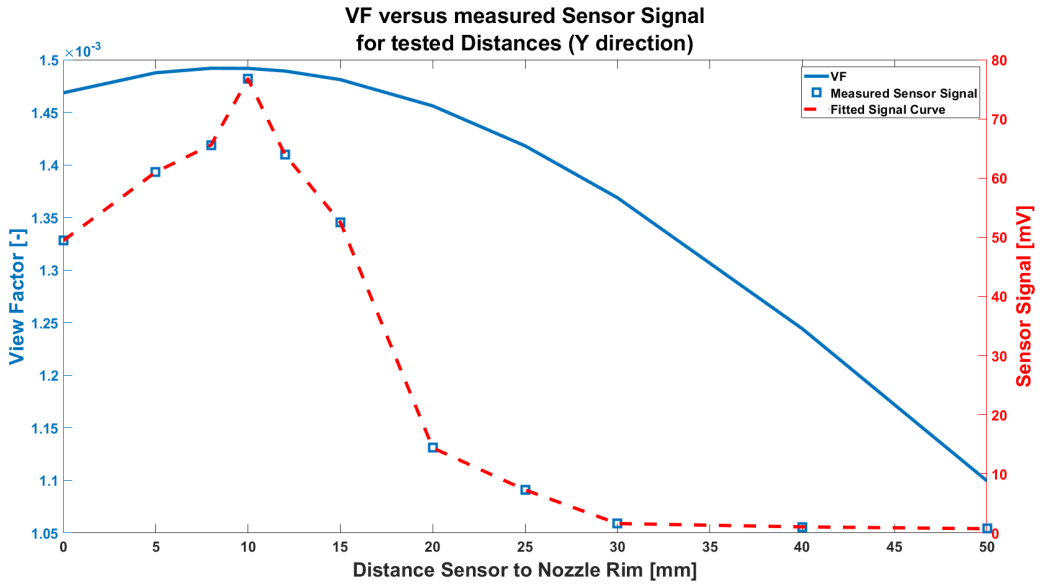

Figure 5.3: VF and measured sensor signal for increasing sensor height. Curves show similar behaviour and peak at about the same position. Sensor signal decreases steeper than VF.

Figure 5.3 displays the VF for increasing sensor height, compared to the measured sensor signal strength. Again, the curves show the same behaviour. Both peak at about the same height, although the sensor signal decays significantly for $Y > 15$, whereas the VF curve decreases smoothly.

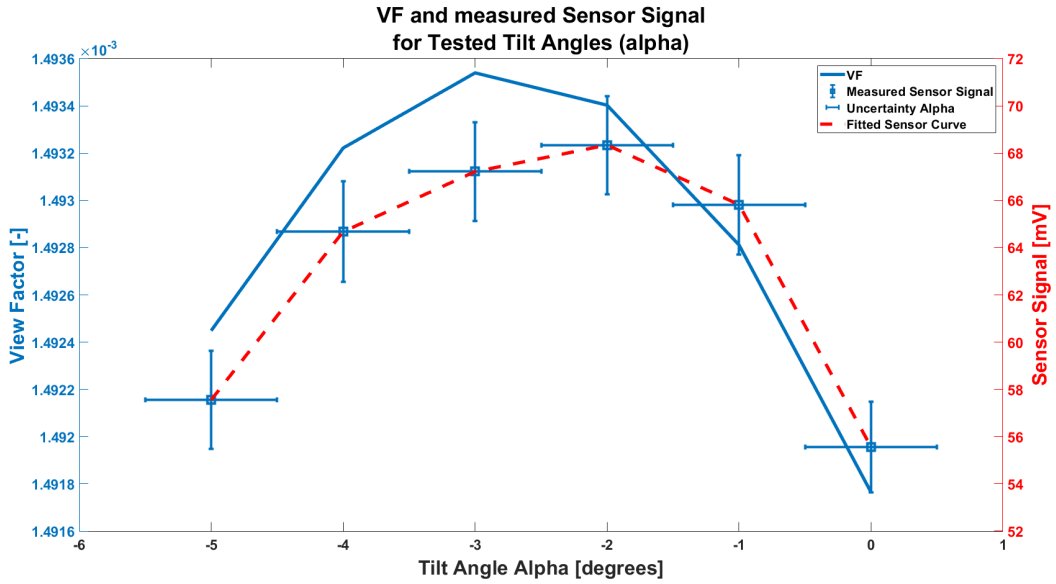

Figure 5.4: VF and sensor signal if sensor is tilted towards the flame base. Curves reveal same shape, but peak at a different position.

Figure 5.4 shows the VF and the sensor signal when the sensor is tilted towards the flame base. Although both curves reveal the same shape, the VF peaks at a greater inclination than the sensor signal. When the sensor is tilted downwards, the distance between sensor and flame surface increases. However, at a certain point the connecting line S from sensor to surface is equal to the surface normal. This might explain the increase for $0° \leq \alpha \leq 3°$. It is visible that the VF changes much less in absolute value than the sensor signal strength. For better comparison, the curves are normalized with their maximum value and compared again in figure 5.5. It reveals that the changes in the VF are barely apparent.

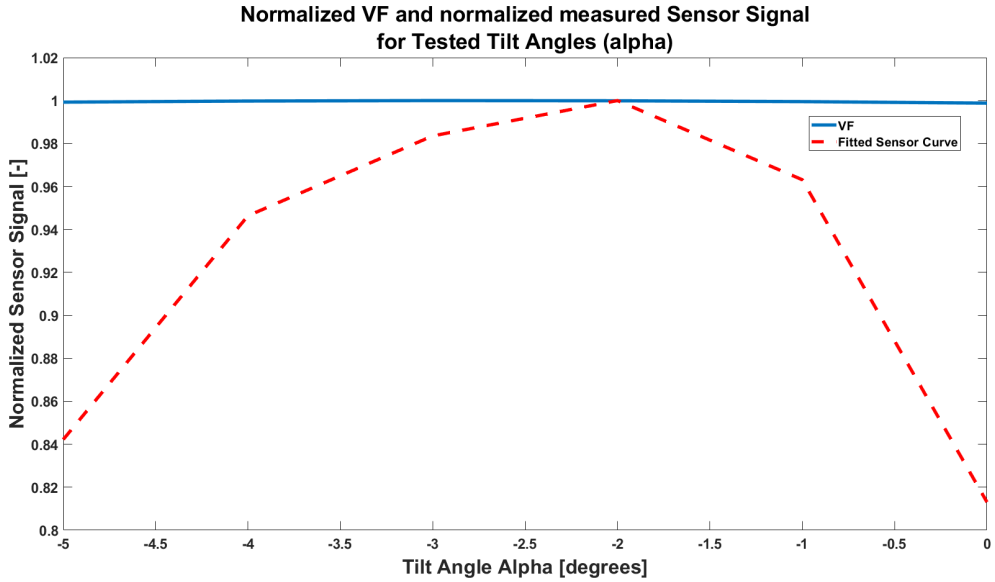

Figure 5.5: Normalized VF and normalized sensor signal if sensor is tilted towards the flame base. View Factor reveals almost invisible change, whereas change in sensor signal is clearly visible.

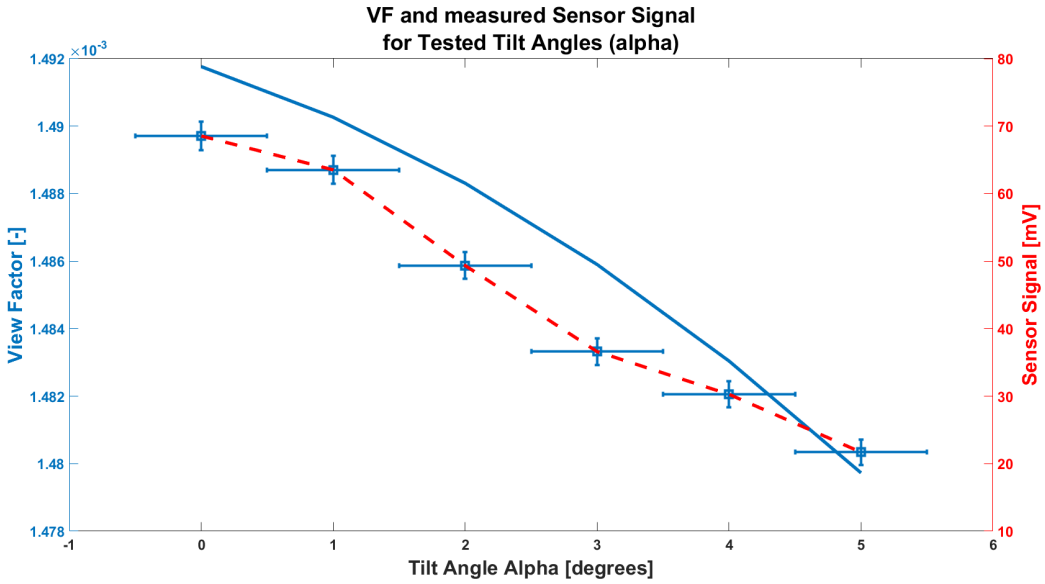

Figure 5.6: VF and measured sensor signal if sensor is tilted towards the flame tip. Sensor signal decays more linearly.

In figure 5.6, values for the VF and the measured sensor signal are compared when tilting the sensor towards the flame tip. Again, the shape of the curves shows a very similar decay. The VF decays more for greater values of α, whereas the sensor signal appears to decay almost linearly. As for the positive tilt angles, the change in sensor signal is much greater compared to the change in VF. Therefore, the normalized curves are shown in figure 5.7. It is evident that the VF remains almost constant, whereas the decay for the sensor signal is clearly noticeable.

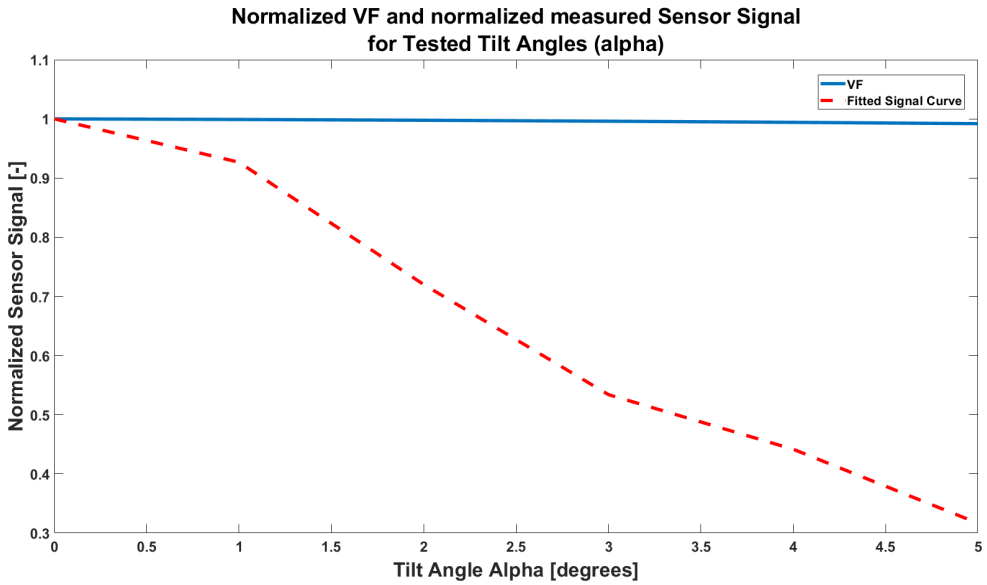

Figure 5.7: Normalized VF and normalized measured sensor signal if sensor is tilted towards the flame tip. View Factor reveals almost non-visible change, whereas change in sensor signal is clearly visible.

The figures presented above lead to the following conclusion. The View Factor displays the influence of the sensor position on the signal strength considerably well, the qualitative behaviour matches with the empirical data. However, a more accurate description of peaks and exact decays is not possible, nicely visible in figure 5.3.
As mentioned earlier, the VF does not take into account that the flame emits UV light inhomogeneously over the surface, because the gas composition and temperature changes with height. The chemiluminescence images in appendix B show the spatial distribution of the intensity for flames with different equivalence ratios. Figures 5.5 and 5.7 reveal clearly that the assumption of a homogeneous intensity leads to inaccuracies. It is important to be able to describe the influence of the position very precise, given the dimensions of damage that can result from a wrong operation of the appliance due to inaccurate information about the state of combustion. If the spatial distribution of emission intensity is not implemented into the calculations, the VF is not a sufficiently reliable indication of the influence of the sensor position on the measured signal strength. It is therefore recommended to account for different emission intensities. One approach can be to identify sufficiently small areas of the flame, where the intensity can be considered as homogeneous. After identifying those areas, the influence of these areas on the VF can be weighted according to the emission levels. Since the spatial distribution of the emission intensity changes with the equivalence ratio (see images in appendix B), the issue has to be investigated individually for each equivalence ratio.
A second remark concerns the open tip of lean hydrogen flames. The View Factor does not consider this missing part of the flame geometry, which leads to an overprediction. As long as the tip contributes weakly to the emission, this might be negligible. As discussed above, the spatial distribution of the emission intensity changes with the equivalence ratio. Therefore, this issue has to be evaluated for each equivalence ratio.

5.4. Comparison to case in literature

The paper "A formulation of Radiation View Factors from Conical Surfaces", published 1984 by B.T.F. Chung, M.M. Kermani and M.H.N. Naraghi, presents a View Factor equation for radiation from an element to a cone (see reference [6]), to determine the View Factor between i.e. a spacecraft and the exhaust plume of its engine. The initial approach was to verify the View Factor equation that Chung et al. give in eq. (8), and to extend it to the case of this study by converting their parameters into the parameters of this study and by implementing the View Factor for the backside of the cone. An exhaust plume is optically thick, therefore only the frontside of the cone was relevant for Chung et al. The flame in this work is assumed to be optically thin, therefore the contribution of the backside of the flame has to be taken into account. Unfortunately, the numerical results obtained with the VF equation from Chung et al. are not reasonable, since they give negative values. Efforts have been made to find out what causes these, but no coherent explanation has been found. Since the formulas for the stepwise derivation of the final VF equation can be simplified in different ways, it is difficult to understand clearly what causes the negative results. Therefore, a new View Factor equation was derived as described above, based on the approach of Chung et al. Nevertheless, the case of Chung et al. is discussed below.

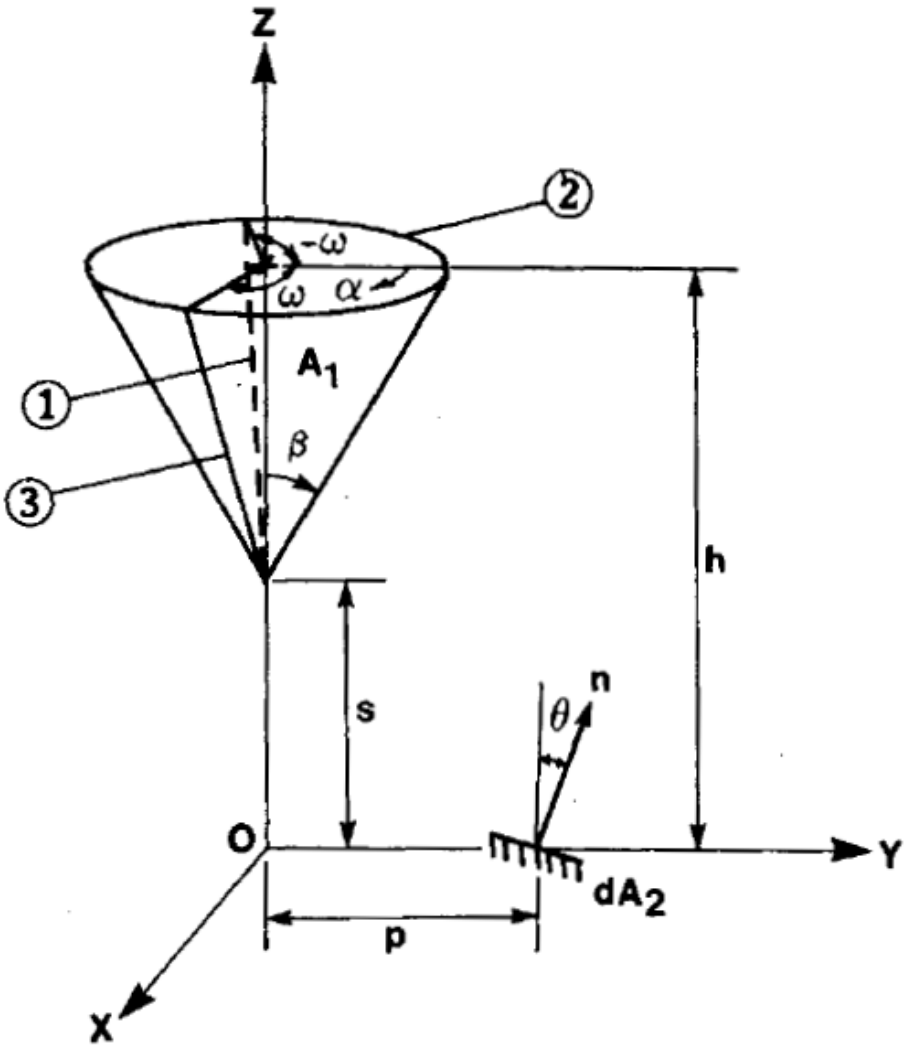

Fig. 1 Cone-differential element view factor geometry for case I.

Figure 5.8: Case for which Chung et al. derived a View Factor. Figure taken from reference [6].

Figure 5.8 illustrates the case for which they developed a VF. Looking back to figure 5.1, the following differences are visible: The cone is turned around and the tip is pointing into the negative direction of the Z axis. The distance from flame tip to origin of the coordinate system is given as s, the distance from the flame base to the origin is given as h. The sensor is positioned on the Y axis, instead of at the side of the cone. Its distance on the Y axis is p.
As for the the case in figure 5.8, the two boundaries for which the contour integral is solved are line 1 and the partial circumference of the cone base, labelled with number 2. The final equation for the View Factor is given in eq. (8) in the paper.

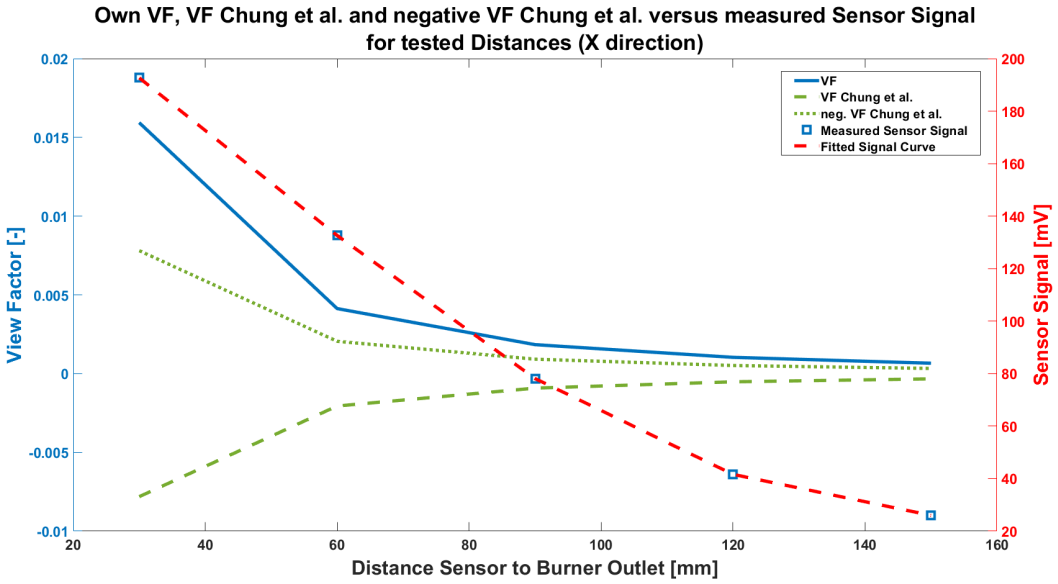

Figure 5.9: View Factor derived in this study, View Factor derived from Chung et al., negative VF derived from Chung et al. and measured sensor signal for increasing horizontal distance between sensor and flame.

Figure 5.9 shows an example of the result obtained with the derived VF equation (5.24) and equation (8) taken from the paper, compared to the sensor signal measurements. For all tested parameters, the numerical values of the VF computed from eq. (8) of Chung et al. differ in sign from the values found with the VF equation derived in this study. Since the View Factor is by definition a positive quantity , there has to be an error in the equation from Chung et al. Closer inspection show, that the numerical results for the frontside View Factor VFF found in this work is almost equal to the absolute numerical values of Chung et al.'s VF. Figure 5.10 shows the deviation between both View Factors for the X and Y direction. The values are computed as

$$\text{Deviation} = 0.5 \cdot VF_{\text{own}} + VF_{\text{Chung}} \tag{5.31}$$

The deviation is at most $1.6 \cdot 10^{-4}$ for the X direction and $3.73 \cdot 10^{-4}$ for the Y direction. Figure 5.11 shows the deviation between both View Factors for the inclination of the sensor α. The deviation is at most $5.5 \cdot 10^{-6}$ for $\alpha < 0°$ and $-2.43 \cdot 10^{-6}$ for $\alpha < 0°$.

It is not clear, what leads to these (small) deviations. A mistake was found in eq. (5) of the paper. The corrected equation is

$$S^2 = \gamma^2 \cdot \csc^2(\beta) - 2\gamma(p \cdot \cos(\omega) - s \cdot \cot(\beta)) + s^2 + p^2$$

However, it is not clear whether this mistake leads to the deviation. It does not explain the opposite sign of the VF from Chung et al.

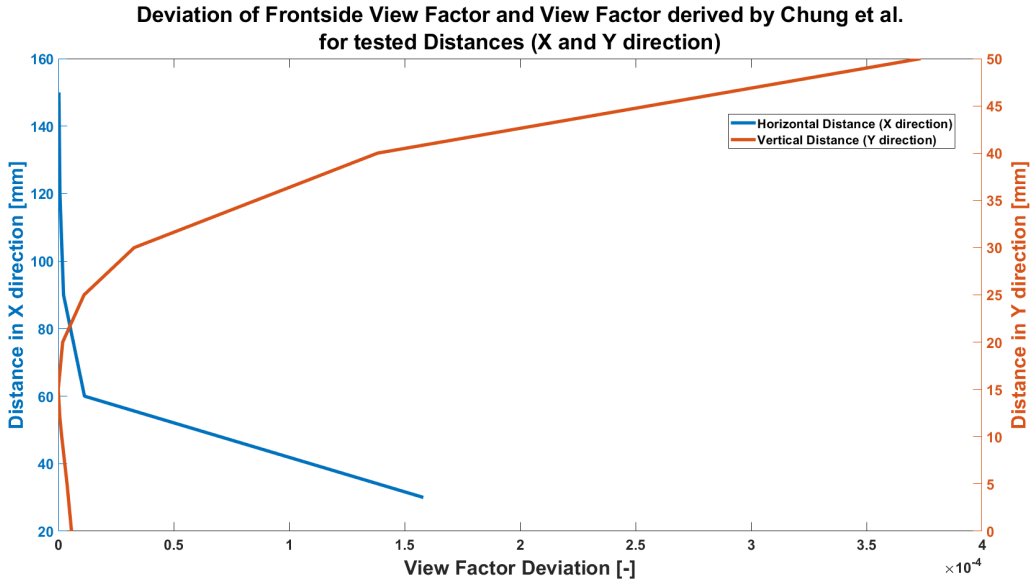

Figure 5.10: Deviation of frontside View Factor derived in this study and View Factor derived from Chung et al. for increasing X and Y distance. The deviation is at most $1.6 \cdot 10^{-4}$ for the X direction and $3.73 \cdot 10^{-4}$ for the Y direction.

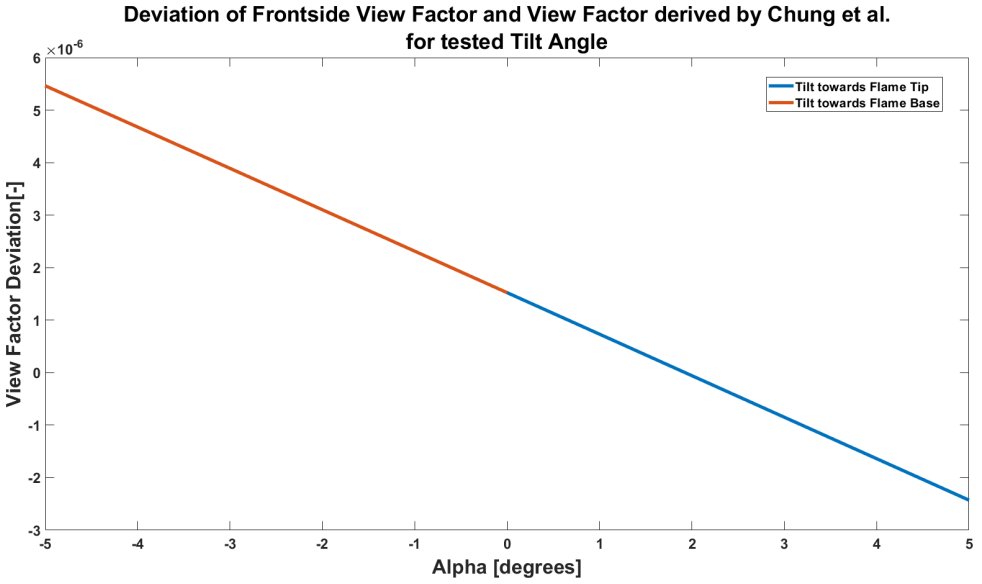

Figure 5.11: Deviation of frontside View Factor derived in this study and View Factor derived from Chung et al. for tilt angle α. The deviation is at most $1.6 \cdot 10^{-4}$ for the X direction and $3.73 \cdot 10^{-4}$ for the Y direction.

6

Conclusion and recommendations

The work presented is motivated by the question of whether the application of UV sensor technology for flame detection and flame monitoring in hydrogen-powered gas boilers is feasible.
The following four questions arose:

1. Is the sensor sensitive enough to detect lean flames of $\phi = 0.5$ and $\dot{V} = 2\text{L/min}$ with resulting low radiation levels?
2. Is the sensor sensitive to changes in the equivalence ratio of $\Delta\phi = 0.05$?
3. How does the sensor signal depend on the position of the sensor with respect to the flame?
4. Can the dependence of sensor signal on sensor position be described analytically?

The given questions were investigated following different approaches. Questions 1 to 3 were subject to an empirical study. With the developed experimental setup described in chapter 2, the sensor signal strength was measured for flames with low emission levels ($\phi = 0.5$ and volume flow $\dot{V} = 2\text{L/min}$) at different sensor positions and for a range of equivalence ratios $0.5 \leq \phi \leq 1.7$.
It was possible to answer questions 1 to 3 from the studies conducted:

1. Yes, the sensor is sensitive enough to detect flames of $\phi = 0.5$ and $\dot{V} = 2\text{L/min}$. This is shown with the sensor signal curve for low values of ϕ presented in section 4.1, as well as the results of the parameter study described in section 4.2, since these measurements were carried out with a flame of $\phi = 0.5$ and $\dot{V} = 2\text{L/min}$ and the flame was detected from almost all positions.
2. Yes, the sensor is sensitive to changes in equivalence ratio of $\Delta\phi = 0.05$. The predicted operational range of the appliance is given as $0.5 \leq \phi \leq 0.75$. For this range of equivalence ratios, the curve presented in figure 4.9, chapter 4, reveals a clear relation between ϕ and sensor signal strength. However, said relation is not as unambiguous for rich flames. Further research should determine the minimal detectable change in equivalence ratio $\Delta\phi$, and is necessary in order to find a strategy for relating the sensor signal to a distinct equivalence ratio for rich flames. An investigation of the mechanisms that lead to the emission values could help to identify additional parameters that may support the monitoring strategy.
3. The dependence of the signal strength on the sensor position is reported for those parameters that define the position individually. The parameters are the horizontal distance to the flame, the vertical distance to the flame and the inclination of the sensor. Each parameter has a visible influence on the sensor signal, that is clearly described in the curves presented in section 4.2. Only for a few examined sensor positions is detection of the flame not possible. This concerns the positioning of the sensor at heights greater than $50mm$ above the nozzle rim, for a horizontal distance of $100mm$ and a neutral sensor position (no tilt). Although the sensor detects the flame for almost all tested positions, some recommendations are made herein to prevent strong signal losses. The horizontal distance affects the sensor signal strength less than the vertical distance. Installing the sensor at heights lower than $20mm$ is recommended. Regarding the tilt angle of the sensor, installing the sensor in a position where it is directed to the flame base, such as $-2°$ for a horizontal distance of $100mm$ and a vertical distance of $10mm$ is recommended.

The observed influence of the sensor position on the signal strength led to question 4. If the influence is described analytically, a correction factor can be calculated and applied to the measured signal strength, to ensure a correct translation from measured signal to the actual emission of the flame. It has been investigated whether the View Factor concept can be applied to the given case of a flame emitting to a sensor. The View Factor was derived as a function of the parameters that describe the sensor position and evaluated for the same sensor positions that were subject of the empirical study. Comparing the experimentally obtained results to the VF evaluation, question 4 is answered as:

4. The derived View Factor equation cannot be used without further improvements. Qualitatively, the calculated values match the empirical observations (see figures 5.2, 5.3, 5.4 and 5.6). However, accuracy is low because peaks or abrupt decays are not reflected in the View Factor curves. Three aspects are not included in the VF equation. Firstly, the VF does not take into account that the flame does not emit UV light homogeneously over the surface. It should be further investigated whether it can be improved by identifying areas of the flame, where the intensity is homogeneous. The influence of these areas on the VF can then be weighted according to the emission levels. Secondly, the View Factor does not reflect a possible tip opening, which happens for lean flames, hence for flames within the operational range of the boiler. For each equivalence ratio it has to be examined whether the contribution of the flame tip is negligible, or if the issue has to be included in the VF. Lastly, the VF does also not include the influence of the Field of View of the sensor. If all three can be implemented, the View Factor is a promising approach for an analytical description of the influence of the sensor position. Alternatively, the influence of the sensor position can be determined experimentally. If enough data is generated, a look up table can be used to find the correction factor for the measured sensor signal for the given position. However, this would require a lot of effort. Another alternative could be to combine the influence that was found for each parameter individually and to extrapolate the data for the desired sensor position.

Regarding the developed setup, several ideas should be evaluated to further improve safety and the accuracy of the results, or to add possibilities for further investigations.

— A flame arrestor was designed for the burner but was not delivered before the studies were conducted. To improve the security of the setup further, this flame arrestor should still be implemented.

— To protect the flame from fluctuations in the surrounding air and to increase flame stability, a quartz glass frame was designed. Like the flame arrestor, it was not ready early enough to be used during the measurements, but should be used for further working with the setup.

— To overcome fluctuations of the equivalence ratio induced by instabilities of the mass flow controllers, a volume can be added to the gas supply path.

— To improve the interpretation of the measured sensor signal it is recommended to investigate the quantitative influence of temperature fluctuations.

— To determine the flame height more accurately, UV chemiluminescence images should be used, instead of pictures of visible light emissions. One possible realization is the conversion of the image dimensions from pixels to values of absolute length.

— It is recommended to improve the sharpness of chemiluminescence images by installing the CCD camera further away from the flame. Measurements should then be conducted for flames with higher emission intensities, since signal decreases with increasing distance.

— If the camera can be calibrated (i.e. with a light source of known irradiation) absolute emission values could be obtained from the chemiluminescence images. This would be interesting, since there is little information on absolute values in literature.

Bibliography

[1] P. G. Aleiferis and Rosati M. F. Flame chemiluminescence and oh lif imaging in a hydrogen-fuelled spark-ignition engine. *International Journal of Hydrogen Energy*, 37(2):1797 – 1812, 2012. ISSN 0360-3199. doi: https://doi.org/10.1016/j.ijhydene.2011.10.010. URL http://www.sciencedirect.com/science/article/pii/S0360319911023020. 10th International Conference on Clean Energy 2010.

[2] V. Alekseev. *Laminar burning velocity of hydrogen and flame structure of related fuels for detailed kinetic model validation*. PhD thesis, Combustion Physics, 2015. Defence details Date: 2015-11-27 Time: 14:00 Place: Lecture hall Rydbergsalen, Department of Physics, Professorsgatan 1, Lund University, Faculty of Engineering External reviewer(s) Name: Mounaïm-Rousselle, Christine Title: Professor Affiliation: Laboratoire PRISME, Université d'Orléans, Orléans, France —.

[3] E. E. Arens, R. C. Youngquist, and S. O. Starr. Intensity calibrated hydrogen flame spectrum. *International Journal of Hydrogen Energy*, 39(17):9545 – 9551, 2014. ISSN 0360-3199. doi: https://doi.org/10.1016/j.ijhydene.2014.04.043. URL http://www.sciencedirect.com/science/article/pii/S0360319914010647.

[4] J. Ballester and T. García-Armingol. Diagnostic techniques for the monitoring and control of practical flames. *Progress in Energy and Combustion Science*, 36(4):375 – 411, 2010. ISSN 0360-1285. doi: https://doi.org/10.1016/j.pecs.2009.11.005. URL http://www.sciencedirect.com/science/article/pii/S0360128509000689.

[5] N. Bouvet, C. Chauveau, I. Gökalp, S.-Y. Lee, and R. Santoro. Characterization of syngas laminar flames using the bunsen burner configuration. *International Journal of Hydrogen Energy*, 36:992–1005, 01 2011. doi: 10.1016/j.ijhydene.2010.08.147.

[6] B. Chung, M. Kermani, and M. Naraghi. A formulation of radiation view factors from conical surfaces. *AIAA Journal*, 22, 03 1984. doi: 10.2514/3.48465.

[7] C. J. Dasch. One-dimensional tomography: a comparison of abel, onion-peeling, and filtered backprojection methods. *Appl. Opt.*, 31(8):1146–1152, Mar 1992. doi: 10.1364/AO.31.001146. URL http://ao.osa.org/abstract.cfm?URI=ao-31-8-1146.

[8] M. G. Davis, W. K. McGregor, and A. A. Mason. Oh chemiluminescent radiation from lean hydrogen-oxygen flames. *The Journal of Chemical Physics*, 61(4):1352–1356, 1974. doi: 10.1063/1.1682059. URL https://doi.org/10.1063/1.1682059.

[9] Y. Ding, D. Durox, N. Darabiha, and T. Schuller. Combustion state monitoring of premixed heating appliances with flame ionization current and chemiluminescence. *Combustion Science and Technology*, 191 (2):382–401, 2019. doi: 10.1080/00102202.2018.1472085. URL https://doi.org/10.1080/00102202.2018.1472085.

[10] Y. Ding, D. Durox, N. Darabiha, and T. Schuller. Chemiluminescence based operating point control of domestic gas boilers with variable natural gas composition. *Applied Thermal Engineering*, 149:1052 – 1060, 2019. ISSN 1359-4311. doi: https://doi.org/10.1016/j.applthermaleng.2018.12.106. URL http://www.sciencedirect.com/science/article/pii/S135943111835703X.

[11] N. Docquier and S. Candel. Combustion control and sensors: a review. *Progress in Energy and Combustion Science*, 28(2):107 – 150, 2002. ISSN 0360-1285. doi: https://doi.org/10.1016/S0360-1285(01)00009-0. URL http://www.sciencedirect.com/science/article/pii/S0360128501000090.

[12] EBN. Energy in numbers 2020, 2020. URL https://www.energieinnederland.nl/feiten-en-cijfers/infographic/. [Online; visited on 30.06.2020].

[13] Edmund Optics. Coating Curve, 310nm CWL TECHSPEC 10nm OD4 Bandpass Filter, 2020. URL https://www.edmundoptics.com/p/310nm-cwl-50mm-dia-hard-coated-od-4-10nm-bandpass-filter/33106/. [Online; visited on 01.06.2020].

[14] Eurostat. Where does our energy come from?, 2020. URL https://ec.europa.eu/eurostat/cache/infographs/energy/bloc-2a.html. [Online; visited on 30.06.2020].

[15] Eurostat. Energy consumption in households, 2020. URL https://ec.europa.eu/eurostat/statistics-explained/index.php/Energy_consumption_in_households. [Online; visited on 30.06.2020].

[16] T. Fiala and T. Sattelmayer. Modeling of the continuous (blue) radiation in hydrogen flames. *International Journal of Hydrogen Energy*, 41(2):1293 – 1303, 2016. ISSN 0360-3199. doi: https://doi.org/10.1016/j.ijhydene.2015.10.045. URL http://www.sciencedirect.com/science/article/pii/S036031991530505X.

[17] D. Giassi, S. Cao, B. Bennett, D. Stocker, F. Takahashi, M. Smooke, and M. Long. Analysis of ch* concentration and flame heat release rate in laminar coflow diffusion flames under microgravity and normal gravity. *Combustion and Flame*, 167, 03 2016. doi: 10.1016/j.combustflame.2016.02.012.

[18] Government of the Netherlands. Government Strategy on Hydrogen , 2020. URL https://www.government.nl/documents/publications/2020/04/06/government-strategy-on-hydrogen. [Online; visited on 30.06.2020].

[19] J. Graña-Otero and S. Mahmoudi. Excited oh kinetics and distribution in h2 premixed flames. *Fuel*, 255:115750, 2019. ISSN 0016-2361. doi: https://doi.org/10.1016/j.fuel.2019.115750. URL http://www.sciencedirect.com/science/article/pii/S0016236119311020.

[20] J. M. Hall and E. L. Petersen. An optimized kinetics model for oh chemiluminescence at high temperatures and atmospheric pressures. *International Journal of Chemical Kinetics*, 38(12):714–724, 2006. doi: 10.1002/kin.20196. URL https://onlinelibrary.wiley.com/doi/abs/10.1002/kin.20196.

[21] D. D. Hickstein, S. T. Gibson, R. Yurchak, D. D. Das, and M. Ryazanov. A direct comparison of high-speed methods for the numerical abel transform. *Review of Scientific Instruments*, 90(6):065115, 2019. doi: 10.1063/1.5092635. URL https://doi.org/10.1063/1.5092635.

[22] W. E. Kaskan. Abnormal excitation of oh in h2/o2/n2 flames. *The Journal of Chemical Physics*, 31(4):944–956, 1959. doi: 10.1063/1.1730556. URL https://doi.org/10.1063/1.1730556.

[23] T. Kathrotia, M. Fikri, M. Bozkurt, M. Hartmann, U. Riedel, and C. Schulz. Study of the H+O+M reaction forming OH(star): Kinetics of OH* chemiluminescence in hydrogen combustion systems. *Combustion and Flame*, 157(7):1261 – 1273, 2010. ISSN 0010-2180. doi: https://doi.org/10.1016/j.combustflame.2010.04.003. URL http://www.sciencedirect.com/science/article/pii/S0010218010001070.

[24] W. Kowalski and W. Bahnfleth. Uvgi design basics for air and surface disinfection. *HPAC Heating, Piping, Air Conditioning*, 72:10 pp, 01 2000.

[25] Y. Mizobuchi, T. Nambu, and T. Takeno. Numerical study of tip opening of hydrogen/air bunsen flame. *Proceedings of the Combustion Institute*, 37(2):1775 – 1781, 2019. ISSN 1540-7489. doi: https://doi.org/10.1016/j.proci.2018.05.025. URL http://www.sciencedirect.com/science/article/pii/S1540748918300269.

[26] K. T. Møller, T. R. Jensen, E. Akiba, and H.-w. Li. Hydrogen - a sustainable energy carrier. *Progress in Natural Science: Materials International*, 27(1):34 – 40, 2017. ISSN 1002-0071. doi: https://doi.org/10.1016/j.pnsc.2016.12.014. URL http://www.sciencedirect.com/science/article/pii/S1002007116303240. SI-HYDROGEN STORAGE MATERIALS.

[27] M. F. Modest. Chapter 4 - view factors. In Michael F Modest, editor, *Radiative Heat Transfer (Third Edition)*, pages 129 – 159. Academic Press, Boston, third edition edition, 2013. ISBN 978-0-12-386944-9. doi: https://doi.org/10.1016/B978-0-12-386944-9.50004-2. URL http://www.sciencedirect.com/science/article/pii/B9780123869449500042.

[28] H. Pitsch. Laminar Premixed Flames: Kinematics and Burning Velocity. Combustion Summer School, 2018.

[29] R. W. Schefer, W. D. Kulatilaka, B. D. Patterson, and T. B. Settersten. Visible emission of hydrogen flames. *Combustion and Flame*, 156(6):1234 – 1241, 2009. ISSN 0010-2180. doi: https://doi.org/10.1016/j.combustflame.2009.01.011. URL http://www.sciencedirect.com/science/article/pii/S0010218009000170.

[30] sglux. TOCON ABC1, Broadband SiC based UV photodetector with integrated amplifier, 2020. URL https://sglux.de/en/produkt/tocon_abc1-en/. [Online; visited on 07.06.2020].

[31] S. Singh, S. Jain, P. S. Venkateswaran, A. K. Tiwari, M. R. Nouni, J. K. Pandey, and S. Goel. Hydrogen: A sustainable fuel for future of the transport sector. *Renewable and Sustainable Energy Reviews*, 51: 623 – 633, 2015. ISSN 1364-0321. doi: https://doi.org/10.1016/j.rser.2015.06.040. URL http://www.sciencedirect.com/science/article/pii/S1364032115006127.

[32] G. P. Smith, C. Park, and J. Luque. A note on chemiluminescence in low-pressure hydrogen and methane–nitrous oxide flames. *Combustion and Flame*, 140(4):385 – 389, 2005. ISSN 0010-2180. doi: https://doi.org/10.1016/j.combustflame.2004.11.011. URL http://www.sciencedirect.com/science/article/pii/S0010218004002469.

[33] N. Speelman, L. P. H. de Goey, and J. A. van Oijen. Development of a numerical model for the electric current in burner-stabilised methane–air flames. *Combustion Theory and Modelling*, 19(2):159–187, 2015. doi: 10.1080/13647830.2014.998712. URL https://doi.org/10.1080/13647830.2014.998712.

[34] R. Stützer and M. Oschwald. The Hyperfine Structure of the OH* Emission Spectrum and its Benefits for Combustion Analysis. 01 2019.

[35] F. Takahashi, M. Mizomoto, and S. Ikai. Transition from laminar to turbulent free jet diffusion flames. *Combustion and Flame*, 48:85 – 95, 1982. ISSN 0010-2180. doi: https://doi.org/10.1016/0010-2180(82)90117-1. URL http://www.sciencedirect.com/science/article/pii/0010218082901171.

[36] J. Tan, K. Zeng, and Z. Wang. Chemiluminescence Measurements of Laminar Premixed Ethylene/Air Flame at Low Pressure. *Journal of Thermal Science and Technology*, 7:665–676, 01 2012. doi: 10.1299/jtst.7.665.

[37] United Nations / Framework Convention on Climate Change. Adoption of the Paris Agreement, 21st Conference of the Parties, 2015. URL https://unfccc.int/process-and-meetings/the-paris-agreement/the-paris-agreement. [Online; visited on 30.06.2020].

[38] F. M. White. *Fluid Mechanics, 7th edition.* McGraw-Hill Series in Mechanical Engineering, 2011.

[39] C. Xu, T. A. Kohler, T. M. Lenton, J.-C. Svenning, and M. Scheffer. Future of the human climate niche. *Proceedings of the National Academy of Sciences*, 117(21):11350–11355, 2020. ISSN 0027-8424. doi: 10.1073/pnas.1910114117. URL https://www.pnas.org/content/117/21/11350.

[40] G. J. Yates, M. Wilke, N. King, and A. Lumpkin. Ultraviolet Imaging Of Hydrogen Flames. In Robert E. Huffman, editor, *Ultraviolet Technology II*, volume 0932, pages 271 – 279. International Society for Optics and Photonics, SPIE, 1988. doi: 10.1117/12.946900. URL https://doi.org/10.1117/12.946900.

[41] M. Zhao. Experimental and numerical study of oh chemiluminescence in hydrogen diffusion flames. *Combustion and Flame*, 09 2018.

[42] M. Zhao, R. Choudhury, R. Malpress, and D. Buttsworth. Absolute concentration measurements of oh in an axisymmetric hydrogen-air premixed flame adjacent to a hot graphite model. 09 2018.

A

Assembly drawing of the burner

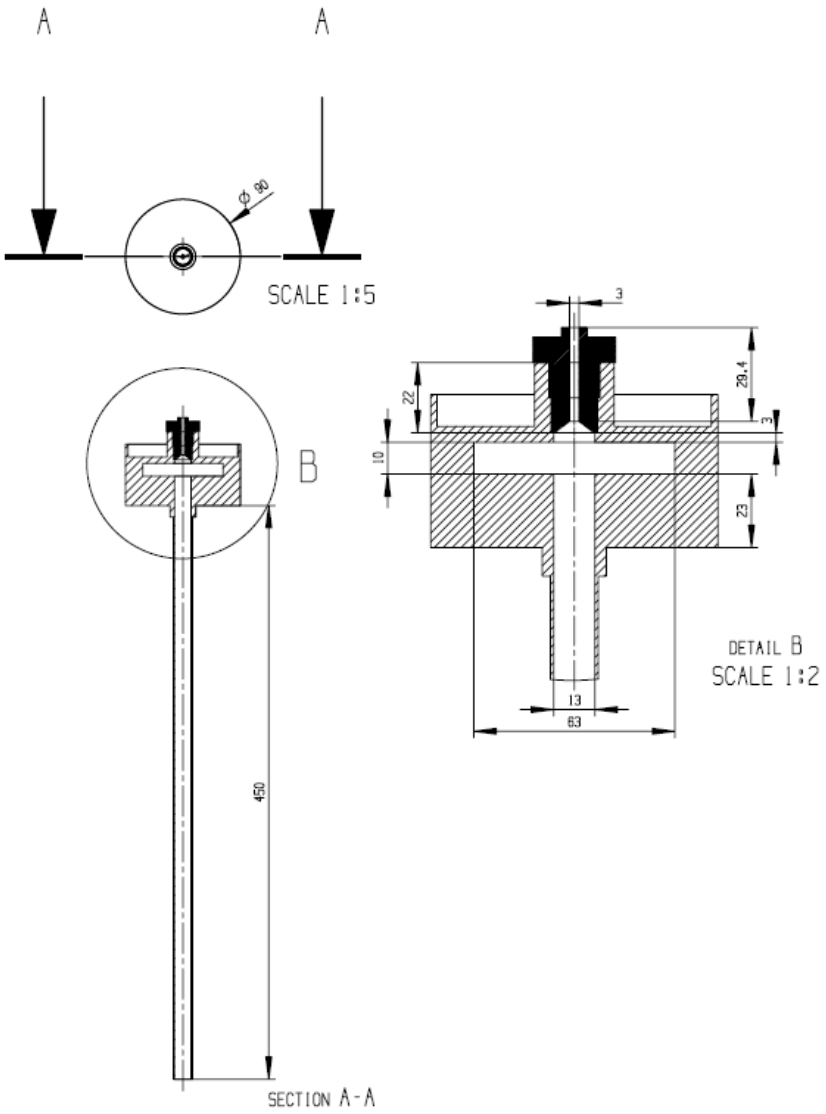

Figure A.1: Technical drawing of burner and nozzle.

B

Chemiluminescence images

To validate the empirical observations regarding the influence of the equivalence ratio on the sensor signal strength, measurement results are compared to data obtained from chemiluminescence images of the flames that are taken during the respective measurements. The images display the intensity of UV light emission qualitatively.
These images are presented for each equivalence ratio that was measured during the experiments. On the left-hand side, the line-of-sight projection of the flame is displayed. To get spatially resolved intensity images, the line-of-sight values have to be deconvoluted mathematically. An inverse Abel transform is used to reconstruct the emission values. The code is included in the *PyAbel* package for *Python*. The *3-point method* is chosen, because it is recommended by several studies (see for example [7], [41] and [21]). The results are shown on the right-hand sight of each figure.
In order to compare the image data to the sensor data, the camera is positioned at the same distance to the flame as the sensor, at $100mm$ horizontal and $10mm$ vertical distance. The sharpness of the images can be improved, if the horizontal distance to the flame is increased. However, the already low sensor signal strength would decrease even further. Since the main purpose of the chemiluminescence images was to obtain the intensity value of the complete flame, the distance of $100mm$ is the compromise between both arguments (the sharpness of the image has no influence on the total intensity). As a consequence it is recommended to take the images again, if it is desired to combine their Abel inverted values with a camera calibration to find spatially resolved absolute UV emission values.

(a) Line-of-sight UV image, exposure time $t = 80ms$.

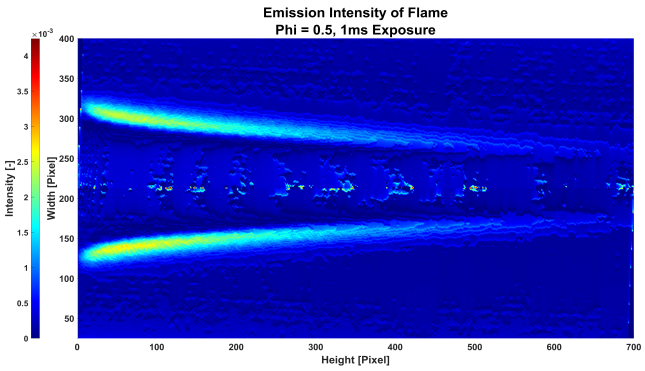

(b) Abel inverted UV image, exposure time $t = 1ms$.

Figure B.1: UV Chemiluminescence image, $\phi = 0.5$.

(a) Line-of-sight UV image, exposure time $t = 80ms$.

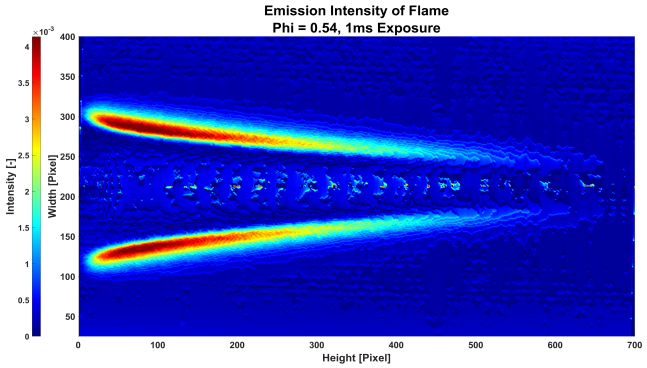

(b) Abel inverted UV image, exposure time $t = 1ms$.

Figure B.2: UV Chemiluminescence image, $\phi = 0.54$.

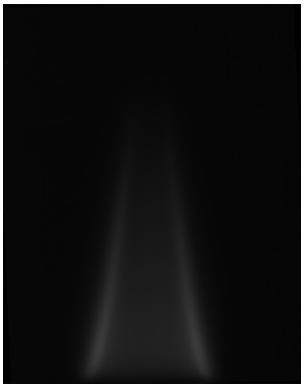

(a) Line-of-sight UV image, exposure time $t = 80ms$.

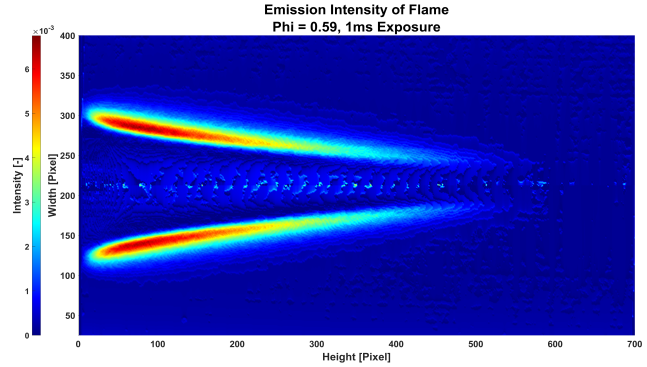

(b) Abel inverted UV image, exposure time $t = 1ms$.

Figure B.3: UV Chemiluminescence image, $\phi = 0.59$.

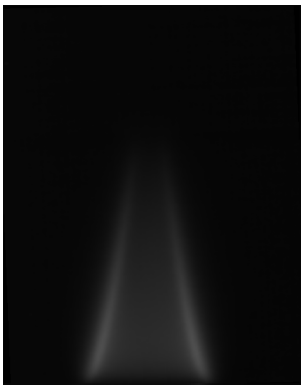

(a) Line-of-sight UV image, exposure time $t = 80ms$.

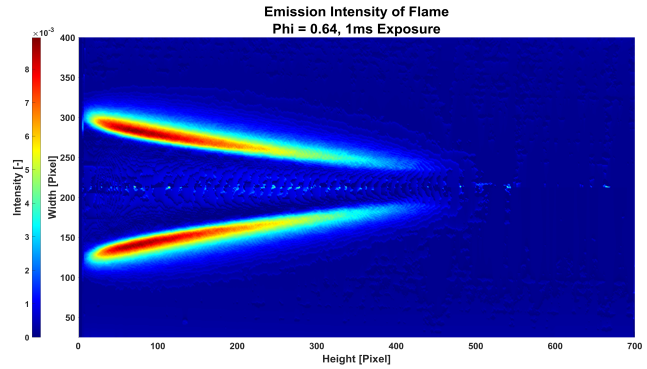

(b) Abel inverted UV image, exposure time $t = 1ms$.

Figure B.4: UV Chemiluminescence image, $\phi = 0.64$.

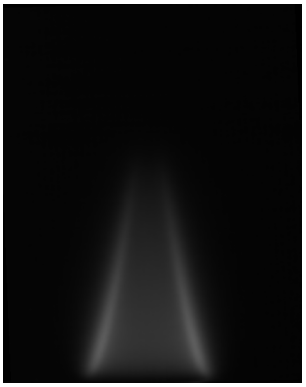

(a) Line-of-sight UV image, exposure time $t = 80ms$.

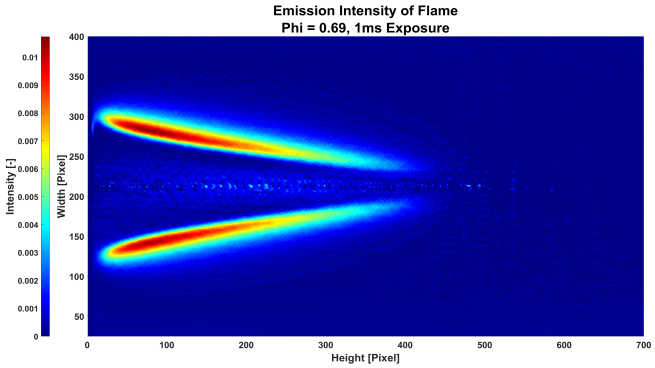

(b) Abel inverted UV image, exposure time $t = 1ms$.

Figure B.5: UV Chemiluminescence image, $\phi = 0.69$.

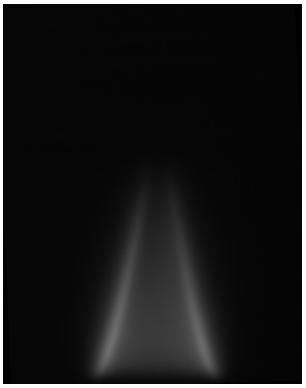

(a) Line-of-sight UV image, exposure time $t = 80ms$.

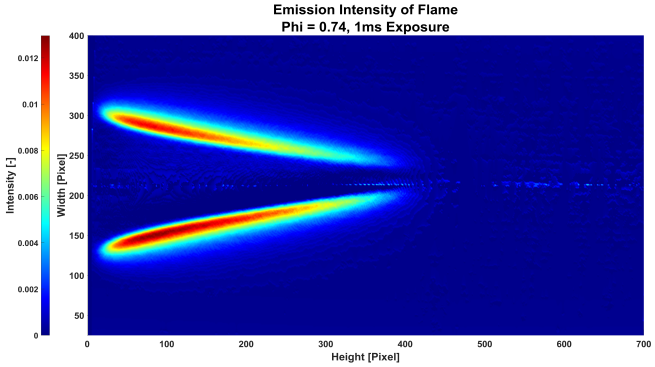

(b) Abel inverted UV image, exposure time $t = 1ms$.

Figure B.6: UV Chemiluminescence image, $\phi = 0.74$.

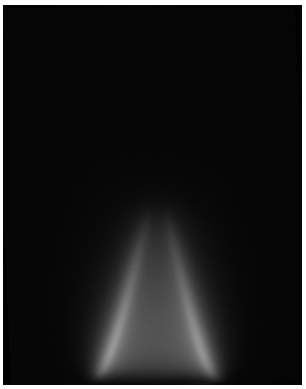

(a) Line-of-sight UV image, exposure time $t = 80ms$.

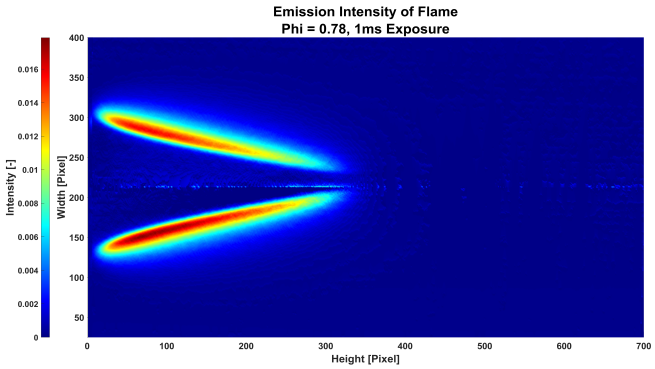

(b) Abel inverted UV image, exposure time $t = 1ms$.

Figure B.7: UV Chemiluminescence image, $\phi = 0.78$.

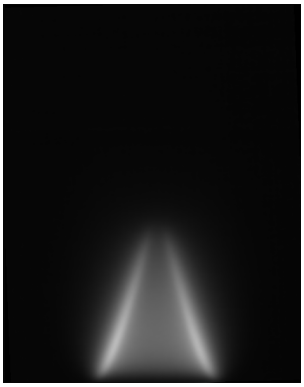

(a) Line-of-sight UV image, exposure time $t = 80ms$.

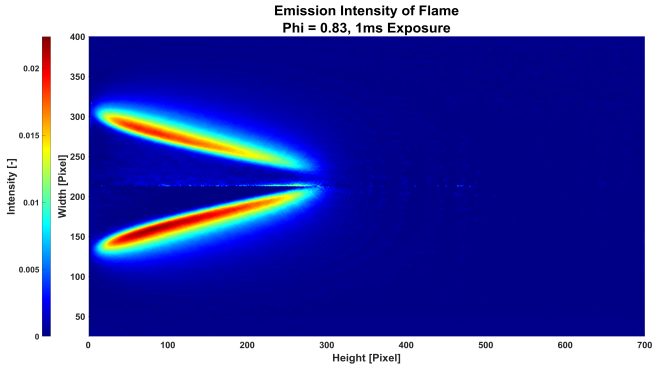

(b) Abel inverted UV image, exposure time $t = 1ms$.

Figure B.8: UV Chemiluminescence image, $\phi = 0.83$.

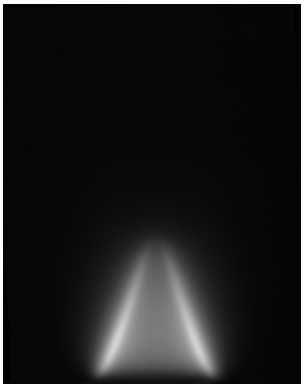

(a) Line-of-sight UV image, exposure time $t = 80ms$.

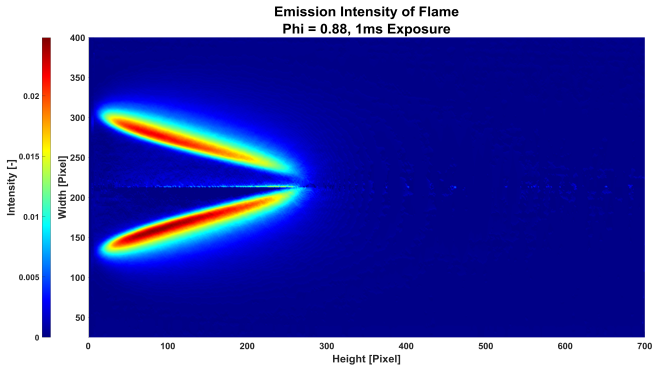

(b) Abel inverted UV image, exposure time $t = 1ms$.

Figure B.9: UV Chemiluminescence image, $\phi = 0.88$.

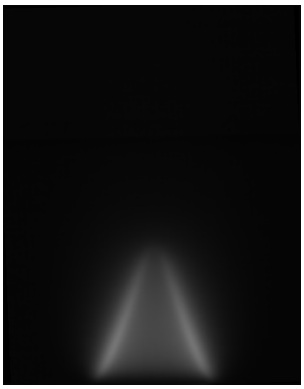

(a) Line-of-sight UV image, exposure time $t = 40ms$.

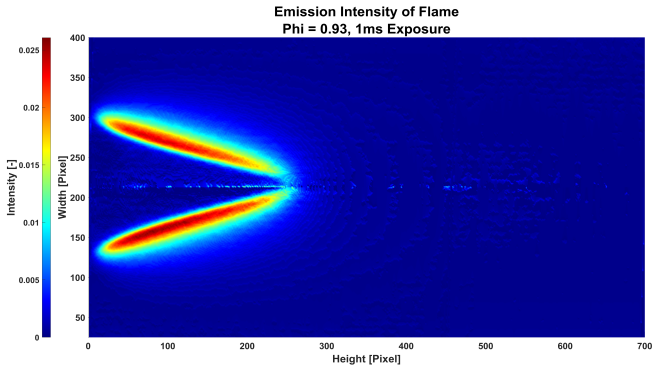

(b) Abel inverted UV image, exposure time $t = 1ms$.

Figure B.10: UV Chemiluminescence image, $\phi = 0.93$.

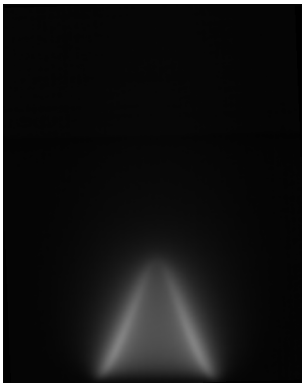

(a) Line-of-sight UV image, exposure time $t = 40ms$.

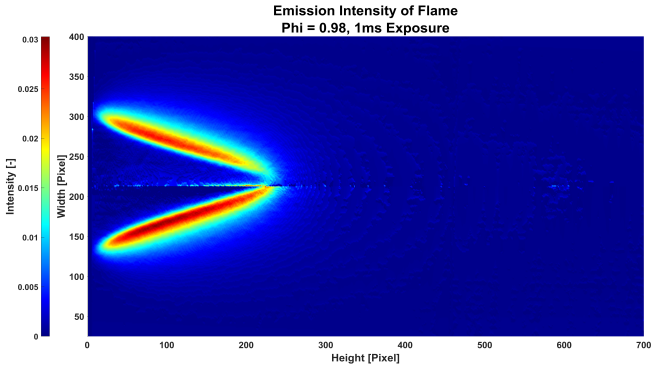

(b) Abel inverted UV image, exposure time $t = 1ms$.

Figure B.11: UV Chemiluminescence image, $\phi = 0.98$.

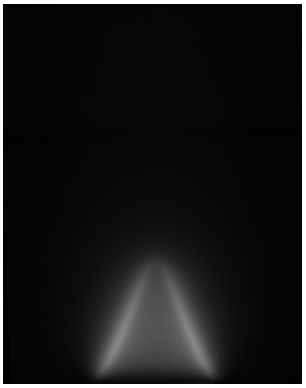

(a) Line-of-sight UV image, exposure time $t = 40ms$.

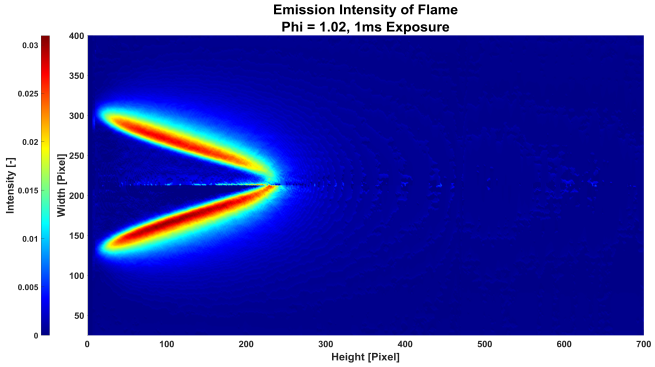

(b) Abel inverted UV image, exposure time $t = 1ms$.

Figure B.12: UV Chemiluminescence image, $\phi = 1.02$.

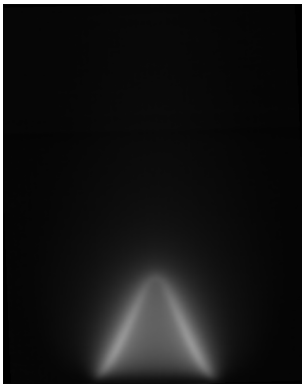

(a) Line-of-sight UV image, exposure time $t = 40ms$.

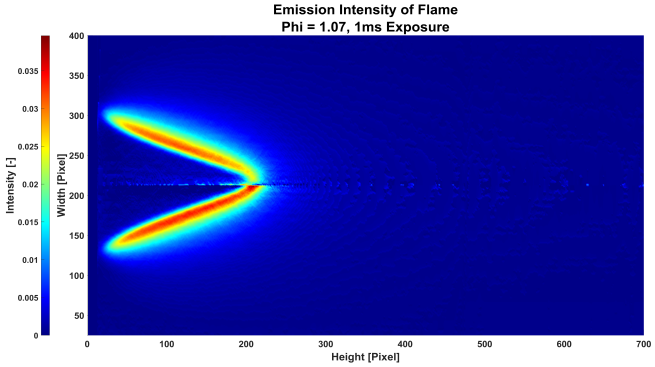

(b) Abel inverted UV image, exposure time $t = 1ms$.

Figure B.13: UV Chemiluminescence image, $\phi = 1.07$.

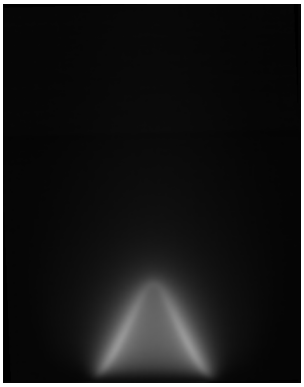

(a) Line-of-sight UV image, exposure time $t = 40ms$.

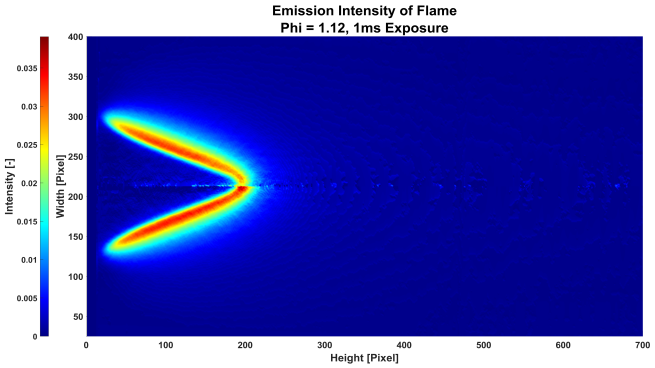

(b) Abel inverted UV image, exposure time $t = 1ms$.

Figure B.14: UV Chemiluminescence image, $\phi = 1.12$.

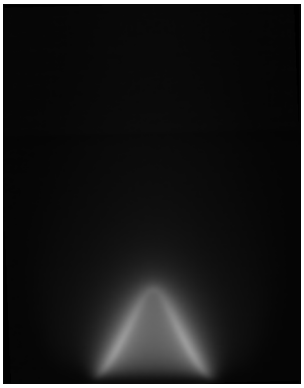

(a) Line-of-sight UV image, exposure time $t = 40ms$.

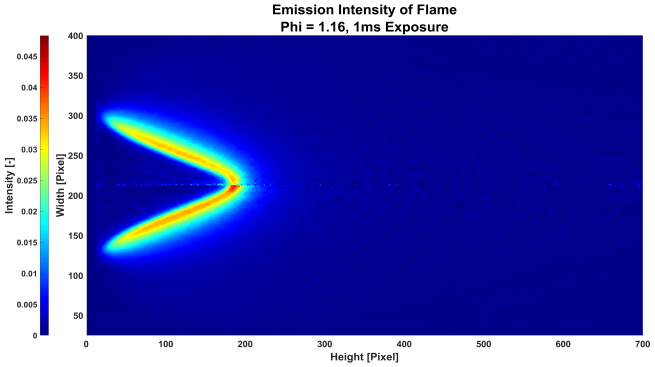

(b) Abel inverted UV image, exposure time $t = 1ms$.

Figure B.15: UV Chemiluminescence image, $\phi = 1.16$.

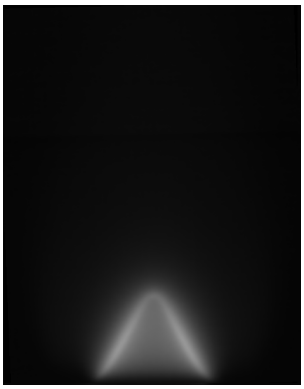

(a) Line-of-sight UV image, exposure time $t = 40ms$.

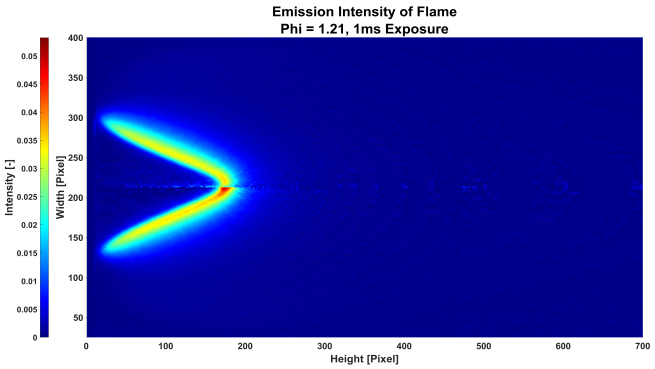

(b) Abel inverted UV image, exposure time $t = 1ms$.

Figure B.16: UV Chemiluminescence image, $\phi = 1.21$.

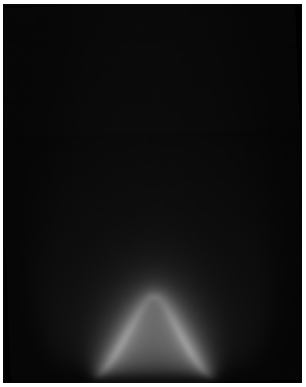

(a) Line-of-sight UV image, exposure time $t = 40ms$.

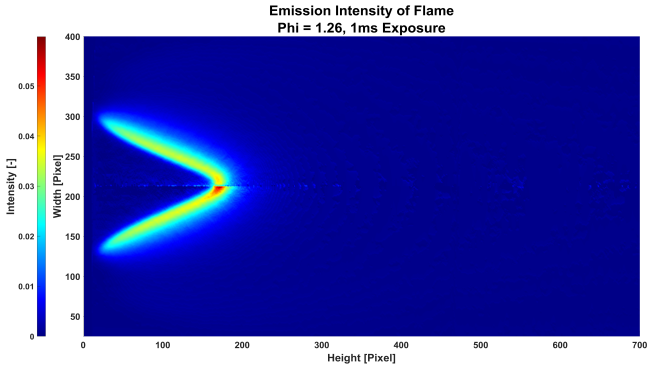

(b) Abel inverted UV image, exposure time $t = 1ms$.

Figure B.17: UV Chemiluminescence image, $\phi = 1.26$.

(a) Line-of-sight UV image, exposure time $t = 20ms$.

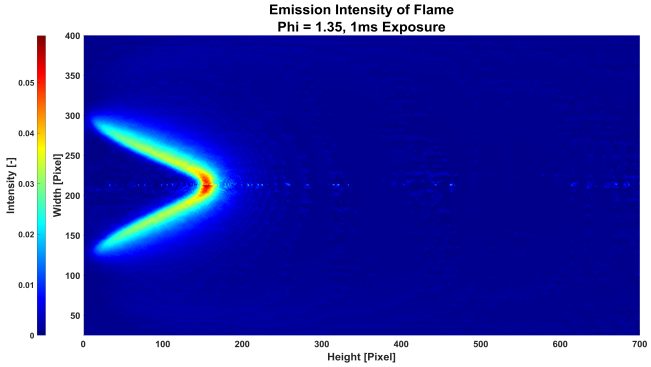

(b) Abel inverted UV image, exposure time $t = 1ms$.

Figure B.18: UV Chemiluminescence image, $\phi = 1.35$.

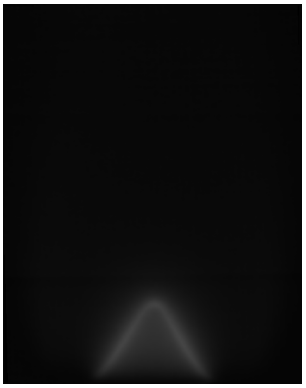

(a) Line-of-sight UV image, exposure time $t = 20ms$.

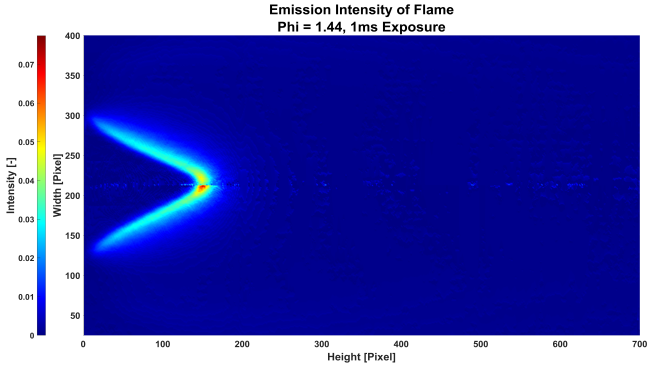

(b) Abel inverted UV image, exposure time $t = 1ms$.

Figure B.19: UV Chemiluminescence image, $\phi = 1.44$.

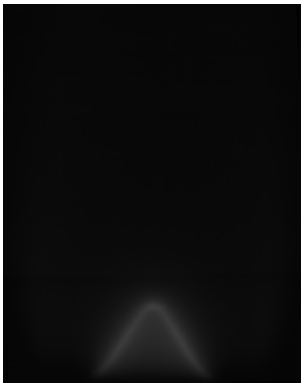

(a) Line-of-sight UV image, exposure time $t = 20ms$.

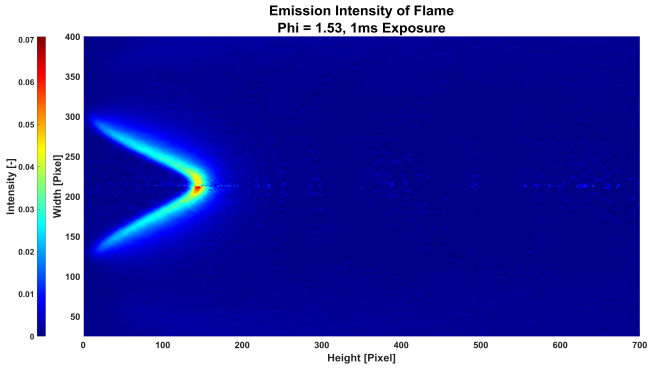

(b) Abel inverted UV image, exposure time $t = 1ms$.

Figure B.20: UV Chemiluminescence image, $\phi = 1.53$.

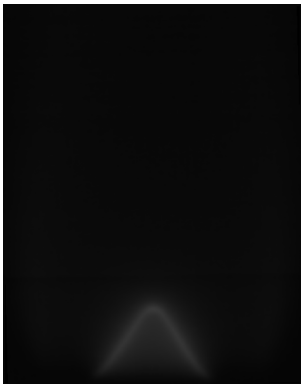

(a) Line-of-sight UV image, exposure time $t = 20ms$.

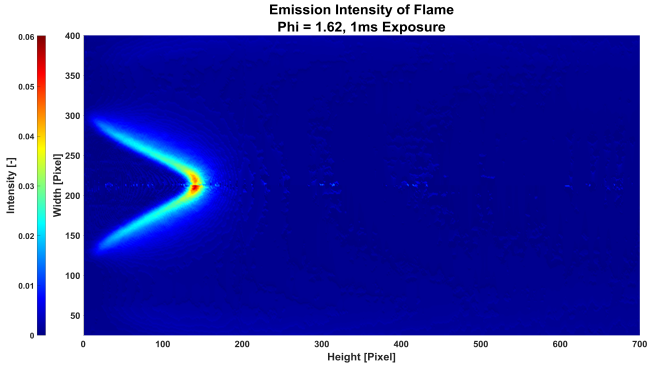

(b) Abel inverted UV image, exposure time $t = 1ms$.

Figure B.21: UV Chemiluminescence image, $\phi = 1.62$.

(a) Line-of-sight UV image, exposure time $t = 20ms$.

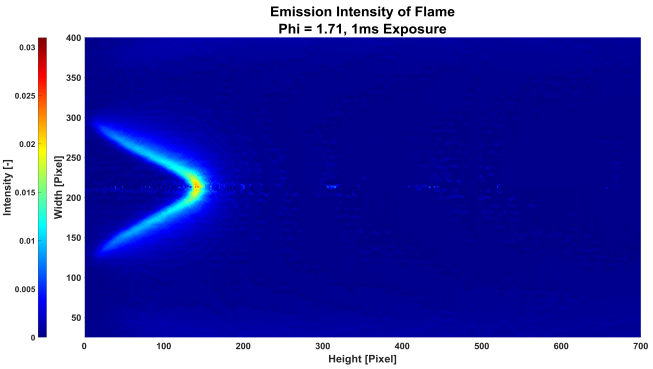

(b) Abel inverted UV image, exposure time $t = 1ms$.

Figure B.22: UV Chemiluminescence image, $\phi = 1.71$.

C

LabVIEW program

As described in section 3.2, chapter 2, a *LabVIEW* program has been written. It stores the data in table 3.1 and controls the gas volume flow supplied by the mass flow controllers. The interface is shown in figure C.1.

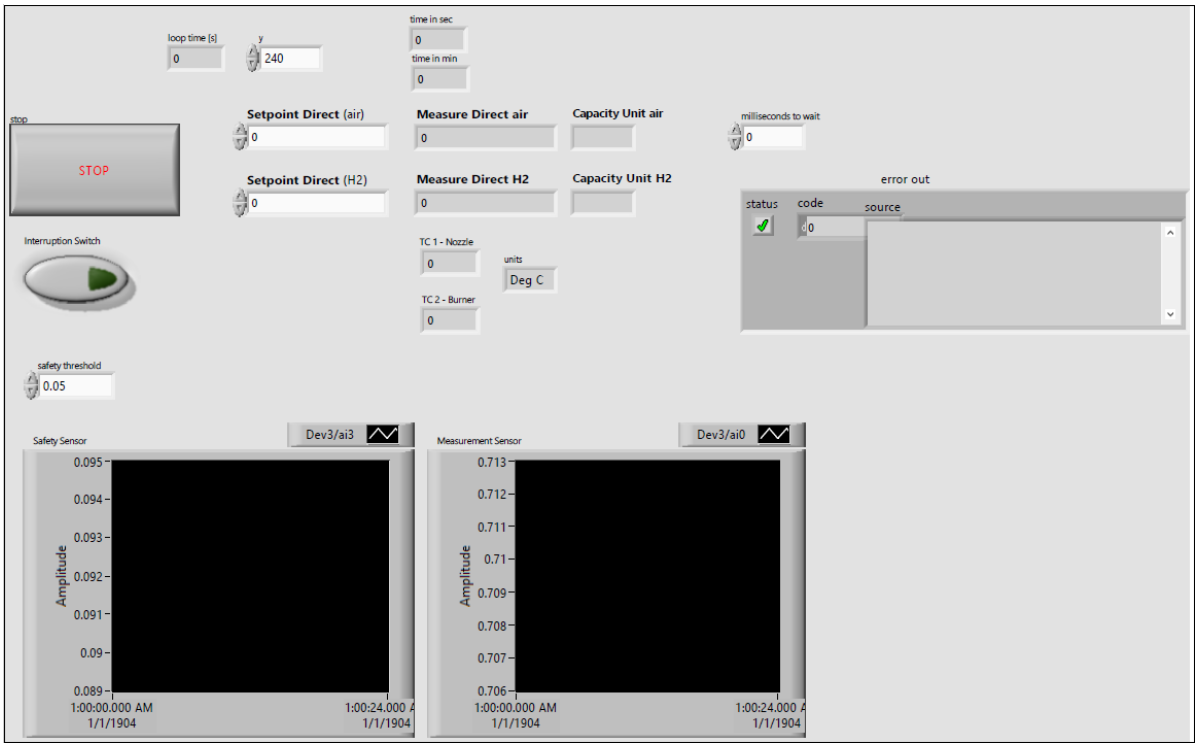

Figure C.1: Interface of *LabVIEW* software.

The user can set the duration of the measurement in the field "y". After that period, the gas supply is stopped, and no data is stored. The "Setpoint Direct" fields allow the user to control the volume flows of air and hydrogen. "milliseconds to wait" determines the frequency at which parameters are measured and stored. The "safety threshold" is used to open the shut-off valves in the hydrogen supply path. If the measured signal of the safety sensor falls below the chosen value, no hydrogen is supplied to the burner. The "interruption switch" allows to interrupt this control logic. This is necessary to start the experiment, since there would be no flame otherwise. The "STOP" button stops the measurement and the gas flows and acts as emergency brake. During the measurement, several parameters are displayed on the interface. The time since the beginning of the measurement in minutes and seconds and the loop time between the single measurements (which corresponds to the chosen frequency). The actual gas flow of hydrogen and air. The temperature measured by the thermocouples. The diagrams show the signal of both UV sensors.

List of Figures

List of Tables